Microwave and terahertz studies of the electron dynamics in two-dimensional electron systems.

Muhammad Usman Shaukat (B.Eng, MSc Eng)

Submitted in accordance with the requirements for the degree of

Doctor of Philosophy.

The University of Leeds

School of Electronic and Electrical Engineering

September 2012

Intellectual Property and Publication Statements

The candidate confirms that the work submitted is his/her own, except where work which has formed part of jointly authored publications has been included. The contribution of the candidate and the other authors to this work has been explicitly indicated below. The candidate confirms that appropriate credit has been given within the thesis where reference has been made to the work of others.

The second half of chapter 3 in the thesis is based on the work from jointly-authored publication. The details of jointly-published work are as follows;

Title: Simultaneous measurement of orthogonal components of polarization in a free-space propagating terahertz signal using electro-optic detection. Authors: M. B. Byrne, M. U. Shaukat, J. E. Cunningham, E. H. Linfield and A. G. Davies. Publication details: Appl. Phys. Lett. 98, 151104 (2011).

I was directly involved in the system design, sample preparation, experimental data recording and experimental data processing/analysis for publication purposes along with the post-doc who was leading the project at that point in time.

"God does not play dice."

Albert Einstein

Blank page

The University of Leeds

Abstract

Faculty of Engineering
School of Electronic and Electrical Engineering

Doctor of Philosophy (PhD)

by Muhammad Usman Shaukat (B.Eng, MSc Eng)

This thesis reports the design and implementation of different experimental systems to study electron-dynamics in two-dimensional electron gases (2DEGs) at microwave and terahertz (THz) frequencies. Both time and frequency domain techniques have been used to study the transport properties of electrons in GaAs/AlGaAs heterostructures. First of all a free-space time-domain spectroscopy (TDS) polarisation sensitive detection system capable of measuring the full polarization state of a propagating THz electric field has been demonstrated. Polarization-sensitive systems provide additional information on material characterization that is inaccessible through conventional techniques. The polarization sensitivity of the THz-TDS system has been evaluated using a 0.5mm thick $LiNbO_3$ sample. The ability to measure the rotation in polarisation caused by a sample allows measurement of direction-dependent material properties, such as the electrical conductivity of low-dimensional semiconductors displaying the quantum Hall effect, or the dielectric permitivity in anisotropic material systems. The newly designed system has been used to evaluate the magneto-conductivity of a 2DEG up to 1.4 THz and 6T. Two separate continuous-wave polarisation-sensitive free-space systems, operating at microwave and THz frequencies, have also been demonstrated. Both systems have been used to study the magneto-conductivity of a 2DEG at microwave (75–110 GHz) and THz (2.6–3.2 THz) frequencies up to a magnetic field of 8T. The continuous-wave microwave system has also been used to study the phenomenon of edge magneto-plasmons in a 2DEG. The work presented in this thesis provides a valuable groundwork to study the electron-dynamics in 2DEGs over a wide range of frequencies (both microwave and THz) and for a wide range of experimental conditions.

Acknowledgements

First of all thanks to Almighty God Who blessed me with the opportunity to work on this project. Then I would like to thank following people for their help and support all the way during my work:

- Prof. E. H. Linfield: He has always been an inspiration.
- Prof. A. G. Davies and Prof. J. E. Cunningham: Many thanks for this wonderful opportunity.
- My friends: Kasif, Osama, Matthew, Farhan, Divyang, Raed, Zeeshan, Shah, Siddhant and all the ghosts I met in Leeds, you all have been just amazing. I couldn't have asked for more. I would also like to express my gratitude for the help and support from Dr Paul Dean and Dr Terry Cousens.
- Finally my Family: Without their love, prayers and support, it would have been just impossible to come this far in my life.

Contents

List of Figures

List of Tables

Abbreviations

2D	**T**wo–dimensional
2DEG	**T**wo–dimensional **E**lectron **G**as
2DES	**T**wo–dimensional **E**lectron **S**ystem
AlGaAs	**A**luminium **G**allium **A**rsenide
BTC	**B**ound to **C**ontinuum
CR	**C**yclotron **R**esonance
CSL	**C**hirped **S**uper **L**attice
CW	**C**ontinuous **W**ave
DH	**D**ouble **H**eterostructure
DM	**D**ouble **M**etal
EO	**E**lectro **O**ptic
EMP	**E**dge **M**agneto **P**lasmon
EM	**E**lectro **M**agnetic
FT	**F**ourier **T**ransform
FTIR	**F**ourier **T**ransform **I**nfrared
FWHM	**F**ull **W**idth at **H**alf **M**aximum
GaAs	**G**allium **A**rsenide
GaSe	**G**allium **S**elenide
GHz	**G**iga **H**ertz
He–Ne	**H**elium – **N**eon
HEMT	**H**igh **E**lectron **M**obility **T**ransistor
InP	**I**ndium **P**hosphide
IQHE	**I**nteger **Q**uantum **H**all **E**ffect
$LiNbO_3$	**L**ithium **N**iobate

LO	**L**ongitudinal **O**ptical
MBE	**M**olecular **B**eam **E**pitaxy
MM	**M**etal **M**etal
MHz	**M**ega **H**ertz
MOVPE	**M**etal **O**rganic **V**apour **P**hase **E**pitaxy
MOSFET	**M**etal **O**xide **S**emiconductor **F**ield **E**ffect **T**ransistor
MQW	**M**ultiple **Q**uantum **W**ell
PC	**P**hoto **C**onductive
ps	**P**ico **S**econd
QCL	**Q**uantum **C**ascade **L**aser
QHE	**Q**uantum **H**all **E**ffect
QW	**Q**uantum **W**ell
RP	**R**esonant **P**honon
SI-SP	**S**emi **I**nsulating **S**urface **P**lasmon
SL	**S**uper **L**attice
SNR	**S**ignal to **N**oise **R**atio
SPW	**S**urface **P**lasmon **W**aveguide
SQW	**S**ingle **Q**uantum **W**ell
SdH	**S**hubnikov–**d**e **H**aas
TDS	**T**ime **D**omain **S**pectroscopy
THz	**T**era **H**ertz
WANTED	**W**ireless **A**rea **N**etworking of **T**Hz **E**mitters and **D**etectors
ZnTe	**Z**inc **T**elluride

Physical Constants

Boltzmann's Constant	K_B	=	$1.380\ 650\ 3 \times 10^{-23}\ \mathrm{m^2 kgs^{-2}}$
Planck's Constant	h	=	$6.626\ 068\ 96 \times 10^{-34}\ \mathrm{Js}$
Pi	π	=	$3.141\ 592\ 65$
Speed of Light	c	=	$2.997\ 924\ 58 \times 10^{8}\ \mathrm{ms^{-1}}$
Electron charge	e	=	$1.602\ 176\ 46 \times 10^{-19}\ \mathrm{C}$
Electron mass	m_0	=	$9.109\ 381\ 88 \times 10^{-31}\ \mathrm{kg}$

Symbols

Au	Gold	
B	Magnetic field	Tesla
d	Thickness of sample	mm
$\Delta\phi$	Fourier phase difference	rad
D	Drain	
E_N	Eigenmodes	eV
E_{rad}	Radiated electric field	Vm^{-1}
E_x	Electric field along x–axis	Vm^{-1}
E_y	Electric field along x–axis	Vm^{-1}
f	Frequency	Hz
f_{RF}	Frequency of RF signal	Hz
f_{LO}	Frequency of local oscillator	Hz
I	Current	Amps
J_x	Current density along x-axis	Am^{-2}
J_y	Current density along y-axis	Am^{-2}
L	Length of Hall bar sample	μm
m_*	Electron effective mass	kg
μ	Electron mobility	$cm^2V^{-1}s^{-1}$
N	Landau level number	
n_{se}	Carrier density	cm^{-2}
ω	Angular frequency	rad/s
ω_c	Cyclotron frequency	rad/s
ω_p	Plasmon frequency	rad/s

R_H	Hall co-efficient	
R_{Hall}	Hall resistance	Ohms
R_A	Characteristic resistance along x-axis	Ohms
R_B	Characteristic resistance along y-axis	Ohms
ρ_{xx}	Longitudinal resistivity	Ωm
ρ_{xy}	Hall resistivity	Ωm
S	Source	
σ_0	DC conductivity	$(\Omega m)^{-1}$
σ_{xx}	Longitudinal conductivity	$(\Omega m)^{-1}$
σ_{xy}	Hall conductivity	$(\Omega m)^{-1}$
T	Temperature	K
T_i	Titanium	
τ	Relaxation time	ps
V_{Hall}	Hall voltage	Volts
w	Width of Hall bar sample	μm

To my family and the lovely memories of my FATHER...

Blank page

Chapter 1

Introduction

1.1 Motivation and significance of work

The motivation for this project comes from the fact that the quantum Hall effect (QHE) is used extensively to understand the transport properties of electrons in a two-dimensional electron gas (2DEG) in GaAs/AlGaAs heterostructures in condensed matter physics. Different systems have been designed to study the dynamic response of 2DEGs beyond the reported data, extending the frequency range up to 1.5 THz and magnetic field range up to 8 T. Different free space systems have been designed both in the microwave and the terahertz (THz) frequency range for the experiments.

The potential applications of this work include the understanding of underlying principles that lead to the observation of different phenomena at high frequencies (GHz/THz) in two-dimensional electron systems (2DES). The better understanding of electron-dynamics at such higher frequencies will lead to better devices that have got a 2DEG at the core such as high electron mobility transistors (HEMTs) - hence consolidation of the utility of these devices for a wide range of applications.

1.2 Thesis outline

The first chapter reviews the literature covering the dynamic study of the QHE, along with many systems and techniques for studying the QHE experimentally.

Chapter 2 deals with the basic concepts of THz-TDS and QCLs. Chapter 3 deals with different polarisation sensitive systems for studying the dynamic conductivity of 2DEGs in GaAs/AlGaAs heterostructures. The systems presented have the capability to measure both components of electric field polarisation simultaneously. Chapter 4 covers the frequency domain experimental systems used to study the dynamic conductivity of 2DEG samples at microwave and THz frequencies. Chapter 5 deals with the experimental work related to THz-TDS studies of many different 2DEG samples for a range of magnetic fields to measure the dynamic conductivity up to 1.5 THz. Chapter 6 contains a discussion regarding initial experimental results for edge magneto plasmons in large 2DEG samples. Finally Chapter 7 contains a summary of the thesis, along with some suggestions for further work.

1.3 Literature review

The most common two-dimensional electron system used in dynamical studies of the quantum Hall effect is a GaAs/AlGaAs heterostructure, in which electrons are confined to a quasi-two-dimensional (2D) plane by the electrostatic charge of a doped AlGaAs layer, which itself is electrically isolated from the 2D electrons by an undoped spacer layer. Both theoretical and experimental efforts have shown that the regions of quantized resistance evolve with frequency and temperature.

1.3.1 Quantum Hall effect

The quantum Hall effect (QHE) was discovered by K. von Klitzing et al in 1980 [1]. The QHE may be used to study the effect of a magnetic field on the transport properties of a 2DES [2–6]. There has long been considerable interest in measuring the frequency dependence of electron transport in 2D electron systems subjected to high magnetic fields, since it can reveal information on fundamental quantum-mechanical effects that is not accessible by DC transport techniques [7].

An example of such interest is the high-frequency investigation of the integer QHE, in which it is well known that up to at least 30 GHz, the characteristic quantization of magneto-resistance at integer values of the Landau-level filling factor is preserved. Experimentally, this resistance quantization has been observed by measuring the microwave/terahertz (THz) absorption or reflection coefficients

of 2D electron systems as a function of magnetic field at millikelvin temperatures [8–10].

The main motivation for exploring the QHE in the GHz/THz frequency range is that the fundamental mechanism for its existence (Anderson localization of electrons) has been predicted to break down at such frequencies [11]. This prediction is based on the assumption that the driving frequency for the 2D electrons becomes higher than their rate of scattering by the ionized impurities in the dopant layer of the heterostructure, thereby destroying the localizing effect of the impurity potential. The scope of experiments has to date been limited by the restricted frequency range available with each measurement technique, as well as the available sensitivity. Evidence for existence of the QHE at frequencies above 30 GHz in GaAs/AlGaAs heterostructures was presented by Kuchar et al [9], measuring the reflection coefficient with a crossed-waveguide geometry at milli-Kelvin temperatures. The same group also presented reflection measurements at 894 GHz in the same sample using a free-space microwave system, for which they claimed any signature of the QHE was not observable.

More recently, it has been claimed that a QHE plateau in a GaAs/AlGaAs sample was observed in the THz range using polarization-resolved free-space THz time-domain spectroscopy (THz-TDS) [12], although the measurement frequency was not specified. With this particular technique, an important point to note is that unless the sample is thick ($>$ 2mm) or the back face is wedged; the measured time-domain signal must be truncated after a very short period (typically 20 ps) to avoid incorporating reflections from the back of the sample. However, the resolution in the resulting frequency spectrum is then typically very low (40-80 GHz), directly impacting on the sensitivity of the measurement technique. To compensate for the low resolution, curve-fitting may be employed to extend the range of time-domain data, but this has the disadvantage that most of the data is then generated by the curve-fit rather than by the experiment itself. Therefore, any claim of QHE-like features measured by THz-TDS is questionable - especially when it is considered that electron localization is expected to be very weak in the THz range, and any consequent resistance quantization would need very high sensitivity for its detection.

1.3.2 Study of the dynamic conductivity of 2DEGs using THz TDS systems

There is a long history of the study of cyclotron resonance (CR) in 2DEGs using Fourier-transform infrared (FTIR) spectroscopy [13–19]. THz-TDS provides means to perform coherent spectroscopy of Landau-quantized 2DEGs, as it provides both amplitude and phase information simultaneously. A combination of THz TDS and strong magnetic field has also been reported to study the dynamic conductivity at different magnetic fields [20]. The application of THz electromagnetic transients, using THz TDS systems, to the study of the dynamical conductivity of 2DEG in GaAs/AlGaAs heterostructure has been reported up to 0.8 THz and 4 T [21–27]. Cyclotron resonance experiments have been performed to study the influence of donor and acceptor impurities on the two-dimensional electron gas in GaAs/AlGaAs heterostructures [28]. Observation of striking line narrowing in the CR of high-mobility 2DEG has also been reported for a temperature range of 4.2 to 1.2 K [29].

1.3.3 Polarisation sensitive systems

An early demonstration of polarization-sensitive THz-TDS involved the use of a free-standing wire-grid polariser to split the THz beam into two orthogonally-polarized components, which were measured by two independent photoconductive detectors [30]. A different technique used a single electro-optic detector in conjunction with manual rotation of a wire-grid polariser to selectively measure different THz electric field components in the received signal [31]. Alternatively, the electro-optic detector itself has been rotated, filtering out the unwanted field components by aligning them with appropriate crystallographic axes [32].

Simultaneous measurements of electric field components have been demonstrated using a single indium-phosphide (InP) photoconductive detector with two orthogonal switch-gaps [33, 34]. An alternative synchronous method used a single electro-optic detector [35]. Here, the direction of the THz electric field vector was inferred from measuring the polarization state of the probe laser beam co-incident on the electro-optic crystal. This technique is, however, dependent on there being a high degree of plane polarization in the pulsed femtosecond laser beam - this requirement is not fulfilled in some Ti:sapphire laser systems.

1.3.4 Quantum cascade lasers

The first quantum cascade laser (QCL) was demonstrated by Faist et al. at Bell Laboratories in 1994 [36]. The first ever QCL operating in the THz range was demonstrated by the WANTED (Wireless Area Networking of Terahertz Emitters and Detectors) consortium in 2002 [37]. At present, spectral coverage has been demonstrated from 0.84-5.0 THz, at maximum temperatures up to 178 K, pulsed, and 117 K, c.w., and output powers of up to 250 mW, pulsed, and 130 mW, c.w [38–42]. Two major design classes of active regions for QCLs have emerged namely, bound-to-continuum (BTC) and resonant-phonon (RP) designs [43–46]. There are also two types of waveguides used at present for THz QCLs namely, the semi-insulating surface-plasmon (SI-SP), and the metal-metal (MM) waveguides [47, 48]. Low divergence single-spot-like beams have been observed in case of SI-SP waveguides while high confinement in MM waveguides leads to lower output power along with very divergent beams [49].

1.3.5 Terahertz time domain spectroscopy

Terahertz (THz) time domain spectroscopy (TDS) was developed by Exter et al [50]. Normally the THz pulse shape is measured using an optical delay line in the pump or probe beam. The Fourier transform of the THz pulse provides the amplitude and phase information associated with the detected THz signal [50–53].

THz generation by photo-conductive (PC) switching was first demonstrated by Auston et al [54]. It has been reported that at the extreme of the long carrier lifetime, where n(t) is considered to be a step function, I(t) becomes proportional to the time-integral of E(t) [55]. Also it has been shown experimentally that the rise time of the photocurrent is more important than the fall time in determining the relative sensitivity of photo-conducting materials [56]. The use of photoconductive detection is known to give rise to problems with detector alignment, and requires carefully optimized detector materials and geometries, which can still provide a high level of background noise in the signals obtained [57, 58]. Signal to noise ratio and sensitivity are better with PC antenna detection at frequencies smaller than 3 THz in comparison to electro optic detection scheme, for the same average THz power and low-frequency modulation of the applied bias. But when the modulation frequency is increased to more than 1 MHz, both PC switching and electro optic

sampling techniques have comparable performance [59]. The spectral response of the PC antenna for broadband detection has been found to be determined by the temporal profile of the number of photo-carriers injected by ultra short optical gate pulses [60]. A reflection-geometry has been reported to make use of the high frequency components of the generated THz radiation. An advantage of such a configuration is that the back of the GaAs substrate is free to be modified to minimise THz reflections [61].

THz field generation using optical rectification depends on materials having electric field dependent susceptibility. When an electric field penetrates a dielectric material, it induces a macroscopic polarization. The bandwidth of the generated radiation can extend into the THz range if the incident electric field is from an ultra-fast femtosecond laser pulse; because interference between frequency components of electric field in the semiconductor may produce a THz beat frequency in the transient polarization [62]. In contrast to the PC switch, no DC bias is required in optical rectification. The radiating dipoles are induced only by the laser pulse as it propagates through the crystal. The system bandwidth is mainly limited by the dispersion of the THz signal, and the duration of the laser pulse in the crystal, assuming it is velocity-matched [63]. Typical semiconductors for generating pulsed THz waves by optical rectification are GaAs [64], gallium selenide (GaSe) [65] and zinc telluride (ZnTe) [66].

1.3.6 Edge magneto plasmons in 2DEGs

Edge magneto plasmons (EMPs) were observed experimentally for the first time in 1985 on the surface of liquid helium in the presence of a perpendicular magnetic field [67–70]. Subsequently, EMPs have been discovered in 2DEG systems such as GaAs/AlGaAs heterostructures, providing useful insight into the dynamics of electrons in very strong magnetic fields (in the quantum Hall regime). It has been shown both theoretically and experimentally that damping of EMPs is very small in strong magnetic fields and that there is a relationship between the Hall conductivity and the velocity of EMPs[71–73]. EMPs have been studied using many different experimental techniques; time-domain methods [74, 75], microwave and RF techniques [76, 77] and far-infrared measurements[78–81]. A number of detailed theoretical studies on EMPs have also been carried out [82–86].

Chapter 2

Background Theory

2.1 Two-dimensional electron gas

A two dimensional electron gas (2DEG) can be formed in a gallium arsenide/aluminium gallium arsenide (GaAs/Al-GaAs) heterostructure (Figure 2.1). The heterojunction consists of a doped layer of n-type AlGaAs, an undoped layer of AlGaAs, commonly known as a spacer, and an undoped GaAs substrate. Electrons from the donor atoms in the doped layer move to the lowest potential energy in the conduction band, which is at the interface of the adjacent undoped AlGaAs and GaAs substrate layers. Because of the physical separation of electrons from the scattering centres (ionized dopant atoms) the electron mobility is much higher in such structures than in doped bulk materials [2].

Other systems where we can have a 2DEG include:

- Quantum wells (QW)
- Silicon metal oxide semiconductor field effect transistors (MOSFETs)
- Surface of liquid helium
- Graphene

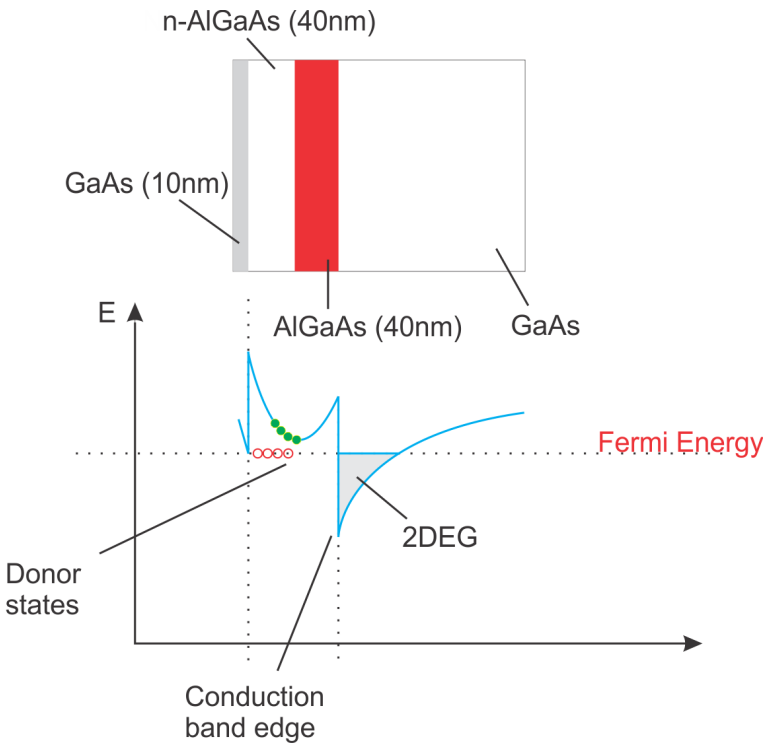

FIGURE 2.1: Formation of a 2DEG in GaAs/AlGaAs heterostructure. The figure shows how the electrons from the dopant atoms move to the lowest potential energy, where they happen to be trapped and result into a sheet of electrons.

2.1.1 Creation of Landau levels in two-dimensional electron gas

When a magnetic field B is applied perpendicular to the 2DEG, the density of states becomes a set of levels, known as Landau levels, separated by the cyclotron energy (Figure 2.2). Localised states occupy energy regions between Landau levels, where no conduction can occur, while extended states occupy the core of Landau levels. Only the extended states can carry current at low temperatures. As the magnetic field is swept, the Landau levels move relative to the Fermi energy (Figure 2.2) [2, 3].

2.1.2 Density of States in a 2DEG and oscillation of Fermi energy

The density of states of a perfect two dimensional electron system is a set of delta functions known as Landau levels when B≠0 (Figure 2.2). The effective

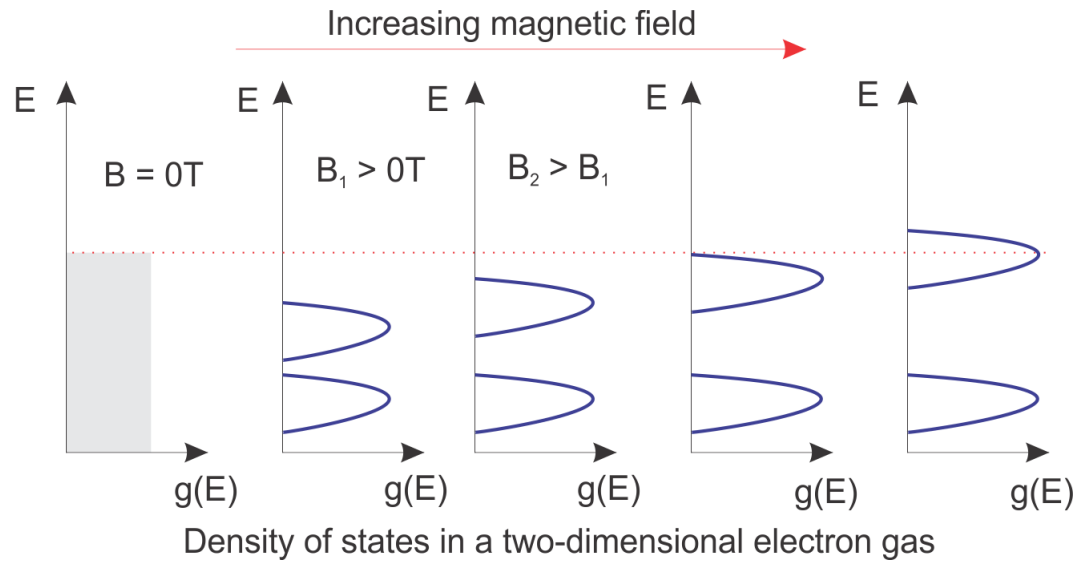

FIGURE 2.2: Formation of Landau levels, in a 2DEG, under an applied magnetic field. The density of states becomes a discrete set of energy states, known as Landau levels. The spacing between any two Landau levels increases with the magnetic field as shown.

potential experienced by an electron in a 2DEG is produced by ionised impurities, interface defects and crystal defects. These sources add a random component to the external potential from the applied magnetic field, resulting in broadening of the delta-function Landau levels (Figure 2.3). The density of states in a single Landau level is a histogram of the amplitude variation of the effective potential i.e. the applied external potential plus the random component.

The carrier density in a 2DEG could be controlled by a surface gate. Figure 2.4 shows two different situations that arise when the density of states is formed from Landau levels. In figure 2.4a the centre of a Landau level is at the chemical potential. If in this case we use a surface gate to remove a small number of electrons from the electron system the Fermi energy E_f will not change much because in the centre of a disorder-broadened Landau level the states are close together in energy. Removing one electron only changes the energy by an amount equal to the next energy spacing. In this situation the Landau level is said to be pinned at the chemical potential. In figure 2.4b there are no states at the chemical potential. In this case, in order to remove an electron, the Fermi energy must shrink rapidly, bringing occupied states in the next lowest Landau level to the chemical potential. When the nth Landau level is pinned, the chemical potential will remain at this value until the density has been reduced by an amount equal to the density of electrons in a Landau level, the Fermi energy will then jump

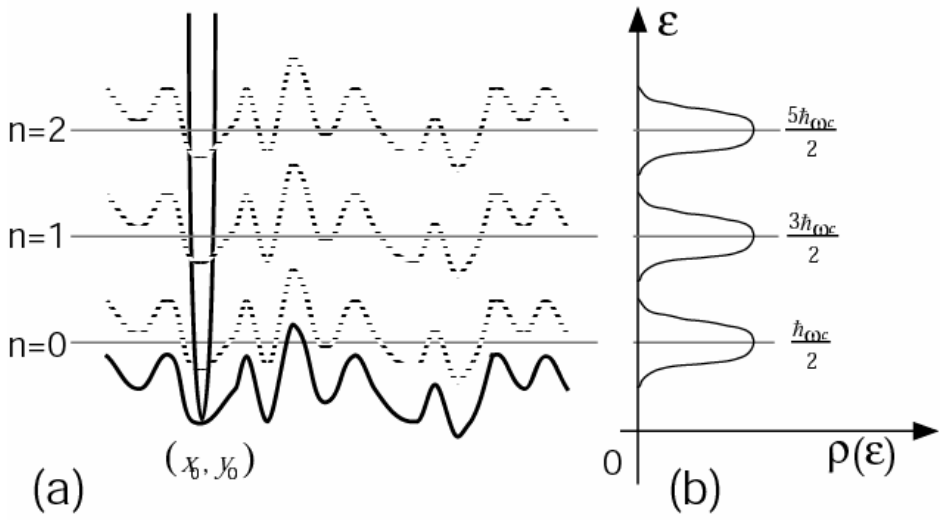

FIGURE 2.3: (a) Dark line: Random effective potential in a two dimensional electron system. Parabola centered at (x_0, y_0): effective potential due to magnetic field. Dashed lines: Local eigenstates in each Landau level. (b) Density of states for each Landau level determined from states in (a). Figure taken from [3].

to the next value and so on (Figure 2.5). When the magnetic field is increased at fixed carrier density, two things happen. Firstly, the density in each Landau level increases and therefore in order for the carrier density to remain constant the filling factor must gradually reduce and successive Landau levels with lower index will pass through the chemical potential. Secondly the spacing between Landau levels increases and therefore whilst a particular Landau level is pinned at the chemical potential, the Fermi energy will increase to accommodate this energy. These factors result in the Fermi energy oscillations as a function of magnetic field around its zero field value (Figure 2.6) [2, 3].

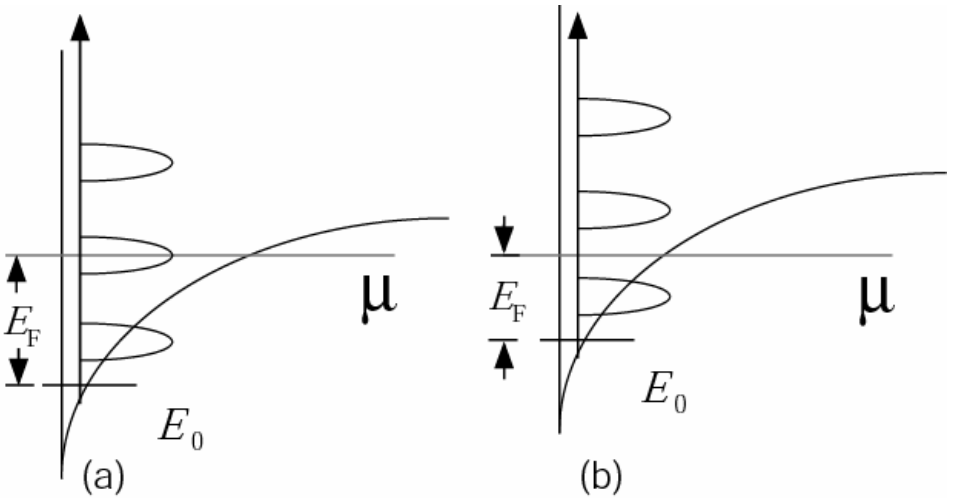

FIGURE 2.4: Hetero-junction interface occupied by a single 2DEG. (a) Landau level at the chemical potential. (b) Chemical potential between Landau levels [3].

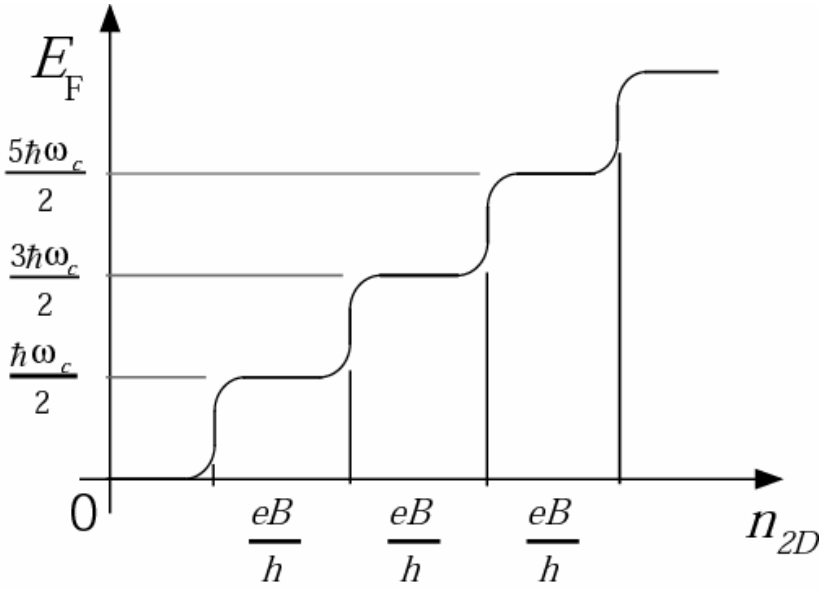

FIGURE 2.5: Fermi energy in a two-dimensional electron system as a function of carrier density at fixed magnetic field [3].

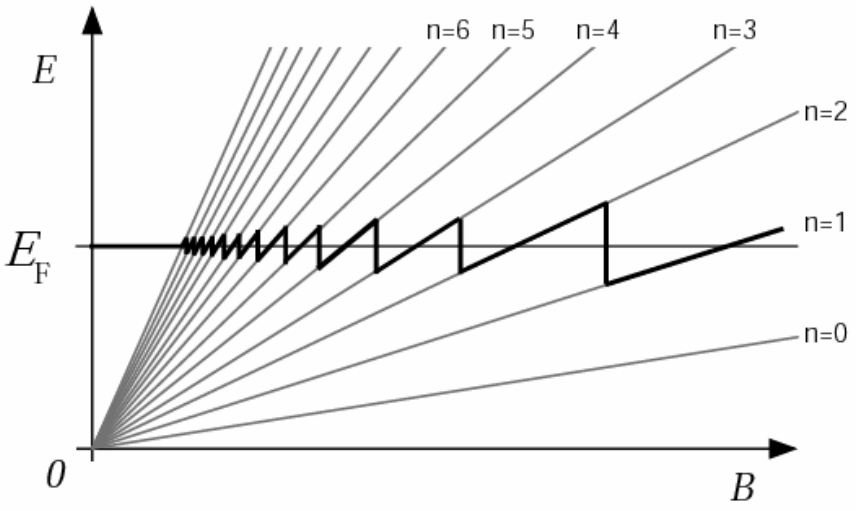

FIGURE 2.6: Grey lines: Landau Fan as a function of B for n = 0 ... 14. Black line: The Fermi energy of a two dimensional electron system as a function of magnetic field at constant density. Horizontal dark grey line: Zero field Fermi energy [3].

2.2 Cyclotron Resonance

When a magnetic field (B) is applied perpendicular to the surface of a semiconductor containing a 2DEG, electrons in the 2DEG start moving in a circle around the lines of applied field. The angular frequency of the electrons in this case is given by:

$$\omega_c = \frac{eB}{m^*} \tag{2.1}$$

where ω_c is the angular frequency known as cyclotron frequency, e is the electronic charge and m^* is the effective electron mass.

The energy eigenvalues (E_N) for 2D free electrons in a perpendicular magnetic field are obtained from the solutions of the Schrodinger equation.

Mathematically:

$$E_N = \left(N + \frac{1}{2} \right) \hbar\omega_c \tag{2.2}$$

where $N = 0, 1, 2.....n$ is the Landau level number and $\hbar\omega_c$ is the energy difference between any two adjacent Landau levels, known as cyclotron energy. Cyclotron energy can be envisaged as the energy associated with the quantum transition between adjacent Landau levels. This quantum transition may be induced by a free-space THz electric field propagating through the 2DEG, in which case there is resonant absorption of energy by the electrons, an effect known as CR.

2.2.1 Conditions for cyclotron resonance absorption

Important conditions for the observation of CR absorption are:

- High mobility 2DEG sample: If the relaxation time τ is not sufficiently high, then the electrons will get scattered even before completing one complete rotation around the magnetic field lines resulting in absorption of incident energy but not at a specific frequency. A high mobility 2DEG with long relaxation time is therefore required. Mathematically the condition can be written as;

$$\omega_c\tau \; >> \; 1 \tag{2.3}$$

- Cryogenic temperature and strong magnetic field: If the temperature is not low enough then the average thermal energy of the electrons k_BT will be

bigger than the cyclotron energy and as a consequence electrons will move between adjacent Landau levels due to thermal fluctuations. Observation of CR then becomes very difficult or impossible. Mathematically;

$$\hbar\omega_c \; >> \; k_B T \tag{2.4}$$

If the magnetic field is not strong enough then the spacing between adjacent Landau levels will be quite small making detection of CR difficult owing to lower system resolution.

2.2.2 Effective mass measurement

The effective mass of the 2DEG electrons can be extracted from the experimental data by fitting the following expression to the experimental data for CR absorption;

$$\omega_c = \frac{eB}{m^*}$$

$$2\pi f = \frac{eB}{m^*}$$

$$f = \frac{eB}{2\pi m^*} = \frac{eB}{2\pi C m_0} \tag{2.5}$$

where f is the THz frequency, m_0 is the electron rest mass and C is the constant of effective mass that can be extracted by fitting the above mentioned expression to the experimental data.

2.3 Quantum Hall effect in two-dimensional electron gas

The Hall effect is used to evaluate the mobility and carrier density of a given semiconductor sample. At low temperatures, under a large applied magnetic field B, the quantum Hall effect (QHE) can be observed in a 2DEG, where electrons are only allowed to move in a plane. At low temperatures, typically $\leq$ 77K, it is found that the Hall resistance of a 2DEG has a plateau as a function of magnetic field [2–4].

When the Fermi energy lies in the bands of localised states between Landau level centres, there is no conduction current and no change in the Hall resistance. The Hall resistance appears as a plateau and the longitudinal resistance vanishes. It is only when the Fermi energy passes through the extended states in the centres of Landau levels that the longitudinal resistance becomes appreciable, and the Hall resistance concurrently makes its transition to the next plateau. In the integer quantum Hall effect (IQHE), the Hall resistance at a plateau is given by:

$$R_H = \frac{h}{ie^2} \tag{2.6}$$

where i is the integer that is identified with the number of completely filled Landau levels. The Hall plateaux appear at incredibly precise values of resistance, no matter which sample is measured. Due to the high precision of the measurement, the quantisation of the Hall resistance is now used as the standard for resistance [1–6].

2.3.1 Hall effect measurement theory

The QHE is used to study the effect of a magnetic field on the transport properties of a two dimensional electron system (2DES). The semi-classical Boltzmann formalism fails to account for transport in high magnetic fields because this theory is based on the assumption that the electrons do not make transitions between energy bands, and that the band structure does not change significantly i.e. E vs k. Neither assumption is valid when B is very large. Within the Drude formalism the longitudinal resistivity is independent of magnetic field, whereas the transverse

HEMT Sample	*Recipe*	*Magnetic Field*	*Mobility Dark/Light*	*Sheet Density Dark/Light*
	(nm)	(T)	$(cm^2V^{-1}s^{-1})$	(cm^{-2})
L409	40:40:10	0.08	63000/88000	$9.93\times^{10}/1.39\times10^{11}$
L410	40:40:10	0.08	83000/137000	$1.03\times10^{11}/2.14\times10^{11}$
L412	40:40:10	0.08	27000/50000	$1.16\times10^{11}/2.33\times10^{11}$
L413	40:40:10	0.08	87000/127000	$8.63\times10^{10}/1.81\times10^{11}$
L424	40:40:10	0.08	1520000/1930000	$1.99\times10^{11}/2.88\times10^{11}$
L425	40:40:10	0.08	1510000/2440000	$1.81\times10^{11}/2.74\times10^{11}$
L355	40:40:10	0.08	79000/135000	$1.21\times10^{11}/2.13\times10^{11}$
L356	40:40:10	0.08	322000/540000	$1.71\times10^{11}/2.91\times10^{11}$
L357	40:40:10	0.08	206000/338000	$1.45\times10^{11}/2.35\times10^{11}$

TABLE 2.1: Measured mobility (μ) and sheet carrier density (n_s) values for different HEMT samples using QHE at 1.8K. The growth temperatures for L409, L410, L412 and L413 are 585°C, 600°C, 570°C and 620°C respectively (Appendix B). In other high electron mobility transistor (HEMT) samples, the doping concentration has been changed. 40:40:10 represents the thickness of doping, spacer and cap layers in nm respectively.

(Hall) resistivity increases linearly with magnetic field. The resistivity tensor of a 2DEG can be measured using a Hall bar (Figure 2.7). For resistivity measurements, a current is passed between ohmic contacts S and D. For the longitudinal resistivity the voltage between contacts A and B is measured to find E_x. For the Hall resistivity the voltage between ohmic contacts A and C is measured to find E_y. The Hall resistivity and Hall resistance are found to be equal. Measurement of the Hall effect can be used as a standard electrical characterisation technique which is able to determine the carrier density and mobility of a semiconductor. The main purpose of a Hall measurement is to determine the carrier concentration from the induced Hall voltage and hence the mobility of the material [1–6]. The DC characterisation data of all HEMT samples used for magneto-conductivity measurements is given in table 2.1. Two diffrent sample sizes have been used for all the measurements. The small samples are referred to as small Hall bars while the large samples are referred to as large square samples in this thesis. The small Hall bars have been characterised using the Hall bar technique while the large square samples have been characterised using the Van der pauw technique.

2.3.1.1 Hall bar technique

Considering Hall bar geometry, the Hall resistivity (ρ_{xy}) of a 2DEG is:

$$\rho_{xy} = \frac{E_y}{J_x} = \frac{B}{n_s e} \tag{2.7}$$

where B is the magnetic field, n_s is sheet carrier density and e is the electron charge.

Hall voltage (V_H) along the y direction can be measured easily (Figure 2.7);

$$V_H = \frac{IB}{n_s e} \tag{2.8}$$

where I is the current between S and D (Figure 2.7).

Rearranging the above equations the sheet density can be determined as;

$$n_s = \frac{IB}{eV_H} \tag{2.9}$$

Thus, by measuring the Hall voltage (V_H) and from the known values of I, B and e one can determine the sheet density (n_s) of charge carriers in semiconductors.

The longitudinal resistivity (ρ_{xx}) can easily be determined by measuring the longitudinal voltage (V_x) and then using the formula;

$$\rho_{xx} = \frac{E_x}{J_x} = \frac{V_x}{I} \cdot \frac{w}{L} \tag{2.10}$$

where w is the width and L is the distance between contacts and the ratio w/L is equal to 1/4 (Figure 2.7).

The longitudinal resistivity is used to evaluate 2DEG sample mobility;

$$\mu = \frac{R_H}{\rho_{xx}} = \frac{1}{n_s e \left(\frac{V_x}{I}\left[\frac{w}{L}\right]\right)} = \frac{1}{n_s e \left(\frac{V_x}{I4}\right)} \tag{2.11}$$

where $R_H = \frac{1}{n_s e}$ is the Hall coefficient.

At small magnetic field values, the Boltzmann formalism works well i.e. longitudinal resistivity is a constant and Hall resistivity varies in a linear fashion in the magnetic field. However at high magnetic field values the longitudinal resistivity

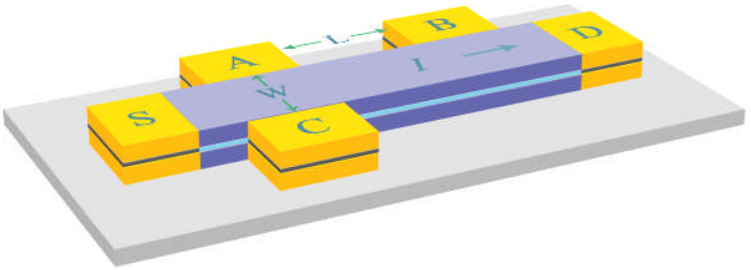

FIGURE 2.7: Hall Bar mesa to measure the Hall effect. The Hall voltage can be measured between contacts A and C while longitudinal voltage can be measured between contacts A and B, under an applied magnetic field. W is the width of the Hall bar while L is the spacing between A and B. Using the values for induced Hall voltage and longitudinal voltage, mobility and carrier density of a semiconductor sample can be evaluated. For the samples used ratio of w to L is equal to 1/4. [3]

begins to oscillate periodically with respect to $\frac{1}{B}$ and the Hall resistivity begins to show plateau at values $\frac{h}{ie^2}$, where i is an integer.

The oscillations in longitudinal resistivity are referred to as the Shubnikov-de Haas (SDH) effect and the plateau in Hall resistivity are referred to as the QHE. In the regions where longitudinal resistivity is zero, this implies that the longitudinal conductivity is zero as well (Figure 2.8) [2, 3].

Carrier sheet density (n_s) and mobility (μ) values can be calculated using the single point values e.g. using the Hall and longitudinal voltage values at 0.08T magnetic field. Also sheet density can be evaluated using the slope of the plot between Hall voltage and magnetic field. It must be noted that the HEMT sample should be operated, where a linear relationship exists between the current through the device and the voltage applied across it.

2.3.1.2 Van der pauw technique

This is another well known technique to measure the carrier concentration and mobility of semi-conductor samples. This method requires the availability of four

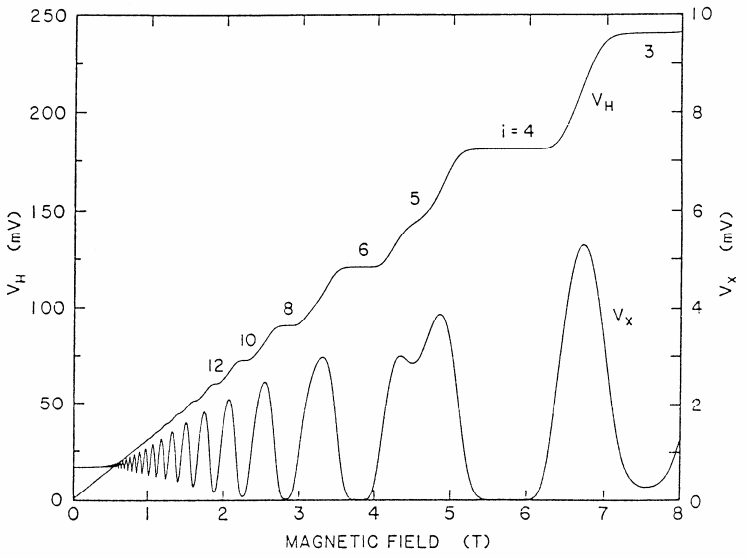

FIGURE 2.8: Hall and diagonal magneto-resistance of an n-type GaAs-AlGaAs hetero-junction for a source drain current of 25μA at 1.2K. [3]

ohmic contacts to the sample under test. A set of resistivity measurements is carried out to determine the longitudinal resistivity, ρ_{xx}. Van der Pauw verified that there are two characteristic resistances R_A and R_B associated with ρ_{xx}, as shown by equations below [87].

$$R_A = \frac{V_{34}}{I_{21}} = \frac{V_{43}}{I_{12}} \tag{2.12}$$

$$R_B = \frac{V_{14}}{I_{23}} = \frac{V_{41}}{I_{32}} \tag{2.13}$$

To obtain the two characteristic resistances, a DC bias is applied across contacts 3 and 4 and the resultant voltage is measured across contacts 1 and 2 and vice versa. Similarly, a DC bias is applied across contacts 2 and 3 and the resultant voltage is measured across contacts 1 and 4 and vice versa (Figure 2.9). The two characteristic resistances R_A and R_B are related to the longitudinal resistivity ρ_{xx} via the van der Pauw equation.

$$exp\left(\frac{-\pi R_A}{\rho_{xx}}\right) + exp\left(\frac{-\pi R_B}{\rho_{xx}}\right) = 1 \tag{2.14}$$

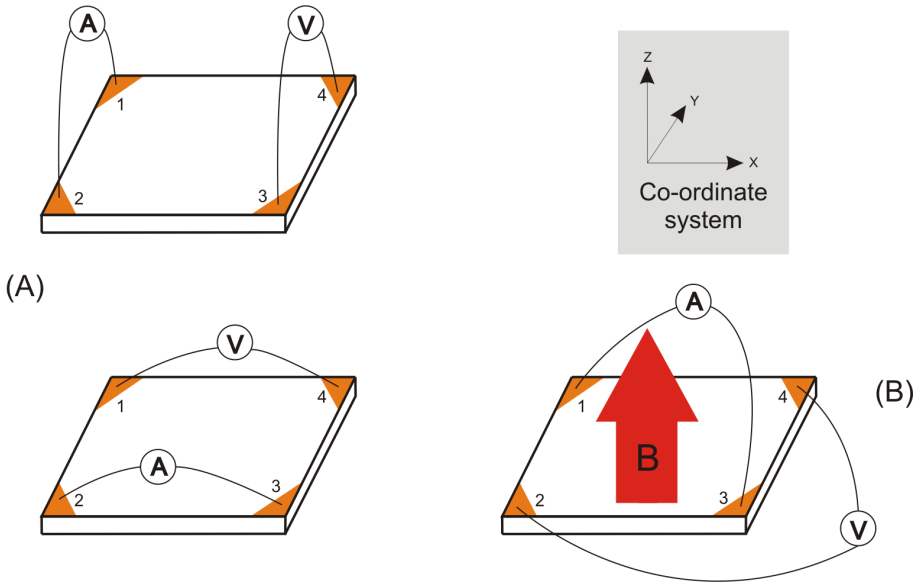

FIGURE 2.9: Van der Pauw technique for quantum Hall measurements in a 2DEG. (A) Measurement of resistivity to evaluate mobility of system. (B) Hall voltage measurement to evaluate carrier density of system under test.

Finally the mobility of system under test is evaluated using the following expression.

$$\mu = \frac{1}{en_s\rho_{xx}} \tag{2.15}$$

The carrier concentration of the system under test is evaluated using the Hall voltage measurements. In order to measure the Hall voltage, a DC bias is applied across contacts 2 and 4 and the corresponding voltage is measured across contacts 1 and 3 and vice versa. Similarly, a DC bias is applied across contacts 1 and 3 and the corresponding voltage is measured across contacts 2 and 4 and vice versa (Figure 2.9). The final value of the Hall voltage is obtained by averaging the four Hall voltage values measured individually. Mathematically:

$$V_H = \frac{1}{4}\left[V_1 + V_2 + V_3 + V_4\right] \tag{2.16}$$

Finally the carrier concentration is evaluated using the following expression.

$$n_s = \frac{IB}{eV_H} \tag{2.17}$$

2.4 Terahertz time-domain spectroscopy

THz time-domain spectroscopy (TDS) was developed by Exter et al [50]. It is a well-established technique for the coherent generation and detection of pulsed THz radiation. It is based on time-domain techniques that employ either photoconductive or electro-optic methods for generation and detection of THz radiation. A THz-TDS system comprises a femtosecond laser source that is split into two beams namely; pump and probe beams. The pump beam is used to generate THz radiation that is passed through the sample and then focused onto the detector. The detector is gated by the probe beam (Figure 2.10). The THz pulse shape is measured using an optical delay line in the pump or probe beam. The Fourier transform of the THz pulse provides its amplitude and phase information in the frequency domain. The frequency spectrum is important in the application of THz-TDS systems to imaging and spectroscopic analysis [50–52]. In spectroscopic analysis, the THz waves interact with a sample material, and the waveform picks up characteristic features associated with the material's response to electric fields. These features are often observable more easily in the frequency domain than the time domain.

2.4.1 THz Sources and Detectors

Two commonly used methods for generation and detection of THz radiation in TDS systems are:

- Photoconductive (PC) switching
- Optical rectification and electro optic (EO) sampling

In both methods a semiconductor material is bombarded with femto-second laser pulses. The difference between the THz waveforms in each case can be explained quantitatively in terms of carrier lifetime and frequency-dependent response of the material used [52].

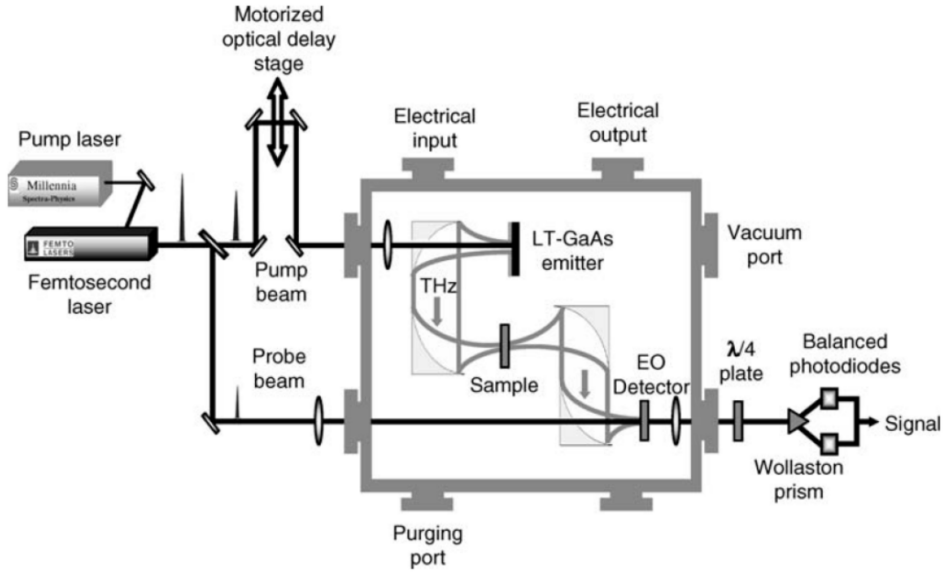

FIGURE 2.10: Example of a free-space THz-TDS system, employing photoconductive generation and electro-optic detection of THz pulses. The box is purged with nitrogen to eliminate absorption by atmospheric water vapour [53].

2.4.1.1 Photoconductive switching

THz generation by PC switching was first demonstrated by Auston et al [54]. It is based on the transport of photo-induced carriers in a semiconductor. A PC switch consists of a highly resistive direct band-gap semiconductor with two electric contacts. In most cases, the semiconductor is a III-V compound like gallium arsenide (GaAs). It is epitaxially grown as a thin film on a semi-insulating GaAs substrate (SI-GaAs), which is also a highly resistive material. The important difference between the SI-GaAs substrate and the film is the relaxation time for the excited carriers. In a SI-substrate the carrier lifetime can be as high as 500ps, while in the film it is often less than 1ps. For THz generation using a PC emitter, a DC bias is initially applied across the semiconductor. A femtosecond laser beam is then focused onto the semiconductor surface, between the electrodes, which induces photo-carriers inside the semiconductor material. The applied DC bias accelerates the photo-induced carriers resulting in dipole-like current pulses. Each current transient emits electromagnetic radiation, for which the useful bandwidth extends into the THz frequency range, owing to the fast rise time of the photocurrent induced by the femtosecond laser. The usable bandwidth can be maximized to around 20-30 THz if the photo-carrier lifetime is also very short ($\leq$ 1 ps). The

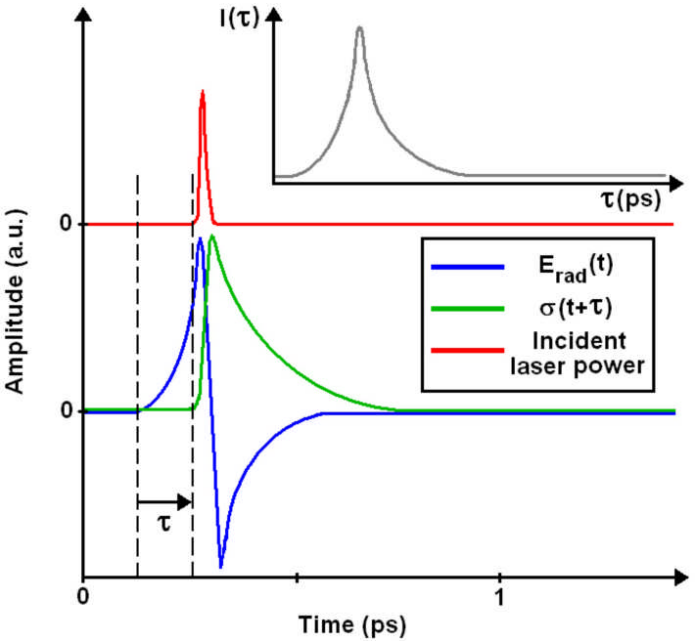

FIGURE 2.11: Convolution of the transient photoconductivity $\sigma(t+\tau)$ and the THz electric field E_{rad}(t) in the detection switch. Inset: The resulting photocurrent signal plotted as a function of τ [88].

instantaneous electric field of the generated THz radiation is proportional to the rate of change of the total current density.

Mathematically:

$$E_{rad}(t) \propto \frac{dJ(t)}{dt} \tag{2.18}$$

It can be shown by the following argument that the peak amplitude and bandwidth of the electric field pulse depends on the mobility and lifetime of the charge carriers. During the initial stages of the THz pulse generation, the rise time of the THz electric field depends on the rate of photo-carrier generation, which is mainly determined by the leading edge of the laser pulse. After laser excitation, the peak amplitude of the THz electric field is determined by the mobility of photo-induced carriers. The decay time of the generated THz electric field is determined solely by the carrier lifetime.

A PC switch may also be used as a THz detector, if a current amplifier is connected across the electrical contacts. The PC switch is then gated by the femto-second laser pulse. The excited carriers are accelerated by the electric field of the incident THz radiation, resulting in a measurable current signal (Figure 2.11). The photo-current from the antenna is proportional to the time integral of the product of

the incident THz electric field and the total number of photo-carriers in the PC switch.

Mathematically:

$$I(\tau) = e\mu\tau_c m \int_{-\infty}^{\infty} E(t)n(t-\tau)dt \tag{2.19}$$

where e is the electron charge, μ is the carrier mobility, e is the carrier lifetime, m is the repetition frequency of the laser and τ is the relative time delay between the THz pulse and the gating laser pulse. In the limit of short carrier lifetime, where n(t) is considered to be a delta function, I(τ) becomes proportional to E(t). On the other hand, at the limit of long carrier lifetime, where n(t) is considered to be a step function, I(τ) becomes proportional to the time-integral of E(t) [55]. Since the carrier mobility and lifetime are mainly determined by the band structure of the semiconductor material used for a PC switch, only very few semiconductor materials are suitable for the THz generation and detection. An additional requirement for the PC switch is high resistivity to minimise the leakage current.

2.4.1.2 Optical rectification and electro optic sampling

Optical rectification is a non-linear process where a crystal gets electrically polarized at high optical intensities. In this process a high intensity laser pulse passes through a transparent crystal material that emits a THz pulse without an applied bias. THz field generation using optical rectification depends on materials having electric field dependent susceptibility. When an electric field penetrates the semiconductor, it induces a macroscopic polarization and the general relation between the electric field and polarisation becomes non-linear as a result of the field-dependence of the susceptibility. If the incident electric field is time-dependent, then the polarization charge generates an electromagnetic radiation field, of which the electric field is proportional to the second time-derivative of the polarization vector. The bandwidth of the generated radiation can extend into the THz range if the incident electric field is from an ultra-fast femtosecond laser pulse; because interference between frequency components of electric field in the semiconductor may produce a THz beat frequency in the transient polarization [62].

In contrast to the PC switch, no DC bias is required in optical rectification. The radiating dipoles are induced only by the laser pulse as it propagates through the

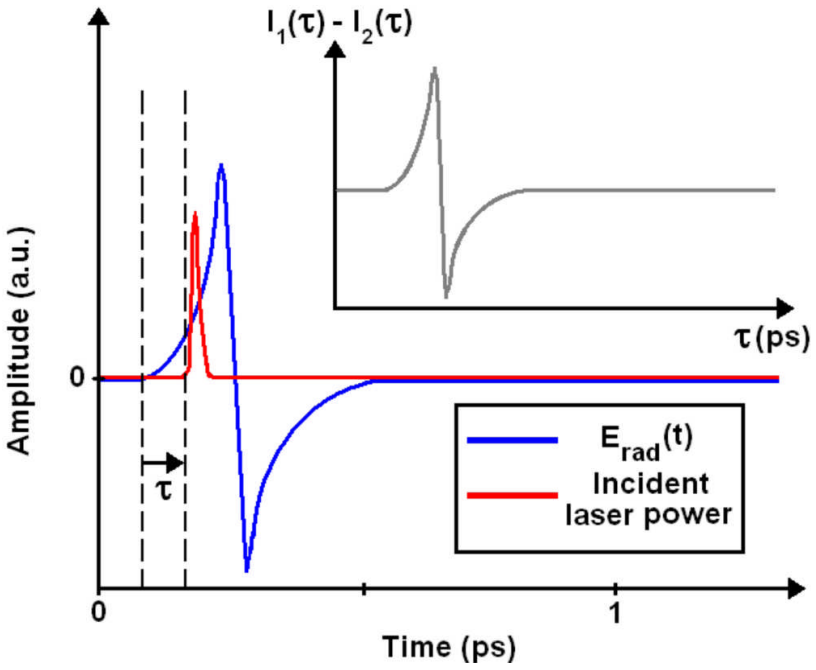

FIGURE 2.12: Convolution of the laser pulse and the THz electric field in the electro-optic crystal. Inset: The difference in photocurrents plotted as a function of τ [88].

crystal. The system bandwidth is mainly limited by the dispersion of the THz signal, and the duration of the laser pulse in the crystal, assuming it is velocity-matched [63]. Reducing the crystal thickness reduces the distance over which such interference and dispersion may occur, thereby limiting these effects. However, if the crystal is too thin, the overall polarisation charge will be lowered, reducing the radiated THz power.

The electro-optic effect is a nonlinear coupling between a laser beam and a relatively low frequency electric field in the sensor crystal (Figure 2.12). Modulating the birefringence of the sensor crystal via an applied, polarised electric field will modulate the polarisation ellipticity of the optical probe beam passing through the crystal [62]. The incident THz electric field induces a change in polarisation inside the EO crystal that is detected by the balanced photo-diodes. In EO the detected signal is proportional to the THz electric field. It has been shown that free space electro-optic sampling offers a flat frequency response over an ultra wide bandwidth. The spectral response of the EO sampling technique is affected by any frequency-dependent mismatch between the group velocity of the gating probe beam and the THz phase velocity in the EO crystal, and by the reflection loss at the EO crystal surface [63]. In general, optical rectification produces wider THz

bandwidths than photoconductive switching, since the decay time of generated radiation is not limited by charge-carrier lifetime.

2.5 Quantum cascade lasers

In semiconductor microstructures of nanometer size, the behaviour of electrons is strongly affected by the quantum nature of the electrons and exhibits a remarkable dependence on the parameters specifying the structure. Therefore, by appropriate design of the structure parameters, one can implement artificial novel electronic properties different to the intrinsic characteristics of the bulk materials. The de Broglie wavelength of electrons in a very thin (less than a few tens of nanometers) semiconductor film structure is comparable with the thickness of the film. In such a structure, electrons exhibit interesting electric and optical characteristics dissimilar to those in bulk semiconductors and ordinary double heterostructures (DHs). The most fundamental semiconductor quantum heterostructure is a single quantum well (SQW), which consists of a very thin layer of a semiconductor sandwiched between two layers of a semiconductor having band-gap energy larger than that of the thin layer. The conduction- and valence-band edges of this structure form potential wells. The region of the thin layer is called a well, and the regions of the side layers are called barriers. A structure consisting of several quantum wells stacked with thick barriers, where coupling between wells is negligible, is called a multiple-quantum-well (MQW) structure. On the other hand, a structure consisting of many alternately stacked thin wells and thin barriers, where the wells are coupled to each other, is called a superlattice (SL) [47].

Quantum cascade lasers (QCLs) are semiconductor lasers that emit in the mid to far infrared portion of the electromagnetic (EM) spectrum and were first demonstrated by Faist et al. at Bell Laboratories in 1994 [36]. Unlike interband semiconductor lasers that emit electromagnetic radiation through the recombination of electron-hole pairs across the material bandgap, QCLs are unipolar devices and consist of hundreds of alternating layers of high and low band gap semiconductors that are each just a few atoms thick. The low band gap material is often GaAs, while the high band gap material on either side of it could be aluminium gallium arsenide ($Al_xGa_{1x}As$). If each layer of GaAs is sufficiently thin, typically a few nanometers, the allowed electronic energy levels in its conduction band are split into a series of sub bands. Under an applied electric field an electron that

is injected into this layer can therefore drop down from a high energy to a low energy sub band, emitting a photon in the process. A QCL is, in effect, a series of these individual quantum wells grouped together to make active units. By making $Al_xGa_{1x}As$ barriers sufficiently thin, an electron can tunnel from one active unit to the next. Each time it does so; the electron drops to a lower energy level and emits a photon. In the case of interband semiconductor lasers, the emission wavelength is essentially fixed by the bandgap of the particular material system used; however QCLs free us of this so called bandgap slavery as the emission wavelength can be tuned over a wide range in the same material system by suitable design of the layer thicknesses in the semiconductor superlattice. By appropriately engineering the thickness and composition of the layers in active units, the transition energy can be tailored to cover a wide range of frequencies from the mid-infrared down to the THz range. QCLs can contain as many as 100 active units stacked together. In general, successive active units are linked by a small group of coupled wells, called injector regions, so that electrons transfer from one active region to the next as efficiently as possible.

2.5.1 QCL active region designs

The MQW active region is the heart of any QCL. To obtain gain for electromagnetic waves at the frequency f, the energy levels, wave functions and scattering rates must be properly engineered to provide a population inversion between two states separated by an energy hf. Aside from the chirped super-lattice (CSL) active region, two major design classes of active regions have emerged: bound-to-continuum (BTC) and resonant-phonon (RP) designs [43].

2.5.1.1 Bound to continuum

The CSL is based on the coupling of several quantum wells together in a superlattice to create so-called minibands of states when the appropriate electric field is applied. The radiative transition is designed to take place from the lowest state of the upper miniband to the top state of the lower miniband. The original CSL design has given way to the BTC design (Figure 2.13). In BTC active region design the lower radiative state and miniband-based depopulation remains the same as that in CSL, but the upper radiative state is essentially made to be a bound defect

state in the minigap. The effect is a radiative transition, which is more diagonal in real space than the transition in single quantum well.

Compared with a CSL design, the oscillator strength of the transition drops slightly, as the overlap with the miniband states drops, but the upper-state lifetime increases as non-radiative scattering is similarly reduced. The injection process also becomes more selective, as the injector states couple more strongly with the upper state than with the lower miniband. As a result, BTC active region designs display improved temperature and power performance compared with the CSL designs [43–46].

2.5.1.2 Resonant phonon

In the resonant phonon (RP) active region design (Figure 2.13), collector and injector states are designed to be below the lower radiative state by approximately $E_{LO} = 36\text{meV}$, so that electrons in the lower state will scatter very quickly into the injector states by emitting an LO-phonon. RP active region design brings the lower radiative state into a broad tunnelling resonance with the excited state in the adjacent quantum wells, so that its wavefunction is spread over several quantum wells. As a result, the lower radiative state maintains a strong spatial overlap with the injector states and experiences sub-picosecond LO-phonon scattering [43–46]. The RP active region design of THz QCLs tends to have higher threshold current values in comparison to BTC active region design.

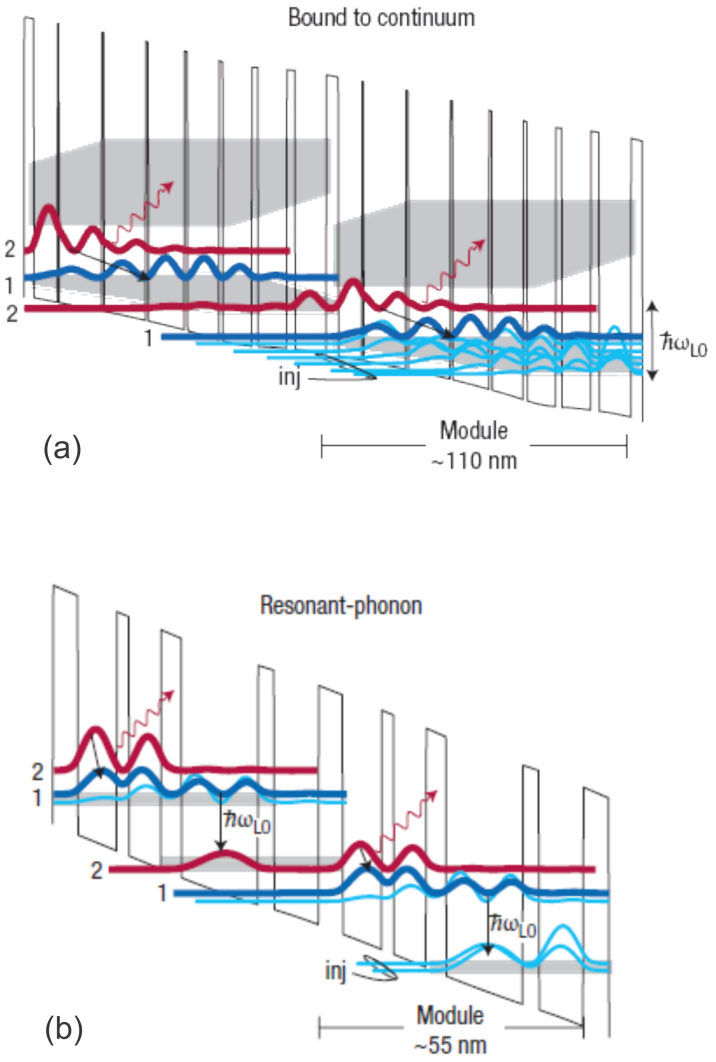

FIGURE 2.13: Conduction band diagram of (a) BTC and (b) RP QCL active region (two identical modules are shown). The squared magnitude of the wave functions for the various sub-band states are plotted, with the upper and lower radiative state shown in red and dark blue, respectively, and the injector states (light blue) specifically labelled. The grey shaded regions correspond to minibands of states [43].

2.5.2 Waveguides for QCLs

There are two types of waveguides used at present for THz QCLs: the semi-insulating surface-plasmon (SI-SP), and the metal-metal (MM) waveguides. It is useful to characterise a laser waveguide: by its loss coefficient, which accounts for scattering and absorption inside the waveguide; its confinement factor, which describes the overlap of the mode with the active region; and, the mirror loss coefficient, which accounts for losses due to optical coupling, usually owing to finite facet reflectivities. These factors determine the required gain to reach the lasing threshold, where the modal gain must equal the total losses [48].

2.5.2.1 Semi insulating surface plasmon waveguide

The SI-SP waveguide involves the growth of a thin heavily doped n+ GaAs layer underneath the active region, but on top of a semi-insulating GaAs substrate and a metal, normally gold Au, layer on top of the active region (Figure 2.14). The result is a compound surface-plasmon mode bound to the top metal contact and the lower plasma layer. The interfaces at the top and bottom of the active region with GaAs form the two plasmon interfaces. The Au and n+ GaAs layers also double up as electrical contacts. Normally, the upper n+ GaAs layer is relatively highly doped compared to the lower GaAs layer. The metal layer at the top provides good confinement on the top side of the waveguide. However, the absence of a metal layer below the lower n+ GaAs layer means that a fraction of the power in the mode is lost via this interface. There is a decaying wave in the substrate that does not contribute to the lasing process. The lack of high confinement means that light can be coupled out of SI-SP waveguides relatively easily compared to other waveguide structures. Surface plasmon waveguide (SPW) QCLs can emit in a single mode (non-Gaussian) despite the fact that the width of the cavity is typically larger than the wavelength of the radiation. Experimentally, low divergence single-spot like beams have been observed. The far field beam profile of SI-SP waveguide THz QCL is non-Gaussian and is not as strongly divergent as that in double metal waveguides where the beam profile is a ring-like interference pattern [49]. Conventional diffraction theory based on Huygens' principle is used to evaluate the the field pattern of SI-SP waveguide considering the aperture as the source. Semi-insulating surface plasmon waveguides for the THz QCLs used in these experiments have a relatively wide gain bandwidth that leads to multiple Fabry-Perot modes

propagating inside the waveguide. A multi mode THz QCL can be made single mode by etching a Bragg grating over the surface of QCL, which leads to removal of unwanted modes. So a Bragg grating i.e. a series of equally spaced metal-stripes on the surface of the QCL ridge, can make the laser to operate in single mode.

2.5.2.2 Double metal waveguide

The alternative to the SI-SP, the double metal (DM) or MM waveguide uses metal layers, which are placed immediately above and below the epitaxial active region by metallic wafer-bonding to obtain a mode almost completely confined to the active region. In a similar fashion to the SI-SP waveguide, the interfaces at the top and bottom of the active region with GaAs form the two plasmon interfaces. In MM waveguide the mode is entirely in the active region. In a double metal waveguide, the presence of a metal layer below the lower GaAs layer prevents the mode from leaking into the substrate. Hence more of the power is confined to the active region of the laser. This high confinement results in very low threshold gains in double metal waveguides, and higher temperatures of operation, compared to the SI-SP waveguide. However, the high confinement in MM waveguides leads to lower output power. Also the fabrication of DM waveguides is relatively more difficult.

2.5.3 Fabrication of quantum cascade lasers

The MQW active region is usually grown using molecular beam epitaxy in the GaAs/$Al_xGa_{1x}As$ material system, and is the heart of any QCL. Commonly used techniques are; molecular beam epitaxy (MBE) and metal-organic vapour phase epitaxy (MOVPE). All the wafers used for measurements were grown using the in house MBE fabrication facility. Also all the grown wafers were processed for experimental measurements using the in in house clean-room facility.

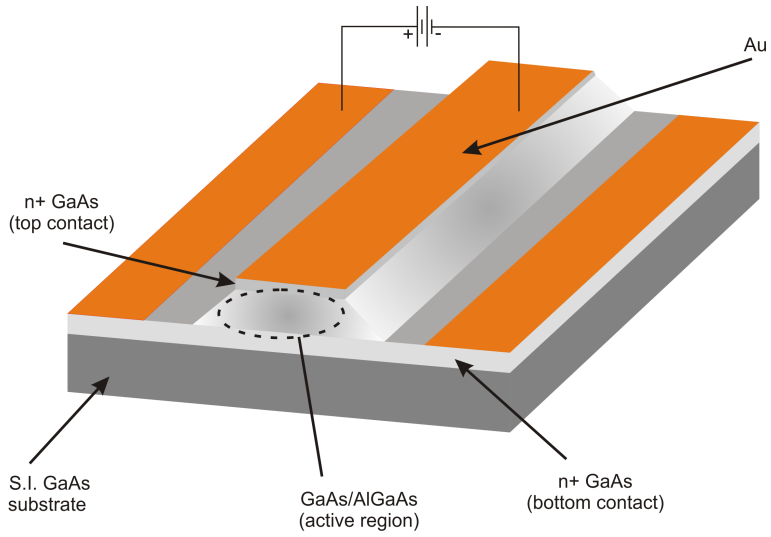

FIGURE 2.14: Schematic illustration of a SI-SP ridge waveguide structure. Such waveguide structures for QCLs consist of a metal, usually gold, and n+ GaAs layers on top and below the active region.

2.6 Summary

This chapter has covered theoretical concepts for a range of topics that provide a comprehensive overview of the systems and components used during the experimental work. To start with, a brief summary of the formation of 2DEGs in GaAs/AlGaAs heterostructures, along with the effect of an externally applied magnetic field B, has been presented. Theory relating to the evaluation of carrier concentration and mobility of a 2DEG sample using QHE measurements has been discussed in detail. The operation of a THz TDS system has been explained in detail, covering both the generation and detection of coherent THz radiation using photo-conductive switches and electro-optic crystals. Finally theory relating to the operation and fabrication of QCLs has been presented.

Chapter 3

Polarisation sensitive detection systems

3.1 Introduction

Conventional terahertz time-domain spectroscopy (THz-TDS) techniques use aligned linearly polarized emitters and detectors for spectroscopy. Birefringent and optically active materials, however, ideally require the measurement of the polarization state of radiation before and after it has interacted with the material [30–35]. Polarization-sensitive THz-TDS can thus provide additional information on material characterisation that is inaccessible through conventional THz-TDS techniques. Specifically, the ability to measure the full polarization state of a propagating THz electric field allows measurement of direction-dependent material properties, (in general described by a tensor) such as the electrical conductivity of semiconductors under applied magnetic fields, or the dielectric permittivity in anisotropic material systems. Indeed, knowledge of the rotation in polarisation caused by a sample is critical for many potential studies of condensed matter systems, such as low-dimensional semiconductors displaying the quantum Hall effect, in which the complex magneto-conductivity is extracted from measurements of the Faraday rotation angle [12].

In order to perform polarization sensitive THz-TDS, it is necessary to be able to measure two electric field components of a THz transient. Theoretically it is possible to do this using a conventional photoconductive receiver. That is; measure one electric field component and then rotate the receiver by 90^0 and measure

the other component. However, in practice this procedure has two major disadvantages: First, during the rotation of the photoconductive receiver, any slight misalignment will significantly shift the relative phase of the electric-field components incident on the receiver; second, the data acquisition time is increased as both components are recorded separately, with mechanical rotation being required.

In this chapter, I will discuss the construction of a free-space time-domain spectroscopy system in which perpendicular polarisations can be measured simultaneously, without the need for mechanical rotation of any components. Two realisations of the system are discussed. In 3.2, the use of a dual polarisation photoconductive detector is discussed. Unfortunately, this detector proved highly sensitive to the precise optical alignment, and not suitable for envisaged system applications. Thus, in 3.3, an alternative approach is discussed based on electro-optic sampling, with separate wire grid polarisers being used to determine simultaneously two orthogonal polarisations. This allows the terahertz properties of a lithium niobate crystal to be measured, results that were published in Appl. Phys. Lett.[89]. The technique is also used in Chapter 5 for measuring the properties of two-dimensional electron systems.

3.2 Polarisation sensitive detection using photoconductive switches

It is possible to measure both components of electric field polarisation simultaneously in a free-space THz-TDS system using a three-contact photoconductive receiver (see Figure 3.1), and this approach, pioneered by M Johnston et al, is investigated [33, 34]. Measuring the cross-polarized extinction ratio can assess the polarization selectivity of such a detector. It should be noted that the polarization of radiation arriving at the detector might not be perfectly linear, as photoconductive emitters do not produce purely dipolar radiation. In fact, it is well known that photoconductive switch emitters produce a small quadrupole field leading to a cross polarized electric-field component. Furthermore, low f-number collection systems inevitably lead to linearly polarized radiation becoming slightly elliptical [57–59]. Therefore, the true extinction ratio of the detector can be higher than the measured one in free space THz-TDS systems.

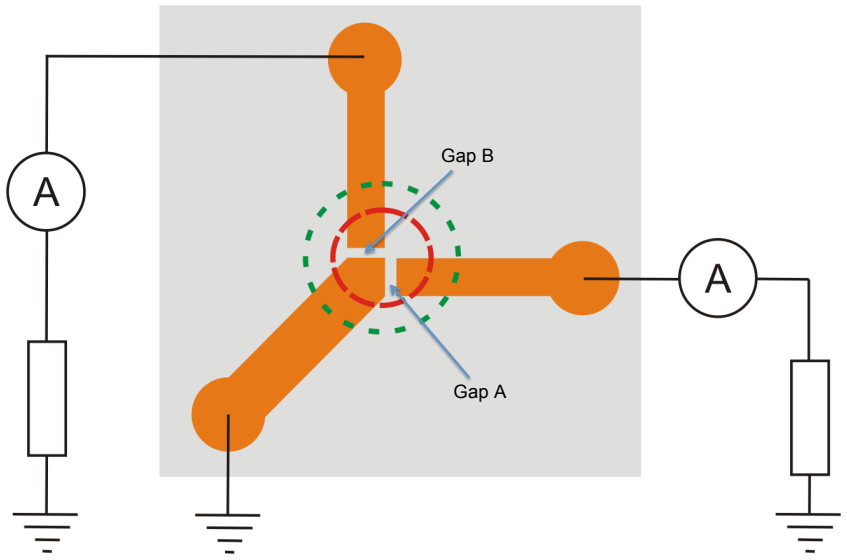

FIGURE 3.1: Operation of integrated three-terminal photoconductive receiver. The probe beam (red circle) from the femtosecond laser is focused onto the centre of the receiver giving equal photocurrent in both switches. The THz beam (green circle) induces photocurrent in the presence of near–infrared radiation across both switches, the relative amounts depending on the polarisation of the THz electric field. In the three terminal detector used both photo-conductive gaps were 50μm wide. Each of the three electrodes was 1mm wide and 1cm long.

3.2.1 Experimental apparatus

The THz-TDS system (Figure 3.2) used for the study of three-contact photoconductive receivers consisted of a pulsed Ti:sapphire laser with a centre wavelength of 830nm, a pulse length of ~150 fs, and a repetition rate of 76MHz. The laser beam was split into pump and probe sections using dielectric beam-splitters.

A time-delayed portion of this beam was used to generate THz pulses from a semi-insulating GaAs photoconductive (PC) antenna, which consisted of two vacuum-evaporated Ti/Au electrodes with an 800μm photoconductive gap. Electron beam evaporation technique was used to deposit 50nm thick electrodes on the substrate surface. A freestanding tungsten wire-grid polariser (wire thickness 20μm, wire spacing 50μm) was used to ensure the polarisation of radiation emanating from the photoconductive switch antenna was linearly polarised. The THz beam was then focused onto the centre of a three-terminal photoconductive receiver (Figure

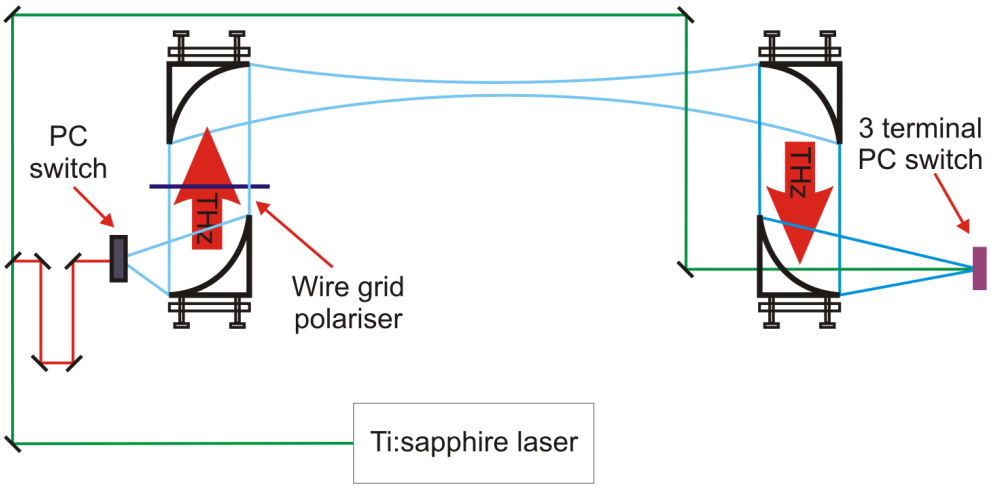

FIGURE 3.2: Experimental apparatus for demonstrating a polarization-sensitive THz-TDS system. THz pulses are passed through a wire-grid polariser to ensure linearly polarised THz beam that is finally focused onto a three-terminal photoconductive receiver for detection.

3.2). For alignment purposes the PC antenna was aligned with the PC gap and electric field vector aligned horizontally. The wire-grid polariser causes only a very small amount of attenuation when the wire-grid is aligned perpendicular to THz electric field.

3.2.2 Terahertz detection

The probe laser beam was focused onto the centre of the three-terminal photoconductive receiver (Figure 3.1), and its position adjusted to ensure the same values of photocurrent from both switches were obtained, when both switches were biased at the same voltage, with photocurrent values of 200μA (gap A) and 209μA (gap B). The DC bias was then removed once it was confirmed that the probe beam was exciting both photoconductive gaps uniformly. THz radiation was next focused onto the centre of the three-terminal receiver (Figure 3.2).

Photo-generated carriers are accelerated across each photoconductive switch according to the direction of the THz electric field polarisation. The induced photocurrent in the two orientations, in the presence of the near-infrared probe beam, was measured using a lock-in amplifier, employing optical chopping for simultaneous detection of the THz radiation. The photoconductive receiver was then rotated through 90^0 to allow a direct comparison between detection from the two

photoconductive arms, with no changes being made to the optical/terahertz alignment. In this measurement, it was ensured that rotation of the photoconductive receiver did not change the relative amounts of laser illumination falling on the two photoconductive switches.

3.2.3 Results and analysis

Typical experimental results, in the absence of a sample, are presented in Figures 3.3 and 3.4. Peak amplitudes were recorded in the time domain in the two orthogonal directions for the same input time domain THz electric field, and the frequency spectrum was obtained in both cases by Fourier transformation (Figure 3.3). The three-terminal photoconductive receiver was then rotated through 90^0, and the measurement repeated. The extinction ratio is defined as the maximum ratio of the signal detected in the time domain by one photoconductive gap to that detected by the orthogonal photoconductive gap. An extinction ratio of 40:1 was determined from the data presented in Figure 3.3 , whilst an extinction ratio of 29:1 was measured when the three-terminal photoconductive receiver was rotated through 90^0. Given these values should, in principle, be identical, this illustrates the critical importance of alignment for this particular type of detection process. It was also observed that the performance of the three-terminal photoconductive receiver was heavily dependent on the laser-intensity noise of the Ti:sapphire laser, as different amounts of fluctuation in photocurrent values were observed for the same photoconductive switch with laser beams (same power) from two different Ti:sapphire laser sources. The optical chopping process used for lock-in detection also compromised the overall signal-to-noise-ratio (SNR) of the free space THz-TDS system by almost a factor of 0.5. The SNR of free-space system was defined as the ratio of the peak Fourier amplitude to the averaged background noise level. In time-domain the ratio of the peak amplitude to the averaged background noise level in the system was used as SNR figure. The output signal from the three terminal detector became very unstable once the optical chopping was employed; the three terminal detector became very sensitive to any spurious reflection in the system. Other contributing factor that further compromised the SNR of free-space system was the laser intensity noise of the fs laser. Because of these issues, the three-terminal photoconductive receiver was not subsequently used for magneto-conductivity measurements of two-dimensional electron gas systems (presented in Chapter 5).

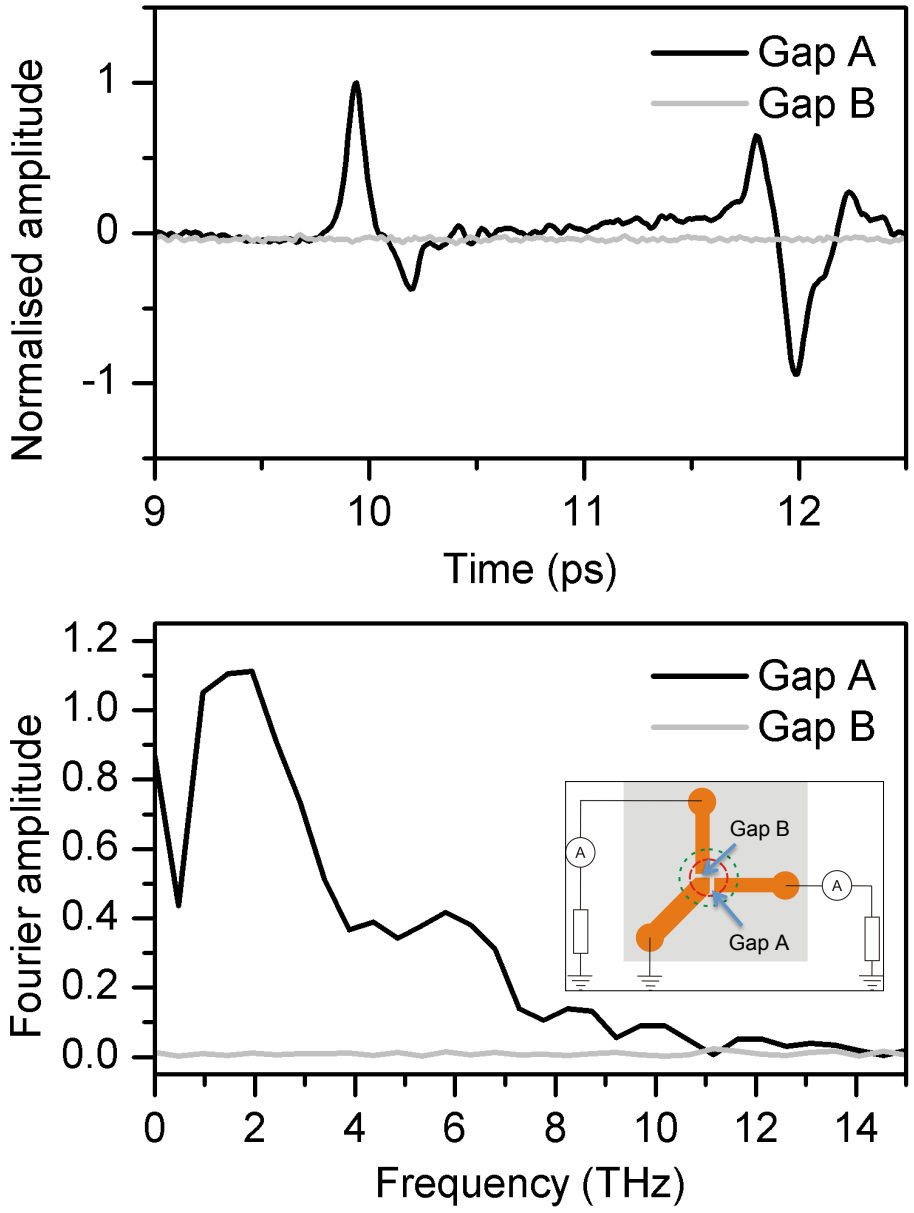

FIGURE 3.3: Polarisation sensitive THz detection, both time (top) and frequency (bottom) domain data. The black line shows the THz electric field across PC gap A, whilst the grey line shows the THz electric field across PC gap B. The extinction ratio of the three-terminal detector was measured to be 40:1 across PC gap A.

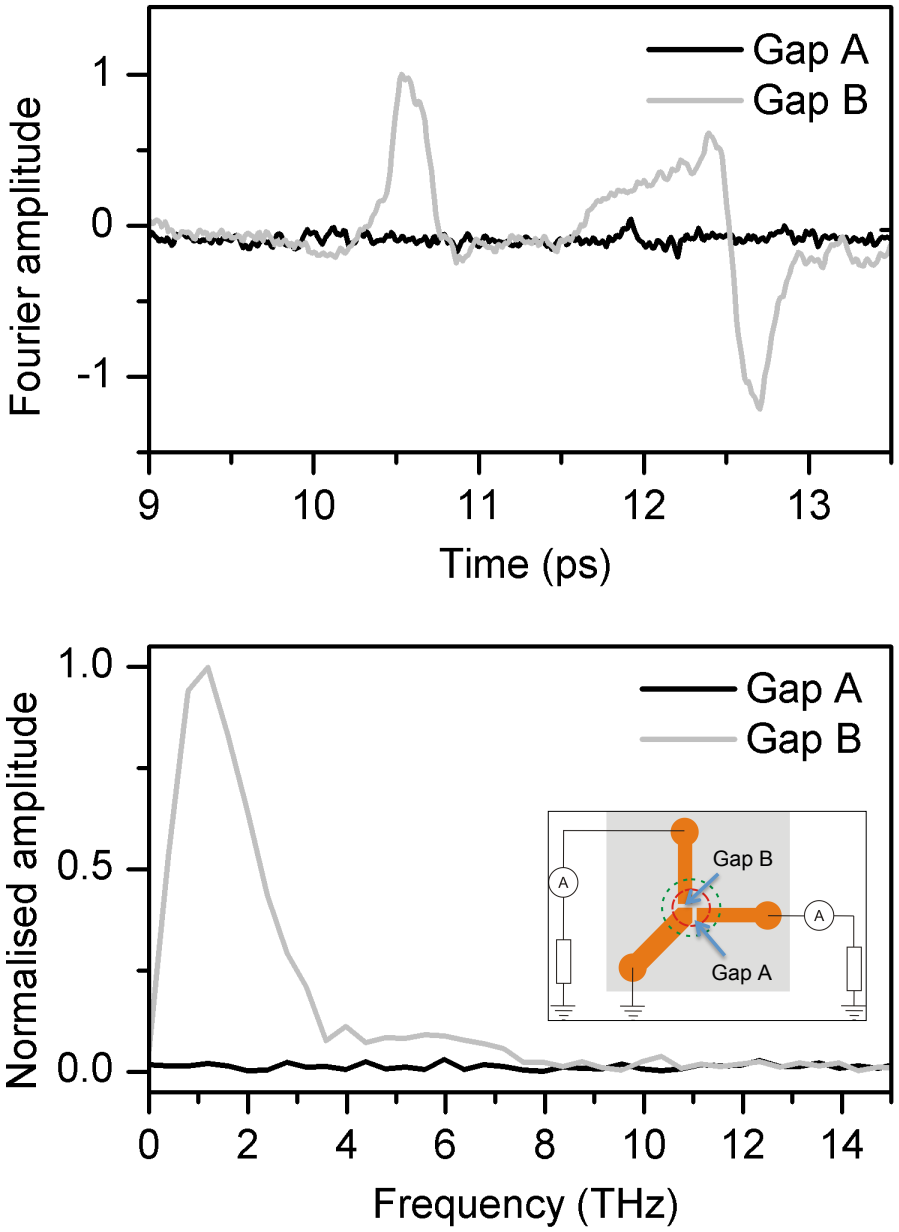

FIGURE 3.4: Polarisation sensitive THz detection, both time (top) and frequency (bottom) domain data. The grey line shows the THz electric field across PC gap B, while the black line shows the THz electric field across PC gap A. The extinction ratio of the three-terminal detector was measured to be 29:1 across PC gap B.

3.3 Polarisation sensitive detection using electro-optic crystals

3.3.1 Experimental apparatus

Owing to the difficulties in obtaining dual-polarisation photoconductive detection [1], an alternative approach was investigated based on electro-optic sampling (Figure 3.5). The system consisted of a pulsed Ti:sapphire laser with a centre-wavelength of 830nm, a pulse length of ∼150fs, and a repetition rate of 76MHz. The fs laser beam was split into three portions, using two beam splitters. The first portion was made incident onto a variable time delay stage, and was then used to generate THz pulses from a semi-insulating GaAs photoconductive antenna, which consisted of two vacuum-evaporated Ti/Au biased electrodes with an 800μm photoconductive gap. The two remaining portions of the laser beam were each used for electro-optic detection by way of two independent electro-optic detectors, each comprising a ZnTe crystal, quarter-wave plate, Wollaston prism, and a pair of balanced photodiodes. The THz radiation emitted by the photoconductive antenna was collimated and then focused through the sample region using two off-axis parabolic mirrors, before being collected and re-collimated by a third off-axis parabolic mirror. A free-standing tungsten wire-grid polariser (wire thickness 20μm, wire spacing 50μm), was then used to split the collimated THz beam into two orthogonal electric field components, each of which was then focused onto its own ZnTe electro-optic crystal, using a fourth and fifth off-axis parabolic mirror, respectively. By changing the position of the delay stage, the time at which THz pulses were received at both electro-optic detectors was simultaneously adjusted with respect to the arrival time of the laser pulses, allowing a time-domain electric field signal to be recorded from both detector branches independently.

3.3.2 Measurement technique

Careful equalization of the THz path lengths and that of the optical path lengths in the two electro-optic detection branches with no sample in place allowed the peak detected THz signal pulse signal from both pairs of balanced photodiodes to occur within the same scan range of the time delay stage. The two signals were then recorded using separate lock-in amplifiers with an optical chopper inserted

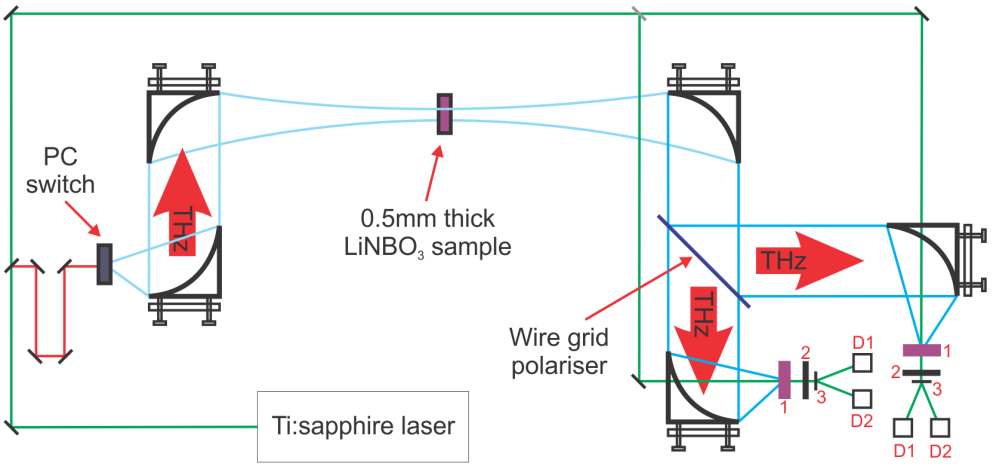

FIGURE 3.5: Experimental apparatus for the polarization-sensitive THz-TDS system. The beam from a pulsed Ti:sapphire laser is split into a pump beam and two probe beams using dielectric beam-splitters. A wire-grid polariser splits the THz beam into horizontal (X) and vertical (Y) components, which are each measured simultaneously by two independent electro-optic detectors (1). Also shown are the quarter-wave plates (2), Wollaston prisms (3) and balanced photodiodes (D1, D2) enabling the electro-optic signal detection.

into the pump beam path providing a reference signal for both measurements. The THz emitter was mounted at an angle of 45^0 with respect to the plane of the optical bench, and a wire-grid polariser (wire thickness 15μm, spacing 60μm) was used to clean up the polarization of the emitted THz waves before their interaction with the sample. The second (beam- splitting) polariser was mounted with its grid lines vertical, thereby separating the THz beam into vertically (Y) and horizontally (X) polarized components in equal proportions. Owing to slight differences in the parabolic mirror focusing and the opacity of the electro-optic crystal used for each beam, the two measured signals were not precisely equal in amplitude, although each was optimized by adjusting the overlap between the focal spots of the laser and THz beams. Rotating the grid lines on the beam splitting polariser by $\pm 45^0$ maximized the signal in one detector while minimizing the other, and vice versa (Figure 3.6). After taking individual Fourier transforms of the signals for each polariser angle (inset to Figure 3.6), the peak amplitudes in the frequency domain were compared, allowing the extinction ratio to be estimated as ~20:1 (at 400 GHz).

The polarization sensitivity of the THz-TDS system was demonstrated by measuring the birefringence of lithium niobate ($LiNbO_3$). With the beam-splitter grid lines returned to the vertical position, a 0.5-mm-thick, polished both sides, 128^0

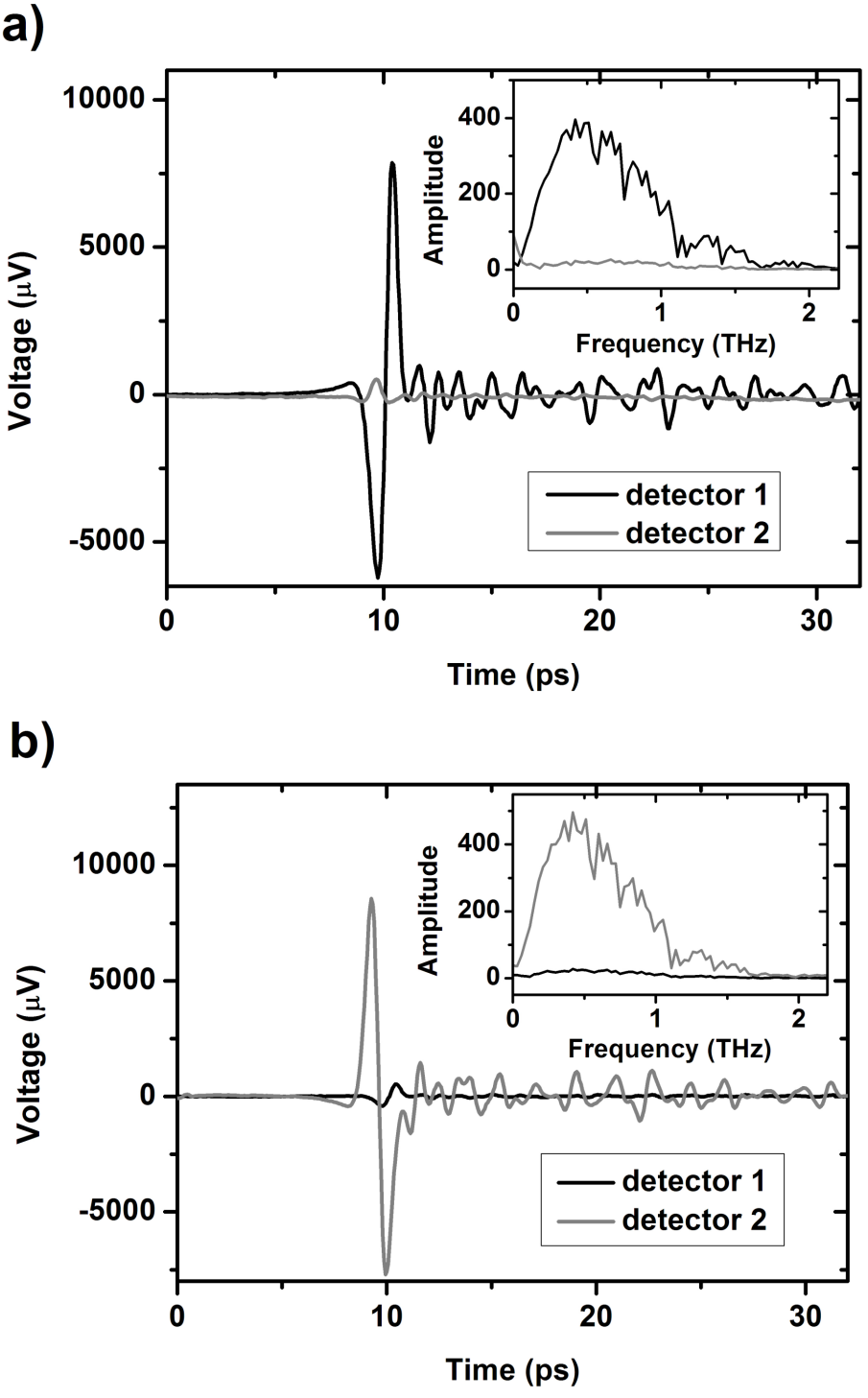

FIGURE 3.6: Terahertz time-domain signals measured simultaneously by the two electro-optic detectors for (a) vertical and (b) horizontal orientation of the grid lines on the second polariser.

Y-cut ($LiNbO_3$) crystal was inserted into the THz- TDS system at the sample position, and mounted on a 360^0 rotation stage with its axis of rotation parallel to the THz beam. To measure the crystal birefringence, it was necessary to locate the directions of the ordinary (o) and extraordinary (e) axes in the plane of ($LiNbO_3$) crystal. This was accomplished by rotating the sample through 360^0 and measuring the corresponding ratio of the x and y electric field components (E_x and E_y). Fourier transformed data was then used to evaluate the values of refractive indices along the ordinary and extra-ordinary axes i.e. n_o and n_e respectively. Fourier transform of the reference time-domain pulses i.e. with no sampl in the THz beam path (Figure 3.6) is used as reference for both polarisation directions. The phase difference, required to evaluate the refractive indices along o and e axes, is obtained by subtracting the reference from the Fourier transformed data for the time-domain pulse with the sample in the beam path. Once the phase difference has been evaluated, following mathematical expression is used to evaluate the absolute values of refractive index.

Mathematically:

$$n(\nu) = 1 + \frac{c\Delta\phi}{2\pi\nu d} \tag{3.1}$$

where c is velocity of light, $\Delta\phi$ is the Fourier phase difference, d is the thickness of the sample (500μm) and ν is the incident radiation frequency i.e. 0.2 – 1.6 THz [90].

3.3.3 Results and analysis

When linearly polarized light enters an anisotropic birefringent crystal, parallel to the principal axis, it does not undergo dual refraction. Anisotropic birefringent crystals behave as isotropic materials under these circumstances. In case when linearly polarized light enters into an anisotropic birefringent crystal at a finite angle to principal axis, it splits into linearly polarized o and e rays with orthogonal electric fields. The o ray travels with the same velocity in all directions while the e ray travels with a velocity that is dependent upon the propagation direction within the crystal.

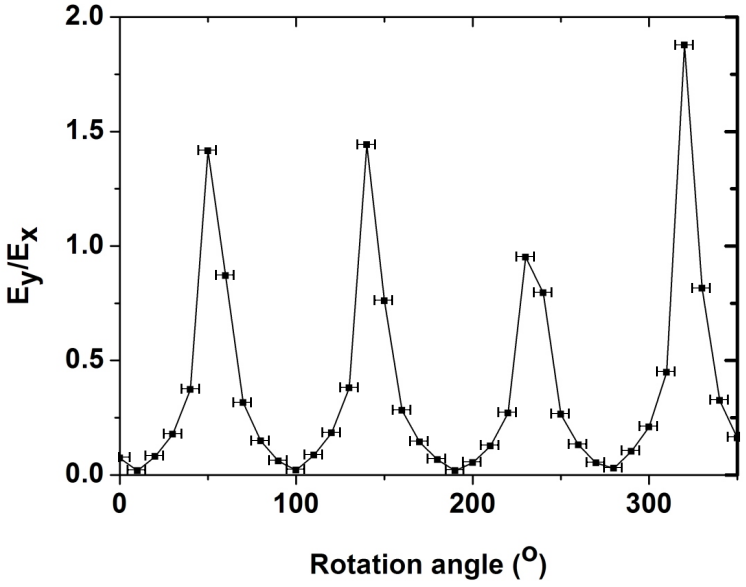

FIGURE 3.7: The ratio E_y / E_x as a function of the sample rotation angle. The constituent E_y and E_x values were taken from the peaks of the individual frequency spectra at ∼400 GHz.

In contrast when linearly polarized light enters the anisotropic birefringent crystal, perpendicular to the principal axis, it is still parted into o and e rays but the propagation direction of o and e rays remains coincident. In this particular case, even though the o and e rays emerge from the crystal at the same location, they exhibit different optical path lengths owing to different amount of phase shift relative to one another.

With the THz electric field vector aligned with either the e or o axis, it should undergo zero rotation on passing through the crystal, corresponding to equalization of the E_y and E_x components. As shown in Figure 3.7 plotting the ratio E_y / E_x as a function of the rotation angle shows that only approximate equalization in E_y and E_x occurs, as the amplitude of the two signals was slightly different owing to slightly different opacities in the ZnTe crystals used, at four equally spaced rotation angles. For these angles (60^0, 150^0, 240^0, and 330^0) in Figure 3.7, the resultant THz electric field is aligned with an optical axis (either e or o), within the experimental error ($\pm 5^0$). A further rotation of the sample by $\pm 45^0$ therefore aligns E_x and E_y individually with one of these axes.

We distinguished between the o and e optical axes by comparing the size of the

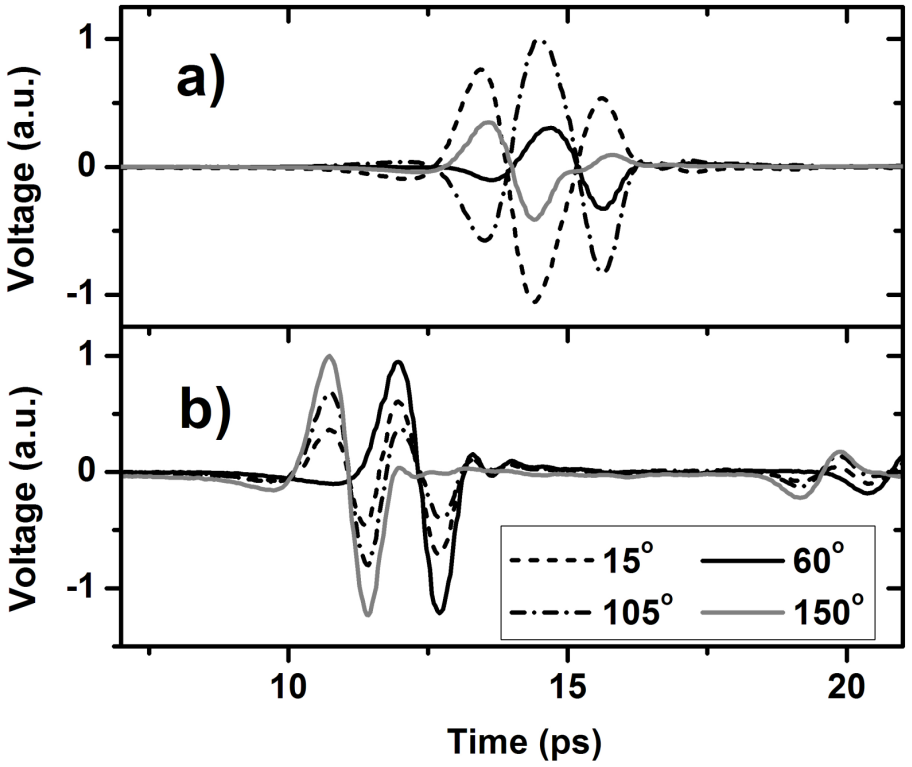

FIGURE 3.8: Time-domain signals measured, simultaneously, with the lithium niobate sample in the beam path, for (a) the X component and (b) the Y component of the THz electric field vector, for the sample rotation angles 15^0, 60^0, 105^0 and 150^0. The horizontal offset between the two components arises from a slight difference in path length between the probe beams.

sample-induced phase shift in each case, the shift being characteristically larger for the o than for the e axis [90]. Figure 3.8 shows the time-domain signals for each field component taken for four different rotation angles, including the two principal axis directions (15^0 and 105^0). The refractive index in each case was extracted from Fourier transforms of these time-domain signals recorded simultaneously by each detector. The size of the sampled time-window used to obtain the Fourier transform was chosen to exclude multiple pulse reflections from the back of the sample. The two refractive indices as a function of frequency are shown in Figure 3.9. We note that the large difference between the THz refractive index observed in the o and e refractive index in our experiment ($\sim$1.5 at lower frequencies) agrees well with measurements of the same quantities obtained by a prior nonsynchronous THz-TDS technique [90]. The absolute values are roughly twice as large as those observed in a previous THz-TDS measurement of birefringence in lithium niobate. The difference in the absolute values can be a direct consequence of the different

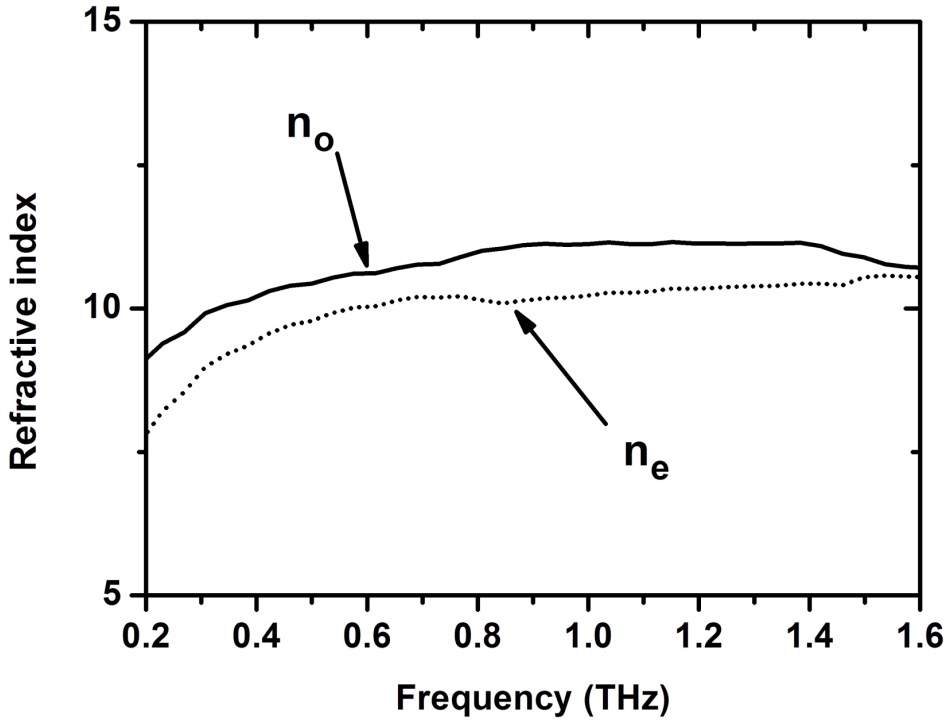

FIGURE 3.9: Data showing the refractive index corresponding to the ordinary (o) and extraordinary (e) axes in the lithium niobate sample, as a function of frequency.

thickness and composition of the samples used. However, since the discrepancy is the same in both indices, it does not imply technical problems in our split-beam setup, but instead points to possible differences in the composition of the samples used in the present work and the earlier measurements.

3.4 Summary

Two different free-space polarisation-sensitive detection systems, both operating at THz frequencies, have been demonstrated. The performance of the THz TDS system with a three-terminal photoconductive receiver was evaluated by the detection of a free space THz signal using lock-in amplifiers across both photoconductive gaps, and determining the corresponding extinction ratio. However, this approach was abandoned, owing to issues related to the alignment of the receiver, laser intensity noise and deterioration of the signal-to-noise ratio of the system caused by optical chopping. Instead, an approach based on electro-optic sensing was used, and this allowed demonstration of polarization sensitive detection of a 0.5mm thick $LiNbO_3$ sample using THz TDS data that has been also reported in App. Phys. Letters [89]. This technique will also be used to measure the magneto-conductivity of a 2DEG in Chapter 5.

Chapter 4

Frequency-domain techniques for measuring the magneto-conductivity of two-dimensional electron systems

4.1 Introduction

There has been extensive recent research on the high frequency (GHz-THz) magneto-conductance properties of two dimensional electron gas (2DEG) systems in order to understand better a range of fundamental physical phenomena such as the frequency/temperature scaling properties of two-dimensional systems in the quantum regime [8–11]; the formation of magneto-plasmons [67–70]; and the origin of microwave-induced magneto-resistance oscillations [91–93]. To investigate such effects at THz frequencies, one can use a time-domain spectroscopy system, where a THz pulse is passed through the 2D systems and sampled coherently in the time domain, with Fourier transformation being used to reconstruct the frequency domain data this approach is taken in Chapter 5 [21–27]. Alternatively, one can measure the frequency domain spectra directly. This can be achieved using Fourier-transform infrared (FTIR) spectrometer, based on a black body source and high sensitivity bolometric detection – this gives a broadband spectral response, which can be measured at specific magnetic fields, but suffers from the low source brightness [13–19]. An alternative approach is to use a fixed frequency, and sweep

the magnetic field. In this case, a high power, single frequency source is used – this might be a free electron laser owing to the traditional lack of high power sources at THz frequencies. In this chapter, however, a high-power laboratory-based source – the terahertz quantum cascade laser, was employed to obtain information about 2DEG systems formed in a gallium arsenide/aluminium gallium arsenide (GaAs/AlGaAs) heterostructure. Results are then compared with those obtained using high power W-band microwave source operating at ∼90 GHz.

Section 4.2.1 describes the techniques used to characterise the four THz QCLs used in this work. These were incorporated into the measuring system described in section 4.2.2. Detailed checks were then undertaken of system stability, with the measurement techniques being presented in section 4.2.3. Results of the QCL measurements are presented in section 4.2.4, with comparisons being made to data obtained at W-band frequencies being given in section 4.3. In both sets of measurements, cyclotron frequencies in the 2DEGs are measured, and the data is compared with simulations based on a Drude model. The chapter concludes with a summary of the key results obtained from making frequency-domain high-frequency magneto-conductance measurements of 2DEGs.

4.2 Free-space THz QCL based system

4.2.1 Characterisation of quantum cascade lasers

In this chapter, four state-of-the-art QCLs are used – two based on bound-to-continuum (BTC) active region designs, and two-based on resonant-phonon (RP) depopulation they operate at around 2.6 and 3.1 THz respectively. All QCLs used a semi-insulating surface plasmon (SI-SP) waveguide both to enhance the output coupling from the active region, and to ensure a well-defined far-field beam profile, which can be focused with subsequent terahertz optics.

The QCLs were characterised using a FTIR spectrometer. Only the power spectrum for each device was recorded, since knowledge of the absolute peak power was not required. During operation, the QCLs were cooled to the base temperature of 5K of a continuous-flow cryostat. Current pulses were then supplied to the QCL at a frequency of 10 kHz and a duty cycle of two percent with lock-in detection at 167 Hz being employed to improve the detection sensitivity. Radiation from

Wafer Number	Active Region Design	Frequency	Mode of Operation
		(THz)	
L559	RP	3.1	Multi
L173	BTC	2.6	Multi
L173	BTC	2.8	Single
L674A	RP	3.2	Single

TABLE 4.1: Characterisation data of four QCLs used in experiments. The two active region designs used are resonant phonon (RP) and bound to continuum (BTC).

the QCL was collected through an optically transparent window, collimated using 2 off-axis parabolic mirror, and directed towards a beam splitter using off-axis parabolic mirrors. Half of the coherent radiation hitting the beam splitter was reflected towards the fixed mirror while the other half went through the beam splitter towards the moveable mirror. Light from both mirrors was reflected back towards the beam splitter and then focused on to the centre of the helium-cooled bolometer (Figure 4.1). Power spectra of QCLs were measured by changing the position of the moveable mirror. A zero path-difference between two reflected beams leads to a maxima in the detected signal amplitude. A Fourier transform is then used to convert the spectra from length to wave-number domain. For high-resolution spectra, the moveable mirror is translated with very small increments. The spectral resolution is equal to the reciprocal of the step-size used for the moveable mirror (e.g. a 0.5μm step size gives a spectral resolution of 2/μm or 20000/cm). Measured spectra of four QCLs are presented in figures 4.2, 4.3 and 4.4 for a range of temperatures and bias currents, and the results from each of the four THz QCLs are listed in Table 4.1. All the wafers (QCLs and HEMTS) were grown using the in house molecule beam epitaxy (MBE) fabrication facility. Also all the grown wafers were processed for experimental measurements using the in in house clean-room facility. Characterisation data of two BTC THz QCLs made from the same wafer (L173) is shown in figs. 4.3 and 4.4, with one device having the Bragg grating and operating in single mode at 2.8 THz.

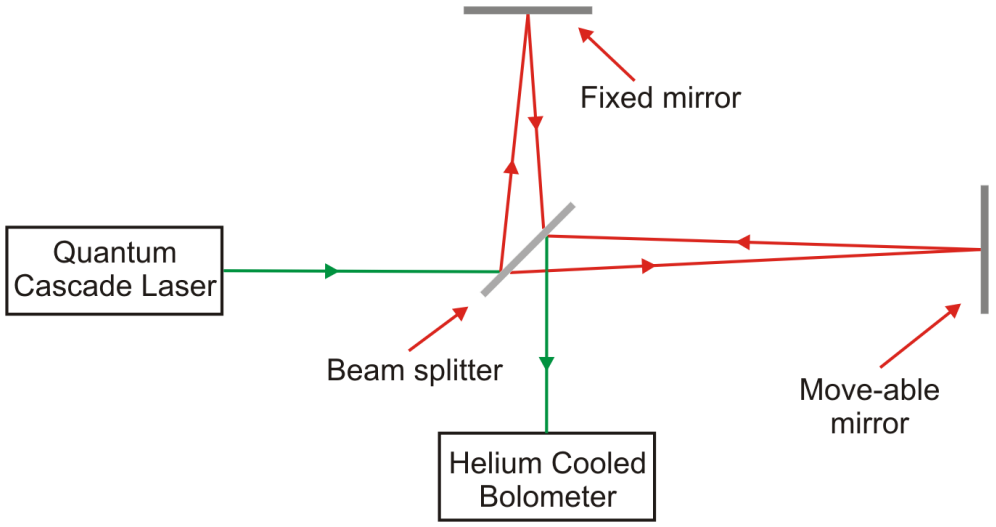

FIGURE 4.1: Overview of the optics, based on a Michelson interferometer, used inside a FTIR spectrometer to measure the spectra of a radiation source. Radiation from the QCL is split into two different beams and is directed towards fixed and moveable mirrors respectively. Based on the path difference between the two reflected beams from the fixed and moveable mirror, the power spectrum of each QCL was measured. An interference pattern is formed on the surface of the beam splitter owing to the overlap of two incoming beams from the fixed and moveable mirrors, and through changing the position of the moveable mirror an interferogram is built up. Fourier transforming the data can recover the frequency spectrum of the source.

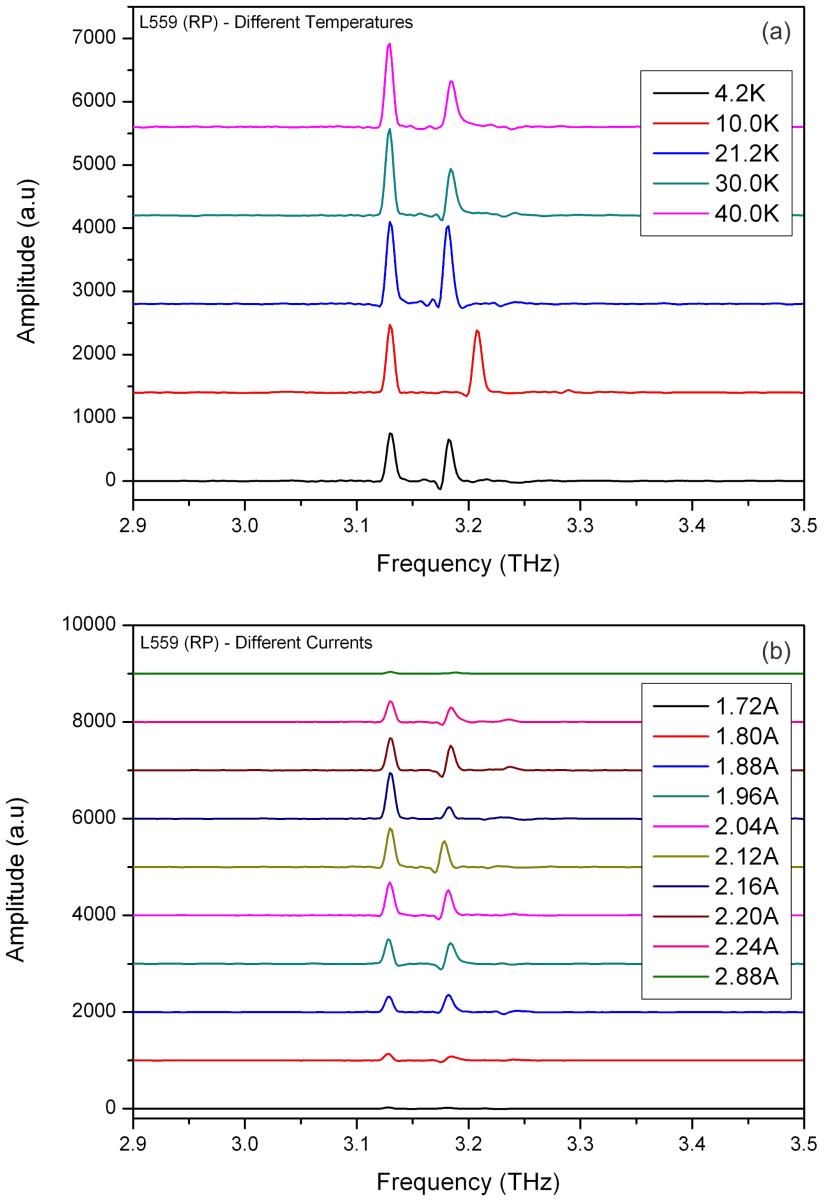

FIGURE 4.2: Experimentally measured spectra for L559 QCL, based on an RP active region design, for a range of (a) temperatures (4.2–40 K) and (b) bias currents (1.72–2.88 A). Spectra offset vertically for clarity.

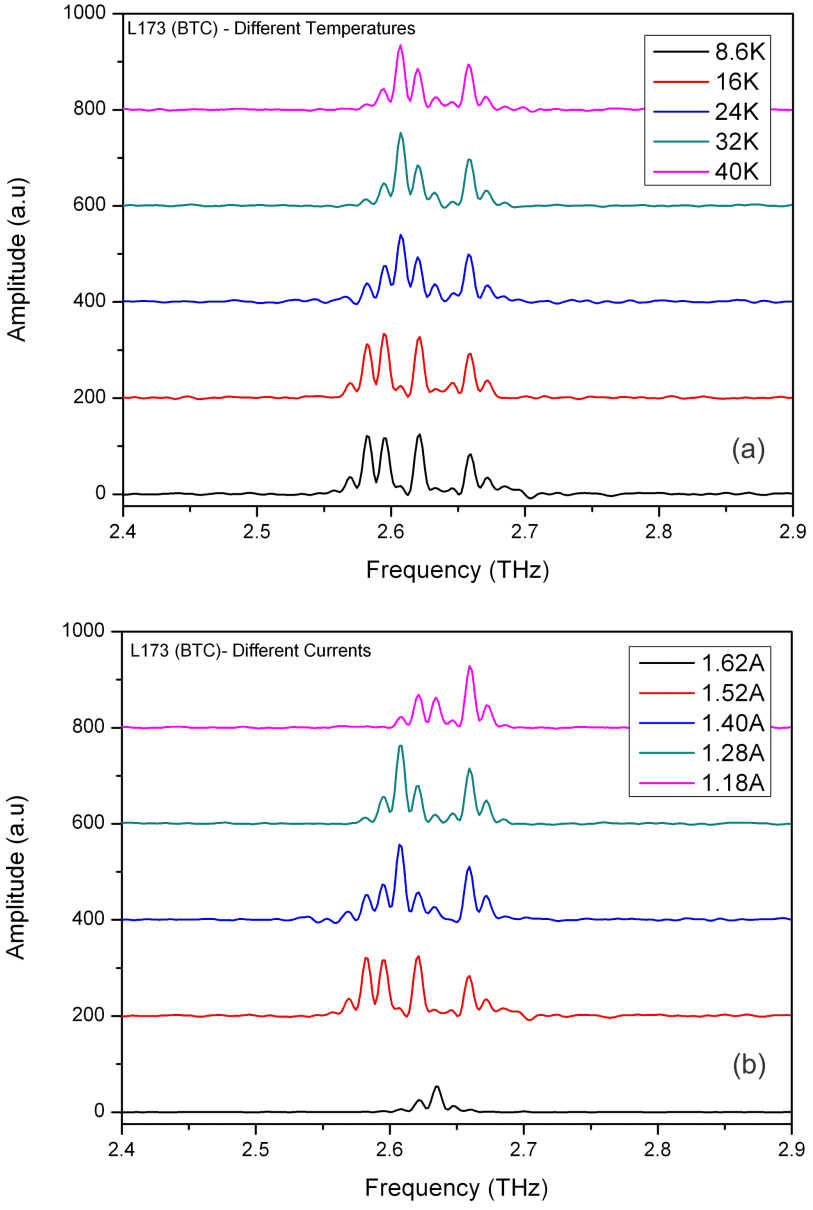

FIGURE 4.3: Experimentally measured spectra for L173 QCL, based on BTC active region design, for a range of (a) temperatures (8.6–40 K) and (b) bias currents (1.18–1.62 A). Spectra offset vertically for clarity.

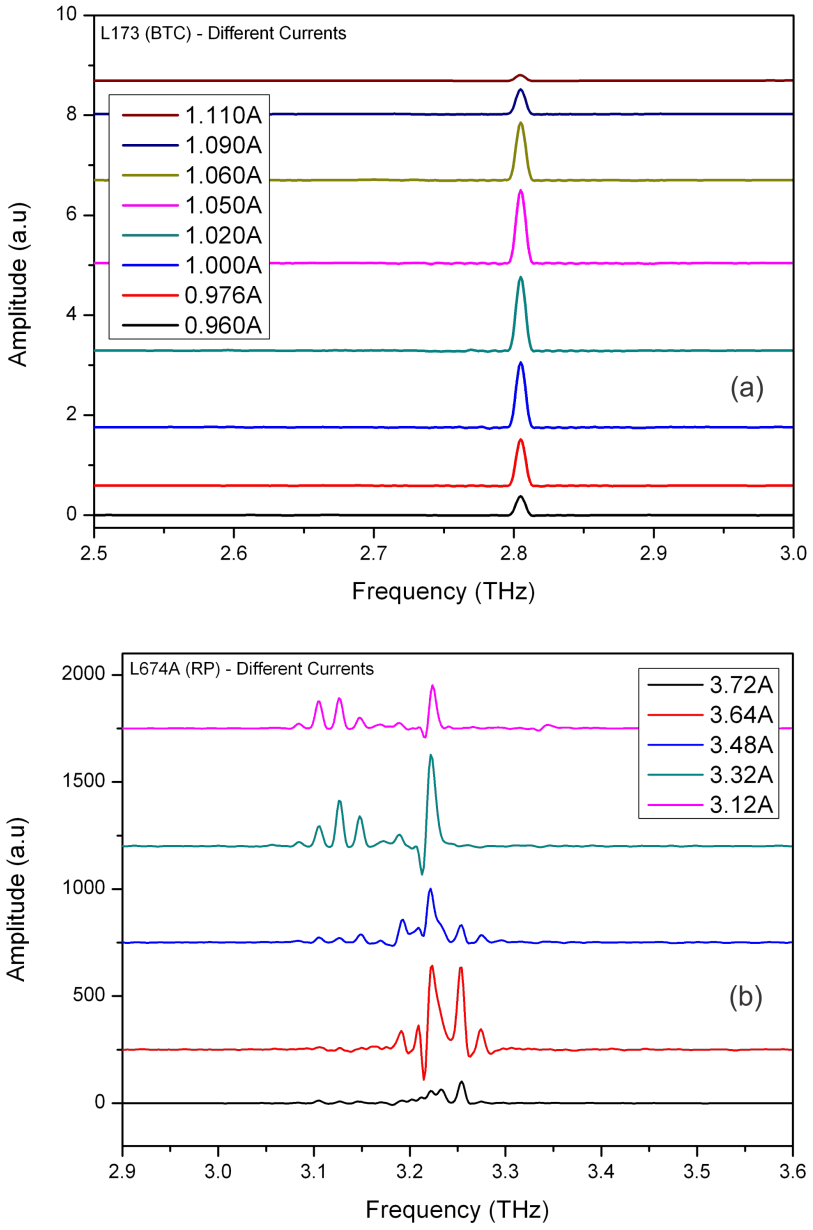

FIGURE 4.4: Experimentally measured spectra at different bias currents for (a) L173 – a BTC QCL with a Bragg grating (0.96–1.11 A), and (b) L674A – an RP QCL (3.12–3.72 A). Spectra offset vertically for clarity.

4.2.2 System design

Having characterised a range of THz QCLs, and determined their emission wavelengths, a system was designed for measurement of 2DEG samples (Figure 4.5). First, a wire-grid polariser was placed in the path of the collimated beam from the THz QCL to ensure a linearly polarised electric field in the plane of the 2DEG sample. The collimated beam was then focused onto the 2DEG sample, which was mounted on a sample probe inside an optical-access cryostat, which had a base temperature of 1.4K. Here, a superconducting magnet provided a magnetic field (perpendicular to the plane of the 2DEG) in the range of 0 to 8T. After transmission through the 2DEG, the THz radiation was collected and collimated by another off-axis 2 inch parabolic mirror. A second wire-grid polariser was then placed in the collimated beam path, which enabled measurement of both diagonal and off-diagonal parts of the 2DEG conductivity independently. The collimated beam was, finally, focused on to the centre of helium-cooled bolometer for detection. Current pulses were supplied to the QCL at a frequency of 10 kHz and a duty cycle of 2 per-cent with lock-in detection at 167 Hz being employed to improve the detection sensitivity. A visible helium-neon (He-Ne) laser was used initially to verify the alignment of all optical components present in the free-space system.

All optical components used in the free-space system were non-magnetic. Nevertheless, in order to verify the stability of the free-space system, the THz signal from the QCL was continuously monitored and recorded while the magnetic field was ramped up from 0 to 8T, with a step size of 0.01T, and then stepped back to 0, in the absence of a 2DEG sample. This confirmed that optics did not change their position as the magnetic field was swept, since complete reproducibility of the signal was obtained between the traces upwards and downwards. This process was repeated twice in order to verify this repeatability categorically. Two 2DEG samples were then tested, each sample having dimensions of 1.5 x 1.5 cm. Ohmic contacts to the 2DEG allowed characterisation of the DC magneto-conductivity to be performed, before and after the THz transmission data acquisition, which provided verification that the 2DEG carrier concentration remained constant throughout the THz measurements.

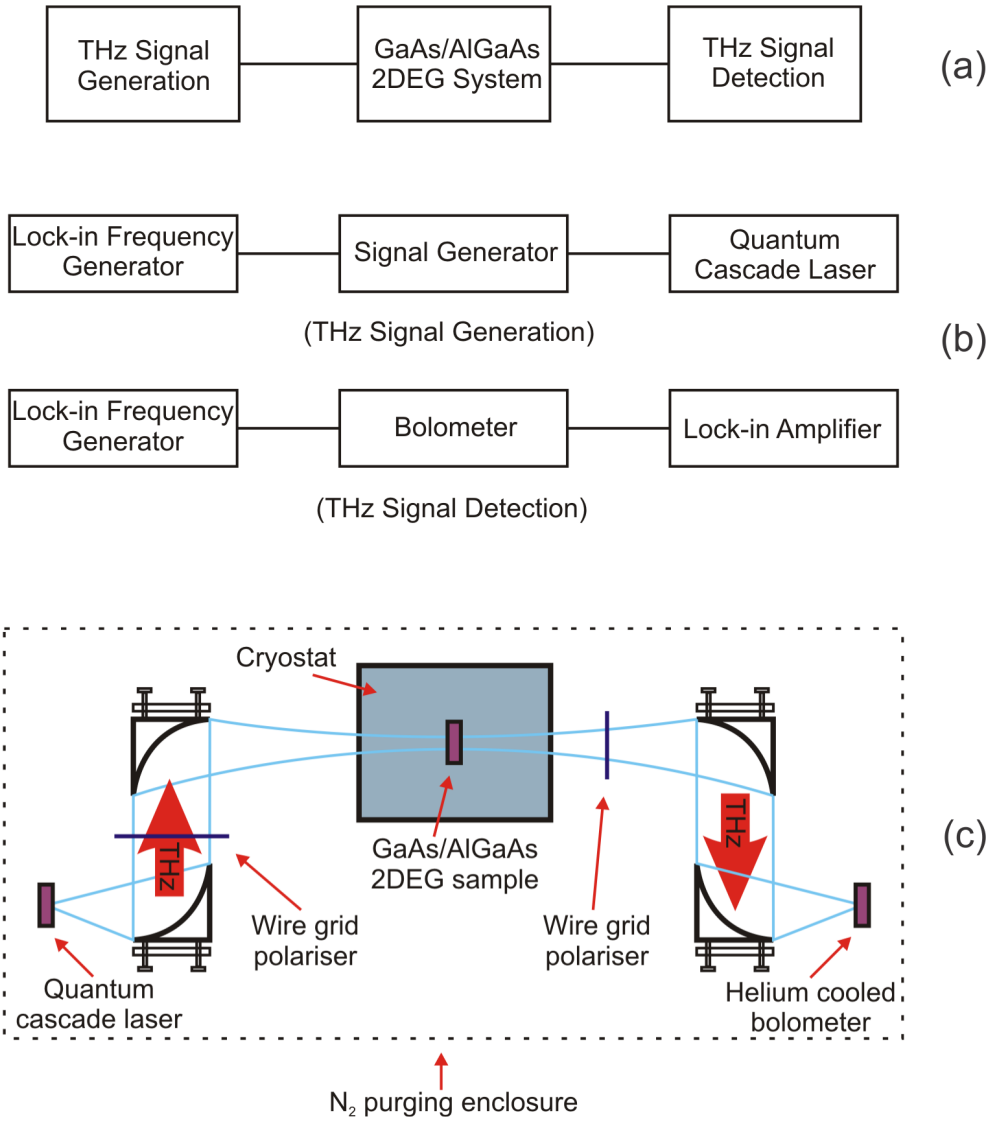

FIGURE 4.5: Free-space QCL based system to evaluate the conductivity of the 2DEG in a GaAs/AlGaAs heterostructure. (a) Block diagram of the free space system. (b) THz signal generation and detection processes. 10 kHz pulses with a two percent duty cycle and external modulation at 167 Hz drive the QCL. The signal from the bolometer is detected at 167 Hz using a lock-in amplifier. (c) Experimental setup for the free space system. Radiation from the QCL is focused on to the sample inside the cryostat at 1.4K. Wire-grid polarisers are placed before and after the cryostat to ensure linear polarisation and ensure that only a single polarisation is measured after passing through the 2DEG sample, respectively.

DC characterisation was repeated with THz radiation being transmitted continuously through the 2DEG in order to verify that no change in carrier concentration arose owing to the presence of THz in the free space system. Both the QCL and bolometer were also positioned as far away from the superconducting magnet as possible in order to avoid any change in their performance caused by the presence of a strong magnetic field– none was detected in the reproducibility studies undertaken above.

Small Hall bars were characterised from the same wafers in order to verify that DC conductivity measurements of the large square samples used for THz measurements gave equivalent results to those obtained in the more standard Hall bar geometry. Shubnikov-de Haas oscillations were measured from both samples, and the 1/B periodicity was found to be identical. For all measurements, dry nitrogen gas was used to purge the system in order to avoid any THz absorption by water vapour. The windows of the cryostat were covered with black plastic sheets in order to block visible light, hence avoiding any carrier excitation caused by the presence of visible radiation from valence to conduction band or from the doping layer to the 2DEG. The presence of these plastic sheets in the THz beam path resulted in a negligibly small attenuation of signal amplitude.

4.2.3 Measurement techniques

The Van der Pauw method was used for DC characterisation of large square samples (illustrative data is given in Figure 4.6). To characterise the THz properties of the sample, the signal detected by the bolometer was measured; this gives information on the real part of the 2DEG conductivity. The diagonal component was measured by placing the wire-grid polariser, orthogonally aligned to the electric field vector of the incoming terahertz radiation, in the beam path before the bolometer. The real part of the off-diagonal conductivity component was then measured by rotating the polariser through 90^0, hence suppressing the transmission signal at zero magnetic-field to the background thermal noise level (NB the absence of phase information, using this measurement technique, prevents the imaginary part of the conductivity being evaluated).

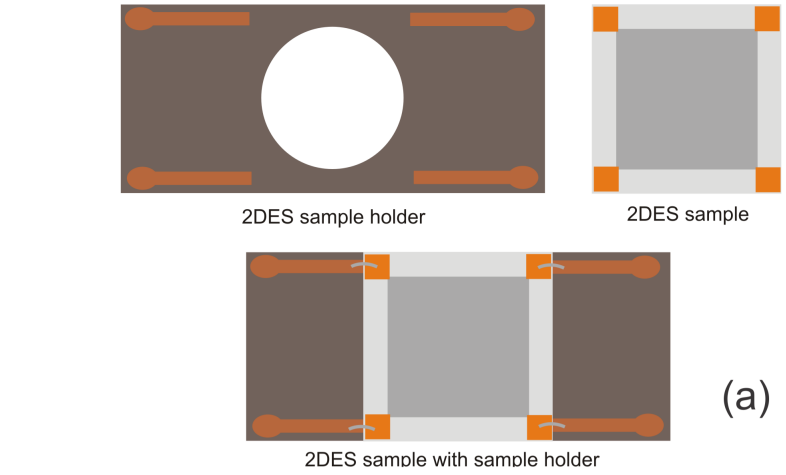

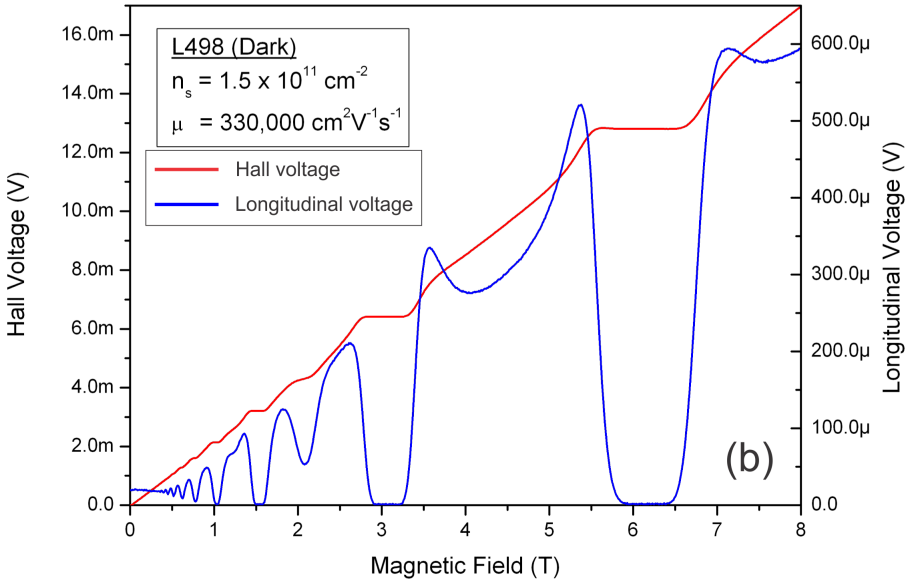

FIGURE 4.6: DC characterisation of 2DEG under test. (a) 2DES large square sample (0.9 x 0.9 cm) on top of a sample holder. Four ohmic contacts allow simultaneous DC magneto-conductivity measurements to be carried out during the free space transmission measurements. (b) DC characterisation data for L498 in the dark at 1.4K for a magnetic field range of 0 to 8T. Carrier concentration and mobility values for this sample are $1.5 \times 10^{11}/cm^2$ and $330,000 cm^2/Vs$ respectively, obtained using the Van der Pauw technique.

Drude model equations [25] were used to simulate the conductivity of the 2DEG at the QCL frequencies used for these transmission measurements.

$$\sigma_{xx} = \frac{\sigma_0}{1 + 2\pi i(\omega - \omega_c)\tau} \tag{4.1}$$

$$\sigma_{xy} = \frac{\sigma_0 \omega_c \tau}{(1 - i\omega\tau)^2 + (\omega_c \tau)^2} \tag{4.2}$$

Here σ_{xx} is the diagonal conductivity while σ_{xy} is the off-diagonal conductivity. σ_0 is the DC conductivity measured at 0.08T, ω is angular frequency, τ is the scattering time and a fitting parameter in simulations and ω_c is the cyclotron resonance (CR) frequency.

4.2.4 Results and analysis

Values of the carrier concentrations and mobilities of the 2DEG samples used in these measurements are given in Table 4.2, with representative DC magneto-resistance data, for a sample with a carrier concentration and mobility of $1.5 \times 10^{11}/cm^2$ and $330,000 cm^2/Vs$, respectively, being given in Figure 4.6. It can be observed from table 4.2 that DC characterisation data is similar for both small and large samples as expected. Also the values of carrier concentration and mobility increase as the sample is illuminated using a red light source as expected (see section 2.2).

Results from the THz transmission measurements are presented in figures 4.7 – 4.12. Initial experiments investigated the transmission through the 2DEG over a wide range of magnetic fields in order to search for the appearance of any features other than CR; the features being the observation of the quantisation of Hall resistance at THz frequencies and observation of THz induced oscillations in the magneto-conductivity of 2DEG. The absence of any such features, for both diagonal and off-diagonal parts of conductivity, resulted in the measurements being focused around the CR region of magnetic field. The presence of the first wire-grid polariser in the free space system, between the first and second parabolic mirrors, ensures that a linearly polarised terahertz electric field is directed towards the 2DEG sample inside the cryostat.

Large Square Samples

HEMT Sample	Experimental Condition	Mobility $(cm^2V^{-1}s^{-1})$	Carrier Concentration (cm^{-2})
L445	Dark	80,000	1.0×10^{11}
L498	Dark	330,000	1.5×10^{11}
L445	Light	150,000	1.9×10^{11}
L498	Light	537,000	2.5×10^{11}

Small Hall Bar Samples

L445	Dark	77,000	$0.9times10^{11}$
L498	Dark	338,000	1.5×10^{11}
L445	Light	146,000	1.8×10^{11}
L498	Light	540,000	2.6×10^{11}

TABLE 4.2: The DC characterisation data of L445 and L498, two different 2DEG samples, used in the transmission measurements at 1.4K and 0.08T. Hall bars made out of same wafers were also characterised to ensure 2DEG sample uniformity.

The terahertz signal from the QCL was recorded for different angular orientations of the first wire-grid polariser, without the 2DEG or the second wire-grid polariser present in the system (Figure 4.7). It can be seen that the amplitude of the bolometer signal drops sharply as the wire-grid polariser is rotated. This clearly shows the presence of a linearly polarised electric field arising from the QCL.

Figures 4.8 and 4.9 show the results obtained from a 2DEG sample (L498) inside the cryostat, both with and without a second wire-grid polariser present in the system, respectively. Figure 4.8 clearly shows the presence of cyclotron resonance, with the expected net drop in signal amplitude, followed by a peak resulting from the presence of the off-diagonal component of cyclotron resonance (Figure 4.8) – in the absence of a second polariser, the diagonal and off-diagonal components are not distinguished. The presence of the 2DEG sample in the THz beam path thus causes polarisation rotation of the incoming electric field. The effect of illumination i.e. when the 2DEG sample is illuminated with a coherent red light source (He-Ne Laser) is shown in Figure 4.9.

The observation of a peak in transmission through the 2DEG in Figure 4.8 can

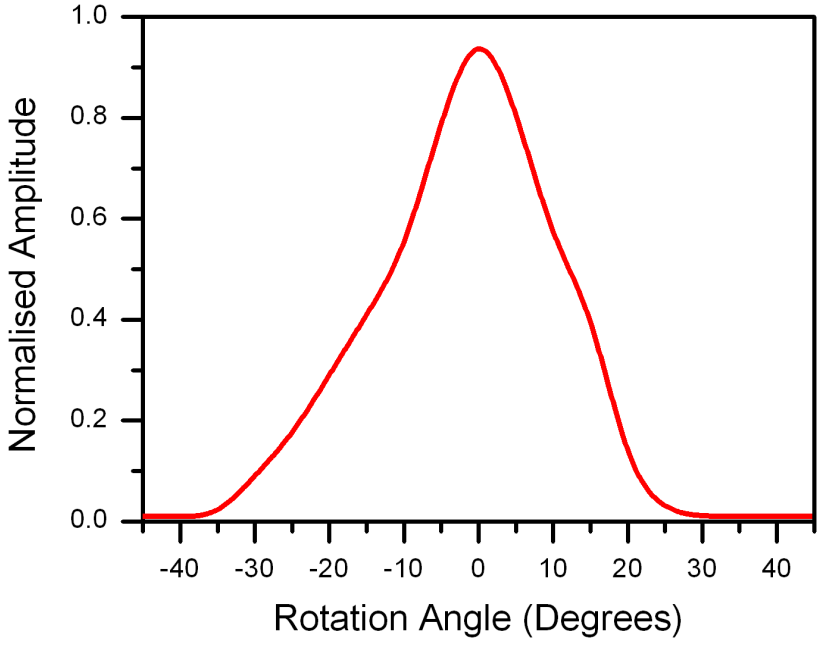

FIGURE 4.7: Polarisation test of the THz radiation generated by a QCL. The zero-degree position corresponds to the orientation of the wire-grid polariser being orthogonal to the incoming radiation form the QCL. The THz signal on the bolometer was recorded as the angular position of the wire-grid polariser was changed.

be attributed to the CR associated with the off-diagonal conductivity. When the 2DEG sample is illuminated with a red light source, electrons are transferred into the one-dimensional potential well in the growth direction, leading to an increase in carrier concentration and mobility. This effect can be noticed in the data plotted in Figure 4.9 (where a second polariser allows the separate diagonal and off-diagonal components to be measured). The width and peak of the CR change as the carrier density and mobility of the 2DEG change. Changes in the full-width-at-half-maximum (FWHM) of the CR can be directly associated with mobility of carriers in the 2DEG, while the peak amplitude of the CR is associated with the number of carriers present. As the mobility of carriers inside the 2DEG increases, it leads to resonant absorption of narrowband of frequencies resulting into a net decrease in the FWHM of CR. Also with the extra electrons inside the 1D well, there will be more energy absorption during the resonant transition leading to a much higher CR peak.

Four different QCLs were used for free-space transmission measurements, operating at around 2.6 (L173), 2.8 (L173), 3.1 (L559) and 3.2 (L674A) THz respectively

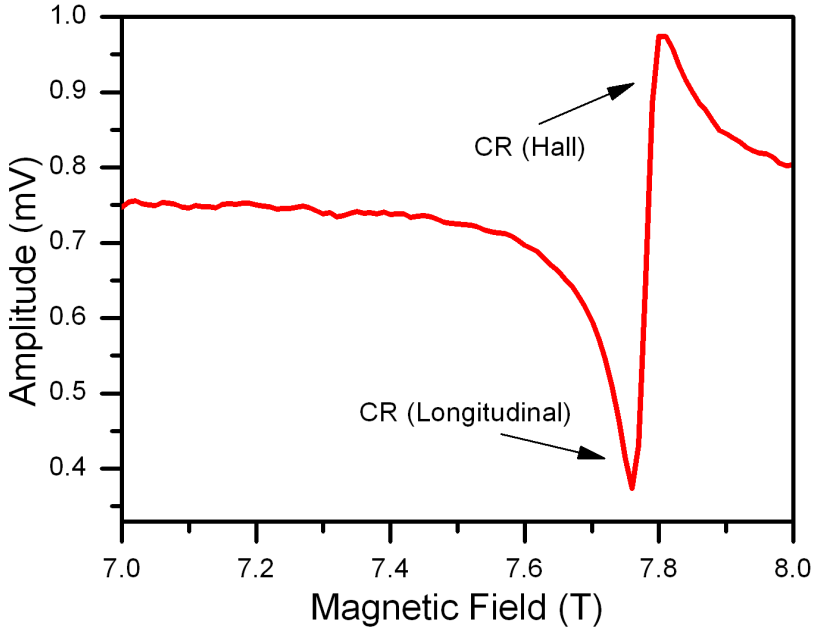

FIGURE 4.8: Measurement of the conductivity in the absence of a second wire-grid polariser. Both diagonal and off-diagonal components of cyclotron resonance appear simultaneously in the transmission data.

(table 4.1). Only one QCL used was a single mode device while the other three QCLs were multi-mode devices (Figures 4.2 – 4.4). The presence of single or multiple modes can be attributed to the wave-guide structure of the particular device, and whether a Bragg grating was incorporated or not. It has been observed that the presence of multi-modes, with comparable amplitudes, results in extra features appearing with the CR peak, whilst a Lorentzian shape CR signal was observed when the QCL had one dominant mode i.e. a mode with a much higher amplitude (Figures 4.9 and 4.10). Figure 4.11 shows the evaluation of the effective mass in the 2DEG from the transmission data at the four different frequencies, with an effective mass of $0.068^{*}m_0$ being used to fit the f vs B experimental data. The presence of the second wire-grid polariser, in the free space system, enables the measurement of the off-diagonal conductivity as well as the diagonal conductivity. Plots of both diagonal and off-diagonal parts of conductivity are shown in figures 4.12 and 4.13 for L445 and L498, respectively, along with Drude model fits using equations 4.1 and 4.2 respectively. All the fitting was done using Matlab. The Drude model also shows the presence of an interesting feature in the experimental data – the CR is not wholly Lorentzian, unlike simulated data. This particular feature has not been observed in time-domain spectroscopy (TDS) data for similar

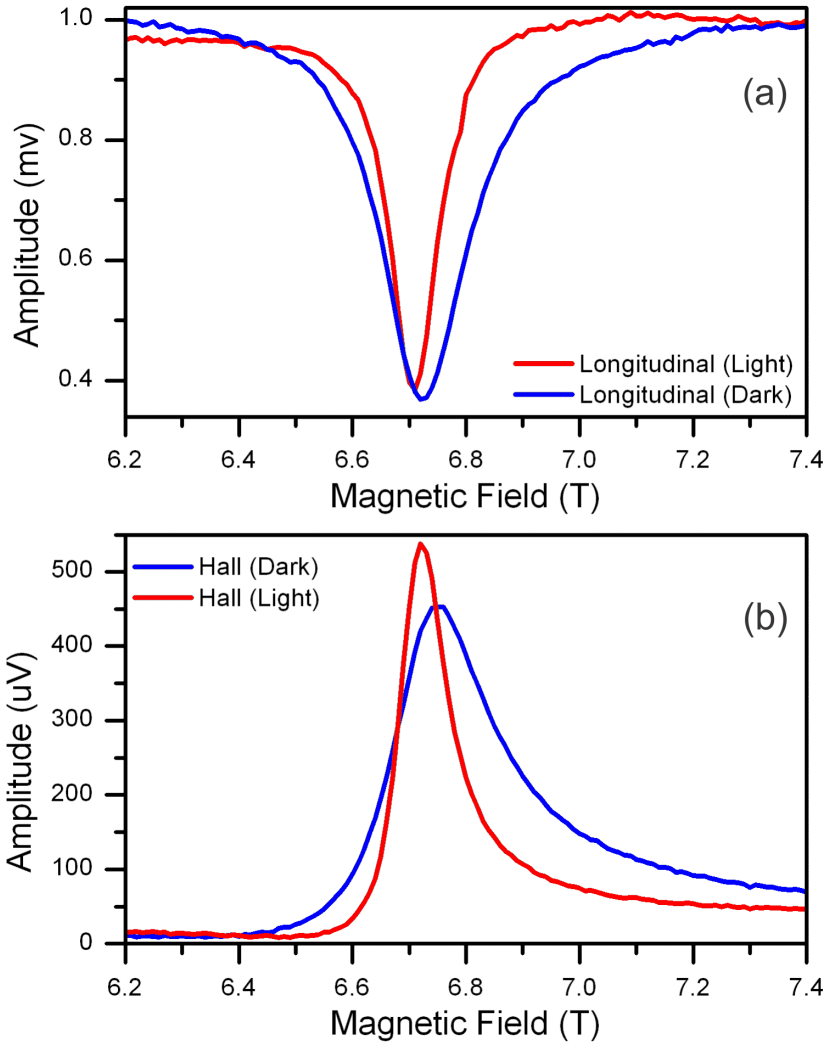

FIGURE 4.9: Effect of changing the carrier concentration and mobility of a 2DEG (L498) at 1.4K and 3.2 THz (L559). When the sample is illuminated, both carrier density and mobility increase leading to a net decrease in the width of the cyclotron resonance. (a) Transmitted diagonal component with the second wire-grid polariser present in system both before (blue line) and after (red line) illumination with a red light. (b) Transmitted off-diagonal component with the second wire-grid polariser present in the system both before (blue line) and after (red line) illumination.

2DEGs over a much wider frequency range of 75 GHz to 1.5 THz (chapter 5). To interpret this more thoroughly, further investigation is required where the CR is measured for 2DEGs with a broad range of carrier concentrations and mobilities, at different temperatures.

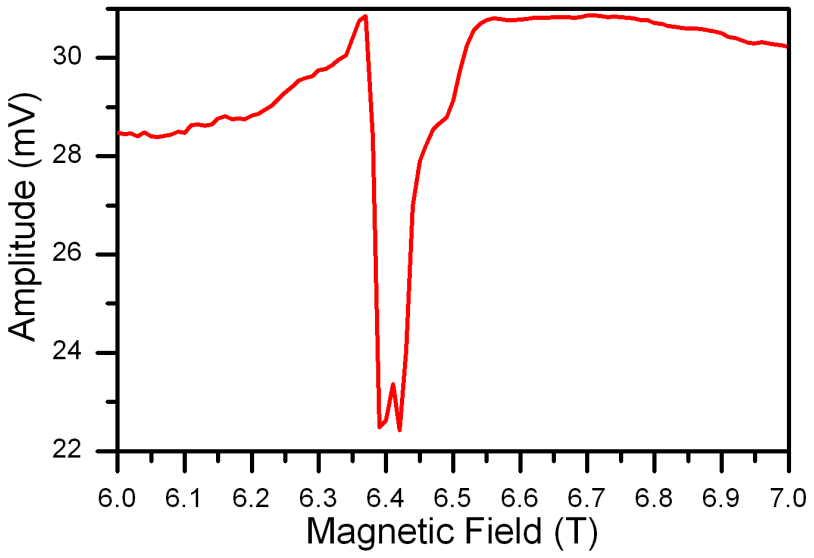

FIGURE 4.10: Transmission through a 2DEG using a multi-mode QCL (L173) operating around 2.6 THz. The presence of many modes, with comparable power spectra, results in an extra feature appearing along with the CR.

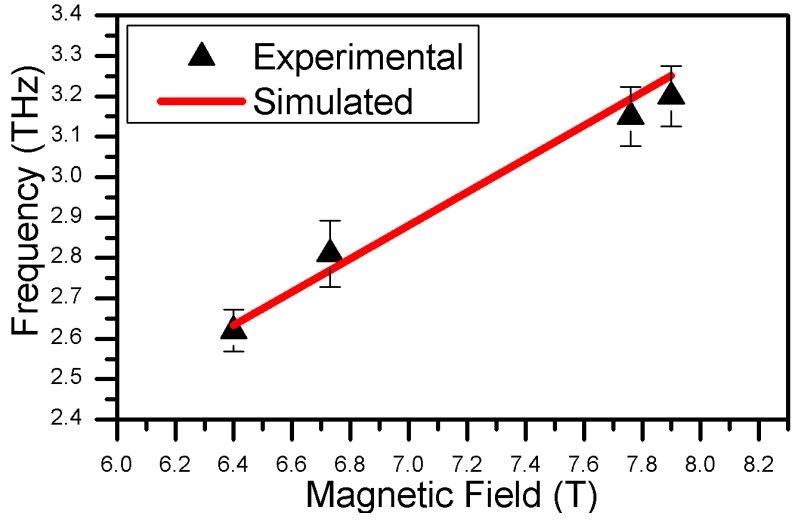

FIGURE 4.11: f vs B plot to extract effective mass from the experimental data obtained using four different QCLs operating at 2.6 (L173), 2.8 (L173), 3.1 (L559) and 3.2 THz (L674A) respectively, with the 2DEG sample at the base temperature of 1.4K. An effective mass of $0.068 \pm 0.002 * m_0$ has been extracted by fitting $\omega_c = eB/m_0A$ to the experimental data.

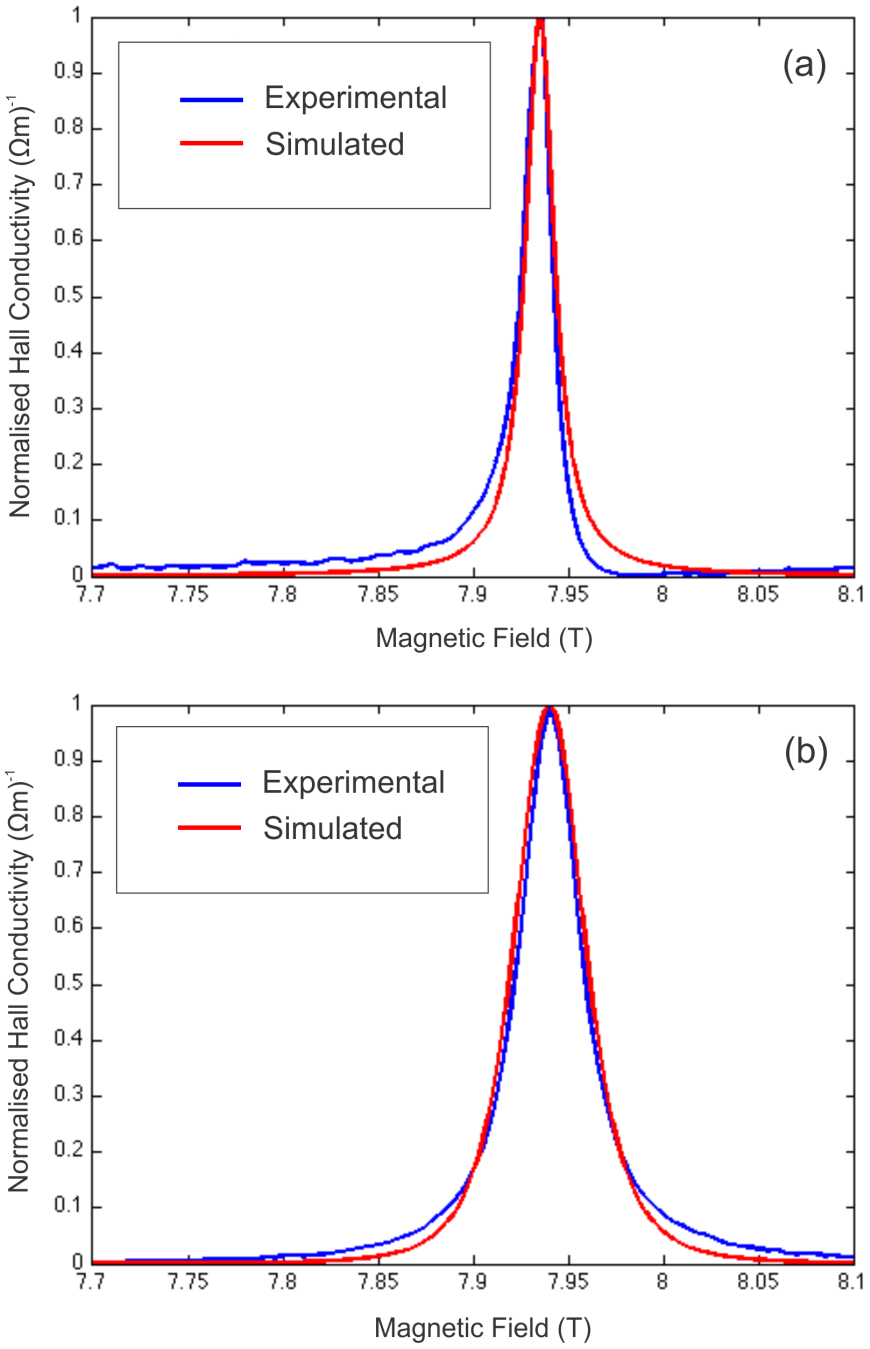

FIGURE 4.12: Plots of longitudinal and Hall conductivity of a 2DEG in a GaAs/AlGaAs (L445) heterostructure at 1.4K and 3.2 THz (L674A),along with Drude model fits. (a) Experimentally measured longitudinal conductivity (blue line) with Drude model fit (red line). (b) Experimentally measured off-diagonal conductivity (blue line) with Drude model fit (red line) for the same sample.

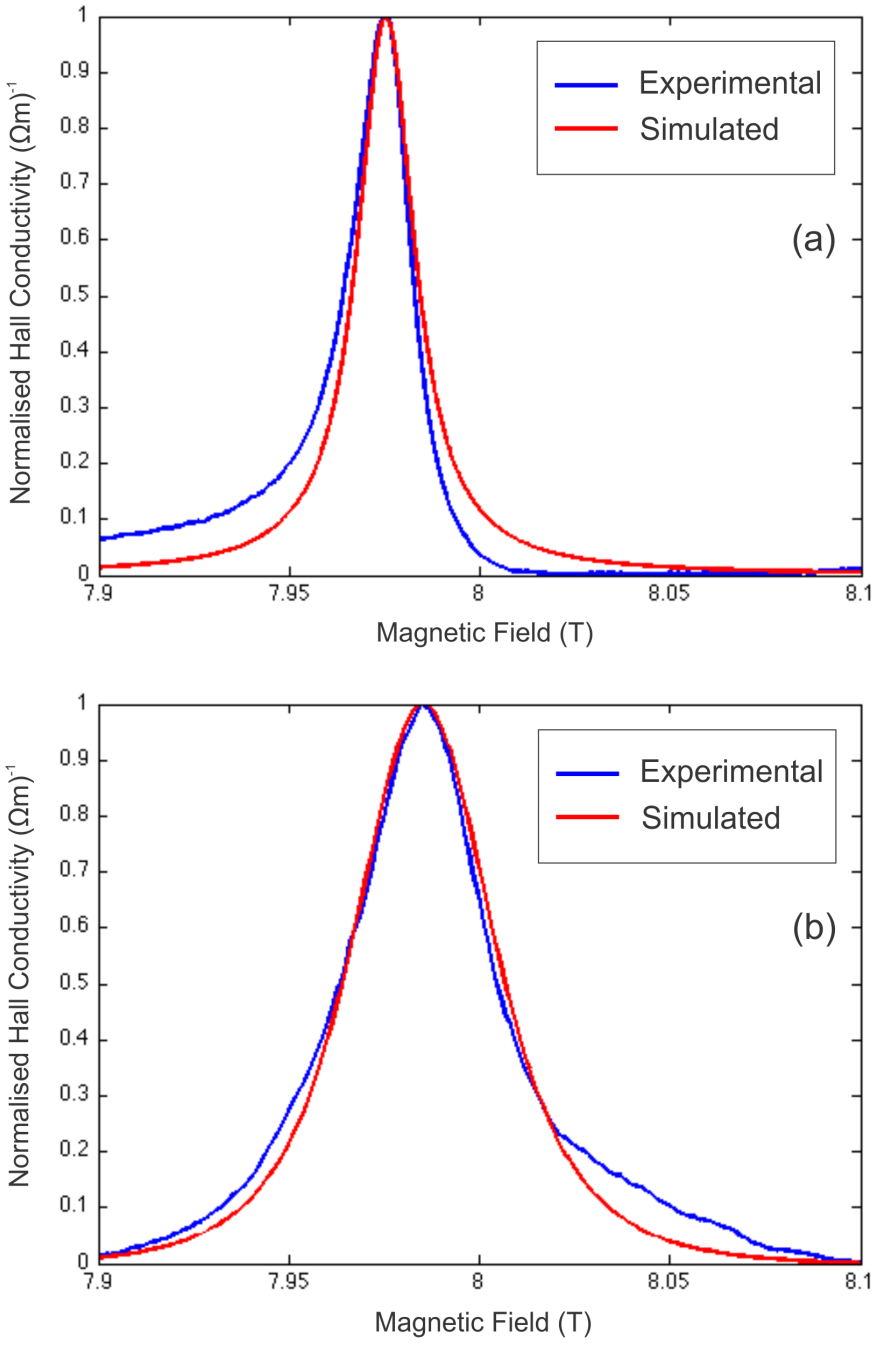

FIGURE 4.13: Longitudinal and Hall conductivity of a 2DEG in a GaAs/AlGaAs heterostructure (L498) at 1.4K and 3.2 THz (L674A), along with Drude model fits. (a) Experimentally measured diagonal (longitudinal) conductivity (blue line) with Drude model fit (red line). (b) Experimentally measured off-diagonal (Hall) conductivity (blue line) with Drude model fit (red line) for the same sample.

4.3 Free-space continuous wave microwave measurements of 2DEGs

4.3.1 Experimental Apparatus

To complement the free-space measurements of 2DEGs in GaAs/AlGaAs heterostructures undertaken with THz QCLs, and explore the electronic dynamics of electrons in a 2DEG at lower frequencies, a continuous-wave W-band (75 – 110GHz) microwave system was established. It is the first ever free-space system designed to study electron dynamics in two-dimensional electron systems. Single frequency continuous wave microwave signals were generated by up-converting a lower frequency ($\sim$12 – 19GHz) signal from a continuous microwave source. The multiplier used for this purpose provided an output frequency six times that of the input frequency. The microwave signal was emitted into free space using a horn antenna connected to the transmission module (Figure 4.14). An off-axis 2 inch parabolic mirror then collected microwave radiation. A wire-grid polariser was placed in the path of the collimated beam ensuring a linearly polarised electric field, which was focused onto the 2DEG sample inside the same cryostat (with a base temperature of 1.4K, and magnetic field range of 0 – 6 T) used in section 4.1. After transmission through the 2DEG, a 2 inch parabolic mirror collected the microwave radiation. A second wire-grid polariser was placed in the collimated beam path so that both diagonal and off-diagonal parts of conductivity could be detected, similar to the experimental design used with THz QCLs. The collimated beam was finally focused on to the centre of a W-band horn antenna connected to the wave-guide of a W-band sub-harmonic mixer that converted the signal to a much lower frequency of 700 MHz:

$$f = mf_{LO} - f_{RF} \tag{4.3}$$

f is the down-converted frequency, for this particular experimental setup it was a fixed frequency of 700 MHz, f_{LO} is the frequency of the local oscillator, m=18 for the sub-harmonic mixer used, while f_{RF} is the frequency of the received microwave signal. A cryogenically cooled low-noise amplifier was used before the signal (f) was fed into the spectrometer.

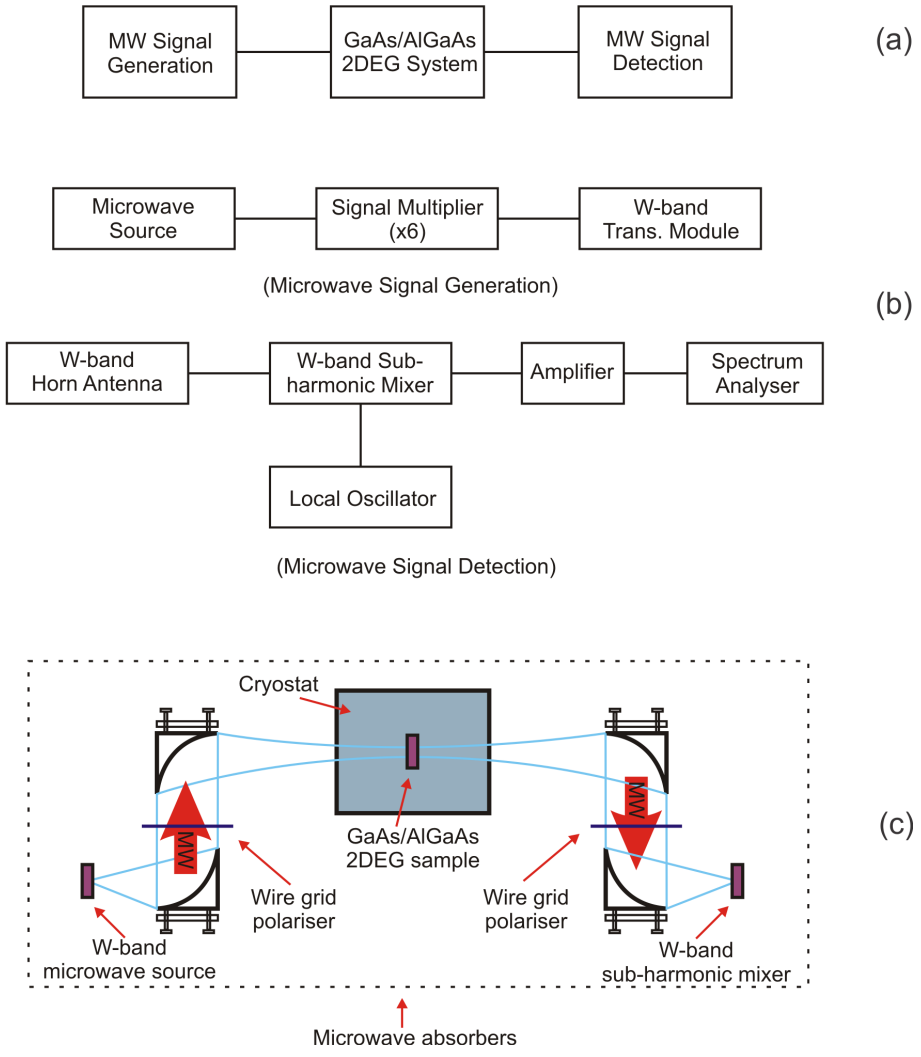

FIGURE 4.14: Free-space single frequency continuous-wave W-band microwave system for measuring the conductivity of 2DEGs in GaAs/AlGaAs heterostructures. (a) Block diagram for the free space system. (b) Microwave signal generation and detection processes. The microwave signal is generated by up-converting a continuous wave signal, while the signal is detected using a W-band sub-harmonic mixer. (c) Experimental apparatus for the free-space system. Radiation from the microwave source is focused onto the sample inside the cryostat. Wire-grid polarisers are placed before and after the cryostat to clean up the polarisation of radiation from the microwave source and suppress the unwanted component of electric field respectively.

A visible helium-neon (He-Ne) laser was used initially to verify the alignment of all optical components in the system.

4.3.2 System Stability Tests

A similar procedure to that described in section 4.1.3 was followed to verify system stability. Both the microwave source and sub-harmonic mixer used for detection purposes were positioned as far away from the superconducting magnet as possible in order to avoid any change in their performance owing to the presence of a strong magnetic field. Furthermore, microwave absorbers were placed around the system in order to avoid any unwanted reflections. DC characterisation of the 2DEG samples was carried out, as described in detail in section 4.1.3, and it was confirmed that the 2DEG carrier concentration did not alter on exposure to microwave radiation The windows of the cryostat were covered with black plastic sheets to ensure that no change in carrier concentration occurred during experiments through excitation by external light.

4.3.3 Measurement Technique

The same 2DEG samples, that were used in the free-space QCL based system (Table 4.2), were used for microwave transmission measurements, with DC magneto-conductivity of large square samples being evaluated using the Van der Pauw technique. Once again, owing to the inability to record phase information in this experimental realisation, only the real part of conductivity could be evaluated. The diagonal component of conductivity was measured by placing the wire-grid polariser, orthogonally aligned to the electric field vector of the incoming microwave radiation, in the beam path. The off-diagonal component of conductivity requires a much higher SNR as the signal is very small and close to the background noise floor at low magnetic field values. Owing to the free-space experimental configuration used, the off-diagonal part of conductivity could not be evaluated since the signal level was too low. This arises because the sub-harmonic mixer used for detection sampled the eighteenth harmonic and high signal powers are needed for efficient conversion. So this particular detection scheme did not have the ability to measure the off-diagonal part of conductivity as the conversion loss of system was too high for small Hall components to be detected. The detection sensitivity of free-space system can be improved by using a helium cooled bolometer instead of the sub-harmonic mixer. Drude model was again employed to simulate the conductivity over the range of frequencies using Matlab and fit to the experimental data.

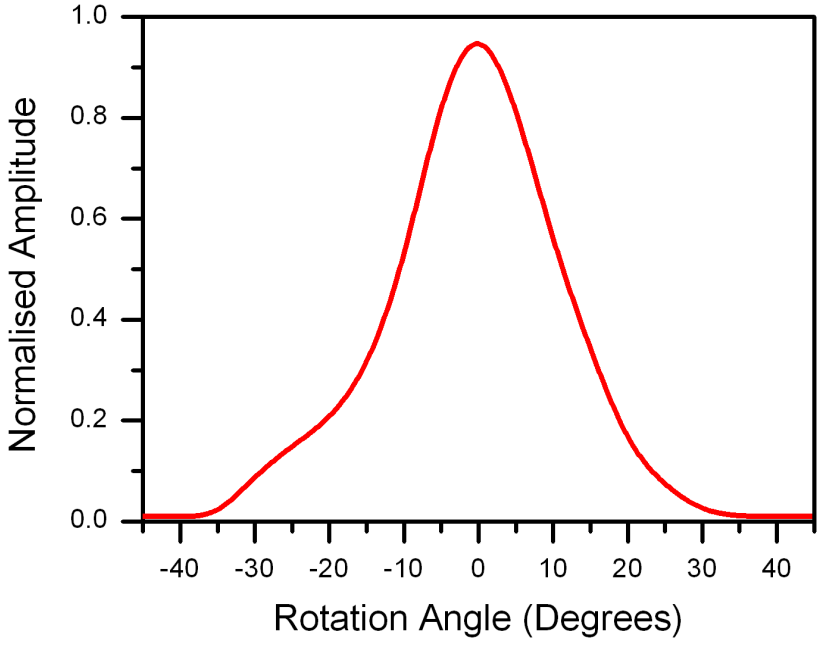

FIGURE 4.15: Test of the polarisation of radiation emitted from the microwave source. The zero-degree position corresponds to the wire-grid polariser being orthogonal to the electric field to the incoming radiation. The microwave signal was then recorded as the angular position of the wire-grid polariser was changed.

4.3.4 Results and Analysis

Typical experimental results are presented in Figures 4.15 – 4.20. The presence of a wire-grid polariser between the first and second parabolic mirrors is included to ensure a linearly polarised electric field is incident on the 2DEG sample inside the cryostat. To verify the polarisation of the microwave source, the single-frequency continuous-wave signal from the narrowband microwave source was recorded for different angular orientations of the wire-grid polariser, without the 2DEG sample or second wire-grid polariser present in the experiment apparatus (Figure 4.15). As can be seen, the signal amplitude drops sharply as the wire-grid polariser is rotated. This clearly indicates the presence of a linearly polarised electric field from the microwave source.

Figures 4.16 and 4.17 show the measured results with 2DEG samples inside the cryostat, and the second wire-grid polariser also present in the system. Transmission through 2DEG samples was recorded at different frequencies, which were set by tuning the reference microwave source. Electron effective masses of $0.071 * m_0$ and $0.072 * m_0$ were used to fit f vs B to the experimental data for L445 and L498 respectively (Figure 4.18), these values are within 5 percent of what has been measured using time domain system in chapter 5. Plots of the diagonal conductivity at various different frequencies, inside the W-band i.e. 75 to 110 GHz, are then shown in figures 4.19 and 4.20 along with Drude model fits using equations 4.1.

Unlike the simulated Drude model conductivity, which is Lorentzian in shape, the experimentally measured conductivity is asymmetric. This particular behaviour was also observed in the data recorded using a QCL-based free-space system.

To complement the frequency-domain studies in this chapter, time-domain spectroscopy was also undertaken (Chapter 5). No asymmetry was seen in the CR feature in this case, but as discussed in Chapter 5, this can be attributed to the data analysis technique used.

To understand the asymmetry observed in frequency-domain systems, further systematic measurements would be required, including changing the measurement temperature, carrier concentration or mobility in a systematic manner.

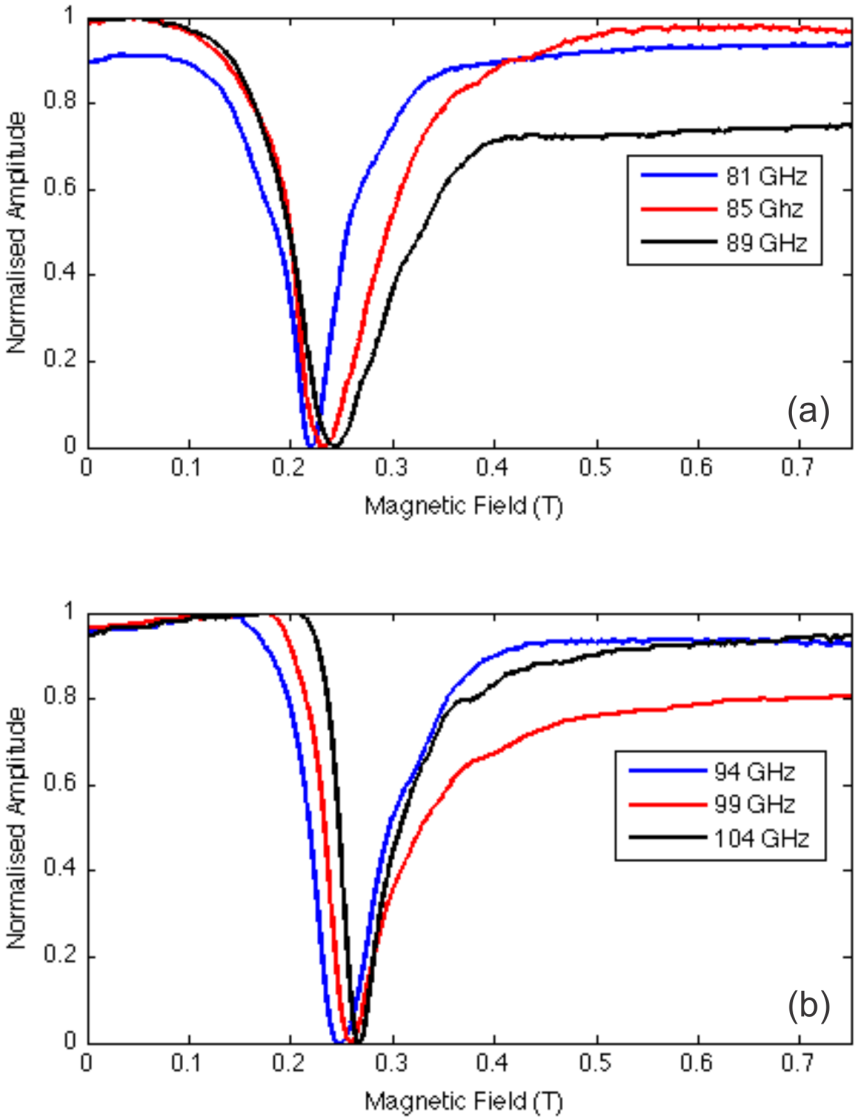

FIGURE 4.16: Transmission data for L445 (Dark) at different frequencies obtained using a W-band free space microwave system. The 2DEG sample was present in the beam path inside the cryostat at a base temperature of 1.4K. Electron cyclotron motion leads to absorption at specific values of magnetic field for each frequency. (a) Transmission data for L445 (Dark) at 81, 85 and 89 GHz respectively. (b) Transmission data for L445 (Dark) at 94, 99 and 104 GHz respectively.

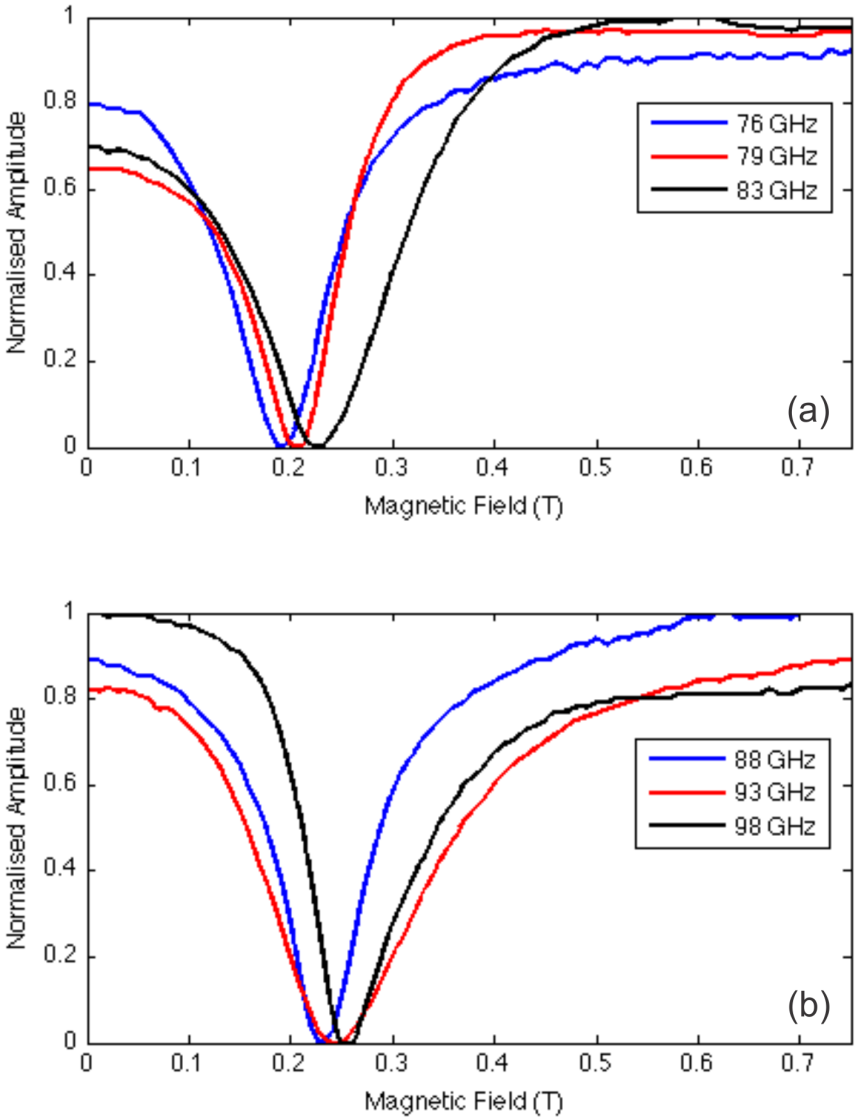

FIGURE 4.17: Transmission data for L498 (Dark) at different frequencies obtained using a W-band free space microwave system. The 2DEG sample was present in the beam path inside the cryostat at a base temperature of 1.4K. The cyclotron resonance leads to absorption at specific values of magnetic field for each individual frequency. (a) Transmission data for L498 (Dark) at 76, 79 and 83 GHz respectively. (b) Transmission data for L498 (Dark) at 88, 93 and 98 GHz respectively.

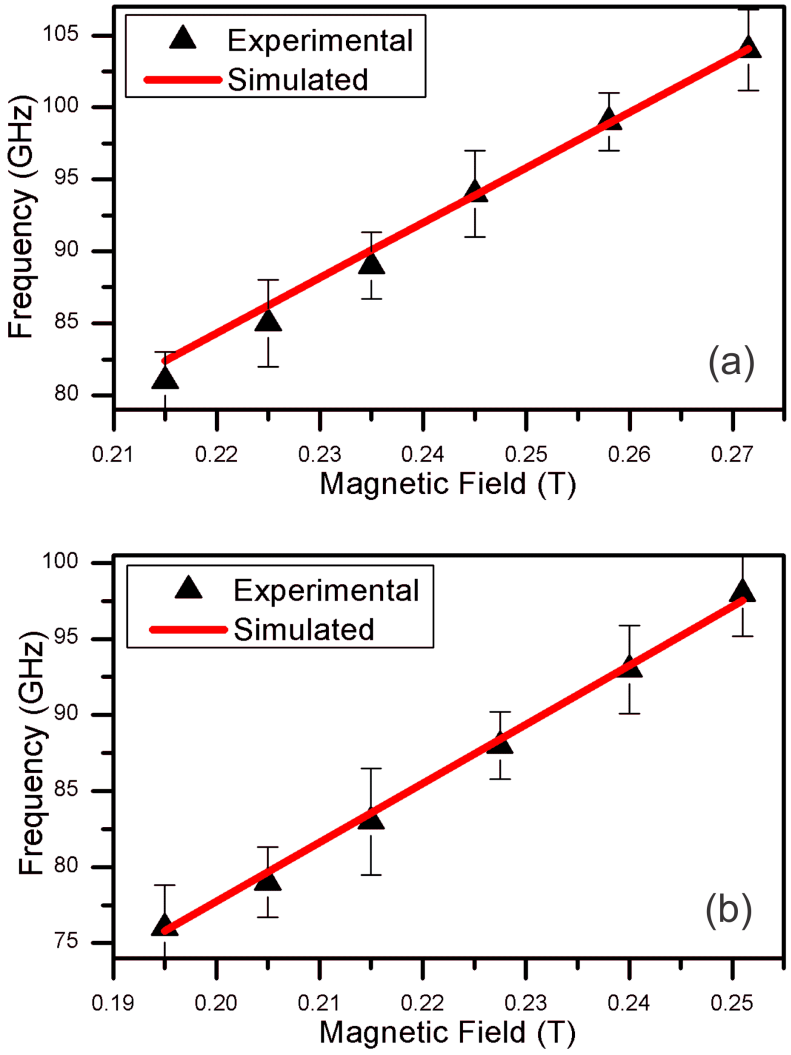

FIGURE 4.18: f vs B plot to evaluate the effective mass from the data presented in Figures 4.16 and 4.17. The effective mass $A * m_0$ can be extracted by fitting to the experimental data. (a) Experimental data for L445 (Dark) at six different frequencies of 81, 85, 89, 94, 99 and 104 GHz respectively (black triangles) with an effective mass $0.071 \pm 0.003 * m_0$ (red line). (b) Experimental data for L498 (Dark) at six different frequencies of 76, 79, 83, 88, 93 and 98 GHz respectively (black triangles) with an effective mass $0.072 \pm 0.003 * m_0$ (red line).

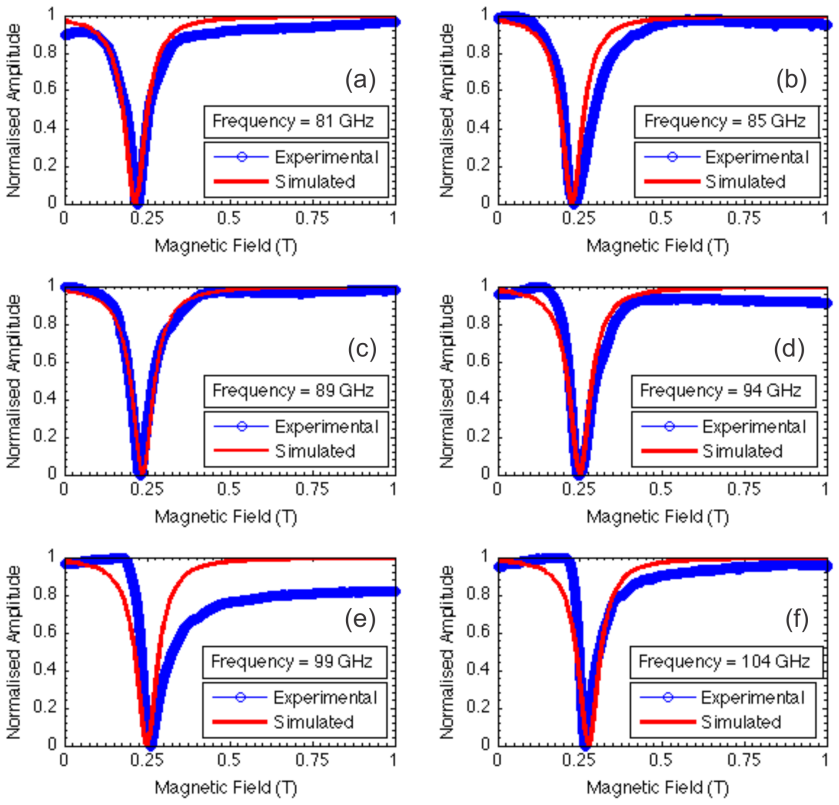

FIGURE 4.19: Transmission data for L445 (*Dark*) together with Drude model fits. A change in the width of the cyclotron resonance can be observed from these plots, leading to an overall asymmetric CR feature. Transmission data with Drude model fits are shown at (*a*) 81 GHz, (*b*) 85 GHz, (*c*) 89 GHz, (*d*) 94 GHz, (*e*) 99 GHz and (*f*) 104 GHz.

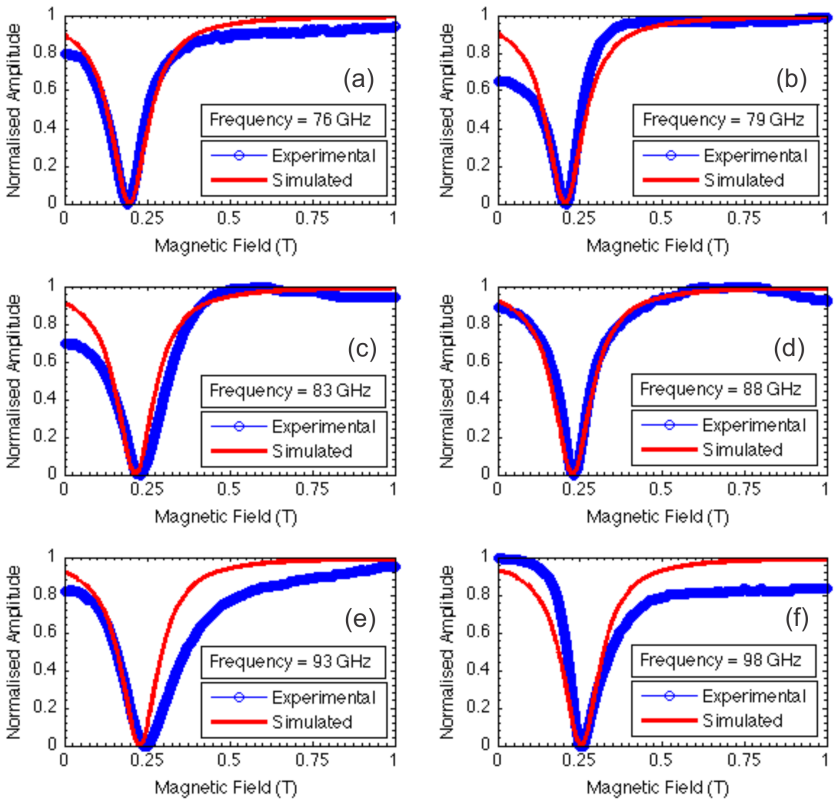

FIGURE 4.20: Transmission data for L498 (*Dark*) along with Drude model fits. A change in the width of the cyclotron resonance can be observed from these plots, leading to an overall asymmetric CR feature. Transmission data with Drude model fits are shown at (*a*) 76 GHz, (*b*) 79 GHz, (*c*) 83 GHz, (*d*) 88 GHz, (*e*) 93 GHz and (*f*) 98 GHz.

4.4 Summary

Free-space transmission measurements of 2DEGs in GaAs/AlGaAs heterostructures have been undertaken using microwave- and QCL-based systems. The real part of diagonal and off-diagonal conductivity of the 2DEG samples was evaluated. Simulations of conductivity based on Drude model equations were carried out for the range of frequencies used in these experiments, and good agreement was generally obtained with the simulated results. An effective mass of $0.068 * m_0$ was measured using the QCL-based free-space pulsed system, whilst slightly higher effective masses of $0.071 \pm 0.003 * m_0$ and $0.072 \pm 0.002 * m_0$ were obtained using the free-space single-frequency continuous-wave microwave system, for two different 2DEG samples. Asymmetric behaviour in the CR lineshape was observed in the frequency-domain studies, unlike for time-domain spectroscopy data where the CR has a perfect Lorentzian shape. A further investigation of this phenomenon in the frequency-domain is needed.

Chapter 5

Terahertz time-domain magneto-spectroscopy of two-dimensional electron gas

5.1 Introduction

The studies of the dynamical conductivity of two-dimensional electron gas (2DEG) in GaAs/AlGaAs heterostructures has been reported using both time and frequency domain techniques in this thesis. Terahertz time-domain spectroscopy (THz-TDS) has inherent advantages over other techniques since it allows direct measurement of both amplitude and phase, allowing a full evaluation of the complex conductivity tensor of 2DEG in GaAs/AlGaAs. Measurement of cyclotron resonance (CR) in a high-mobility GaAs/AlGaAs 2DEG using the technique of terahertz time-domain spectroscopy combined with magnetic fields has been reported (up to 0.8 THz and 1.4T) before [21–27]. In this chapter, I will discuss the construction of a free-space time-domain spectroscopy system to study the magneto-conductivity of 2DEG samples. Experimental data has been presented for both diagonal and off-diagonal part of conductivity. The results (up to 1.5 THz and 6T) have already been presented at the 20th international conference on Electronic properties of two-dimensional electron system 2011, Florida USA [94]. Detailed simulations have also been presented to explain the effects of sudden truncation of the THz time domain pulse.

5.2 Experimental apparatus

Figure 5.1 shows the experimental setup for the free space THz TD magneto-spectroscopy system used for these measurements. The beam from a pulsed Ti:sapphire laser is split into pump and probe beams using dielectric beam-splitter. The pump beam illuminates an electrically biased semi-insulating GaAs photo-conductive antenna, generating THz pulses. Also shown is the quarter-wave plate, Wollaston prism and balanced photodiodes for electro-optic detection. A 0.9 x 0.9 cm square sample has been used for these free space transmission measurements with four electrodes at the corners for DC characterization. The sample was mounted on a probe stick inside the cryostat at the base temperature of 1.4K with an effective magnetic field range of 0 to 6T. For these measurements the free-space system bandwidth was 1.5 THz; the cut-off frequency being 60 percent of the peak Fourier amplitude. A wire grid polariser enabled measurement of both components of the propagating THz electric field.

5.3 Measurement technique

Fourier transforms of the time domain data were used to extract the amplitude and phase information. The zero padding technique, where length of time domain signal is increased by adding a stream of zeros to the time domain data, was employed to enhance the frequency resolution of the experimental data, as the original window size in the time domain resulted in a frequency resolution of 50 GHz. For this set of measurements the stream of zero was added to the time domain THz time domain pulse before the main peak. After the zero padding the final length of the time domain THz pulse became five times that of the original one. It was observed that this particular data analysis technique only does the data smoothing, with the system's inherent frequency resolution remaining the same. It was also observed that background noise in the system also remains the same hence no observable change in the system bandwidth as well.

At B = 0T when there is no Hall component present in the transmission signal, the wire grid polariser was placed perpendicular to the beam path with wire grid perpendicular to the electric field vector. In order to measure the Hall component only, the wire grid polariser was rotated through 90^0, hence making wire grid

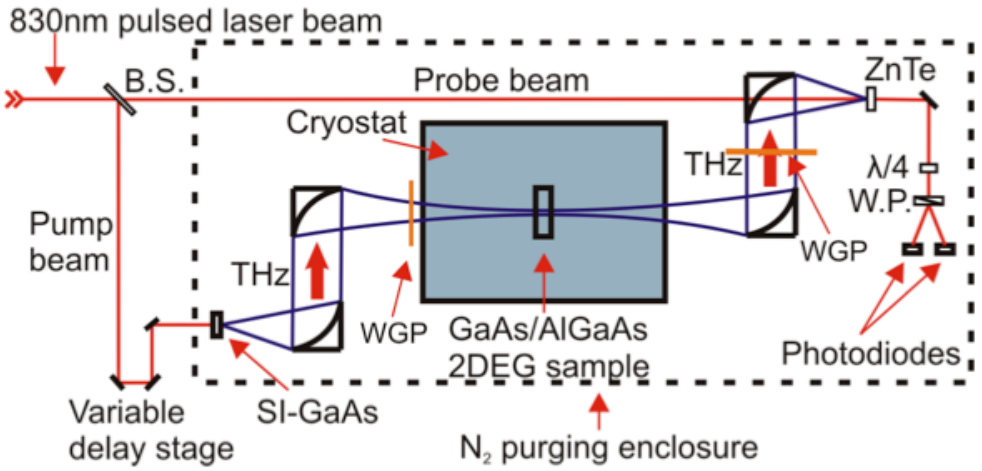

FIGURE 5.1: Schematic of THz TD magnetospectroscopy system used for dynamical conductivity measurements of a 2DEG in a GaAs/AlGaAs heterostructure. The first WGP ensures a linearly polarised radiation directed towards the sample inside the cryostat. Second WGP was physically rotated through 90 degrees in order to record both diagonal and off-diagonal parts of 2DEG magneto conductivity. Here B.S. is the beam splitter and WGP is the wire grid polariser.

parallel to electric field vector at B = 0T. The magneto conductivity of 2DEG sample was evaluated by using the transmission data for 2DEG and a bulk GaAs substrate without any conductive layer. The transmission data for the bulk GaAs substrate was used as reference.

5.4 Results and analysis

THz TDS transmission through a 2DEG for both diagonal and off-diagonal components under dark and light conditions is shown in figures 5.2 and 5.3. Some extra features, parallel to the cyclotron resonance, have been observed in transmission data for both diagonal and off-diagonal components under dark and light conditions. Initially it was assumed that these extra features were a manifestation of the magneto plasmon modes in the 2DEG sample (Figure 5.4), or that they represented multiple harmonics of the cyclotron resonance (Figure 5.5). In order to investigate the origin of these extra features, transmission through different 2DEG samples was recorded for a range of magnetic fields. Also, simulations were carried out to investigate the origin of these new features (See sections 5.4.1 and 5.4.2). Many samples, with different carrier concentration and electron mobility, were used for THz TDS transmission measurements (Table 2.1). It can also be

observed in the experimental data that the width of cyclotron resonance seems to be changing at lowerr magnetic fields. This can be attributed to the signal to noise ratio of the free space system deteriorating at the lower limit of the system bandwidth that affects the ability of experimental system to resolve the correct width of the cyclotron resonance. Similar is the case for the higher magnetic fields. There are also some vertical bands visible in the transmission data (Figure 5.3). These sudden fluctuations in amplitude can be attributed to sudden changes in the noise floor of the THz TDS system. Since there was a manual needle value on the 1.4K cryostat to control the flow of liquid helium inside the sample chamber, so at times there were fluctuations in the temperature inside the sample chamber and transmission syatem was sensitive enough to pick up those changes.

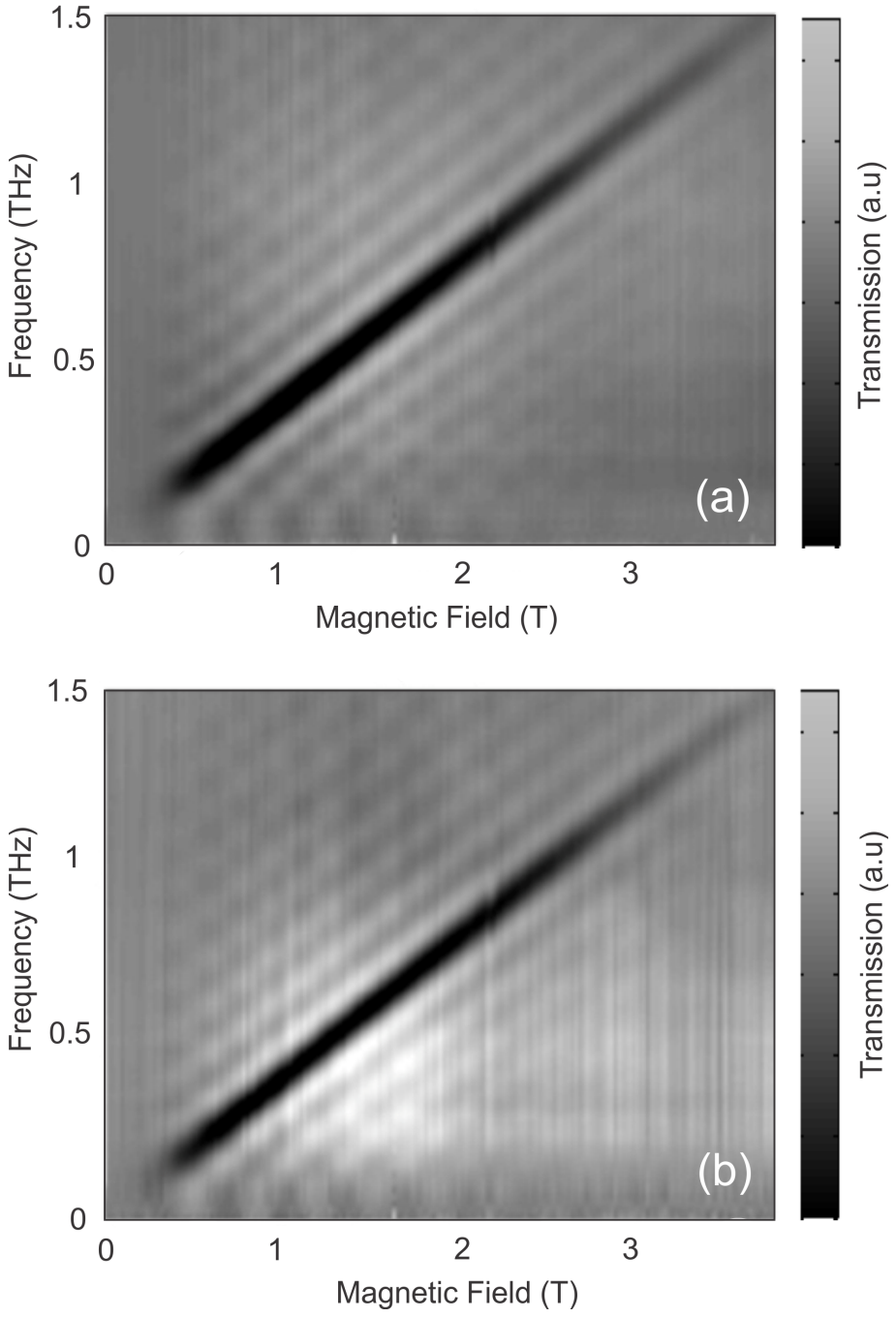

FIGURE 5.2: Experimental data for longitudinal part of conductivity under (a) dark and (b) light conditions. Extra features parallel to the cyclotron resonance can be observed in both situations. The data has been shown only up to 3.5T as the system bandwidth is limited to 1.5 THz and there are no observable features beyond 3.75 T.

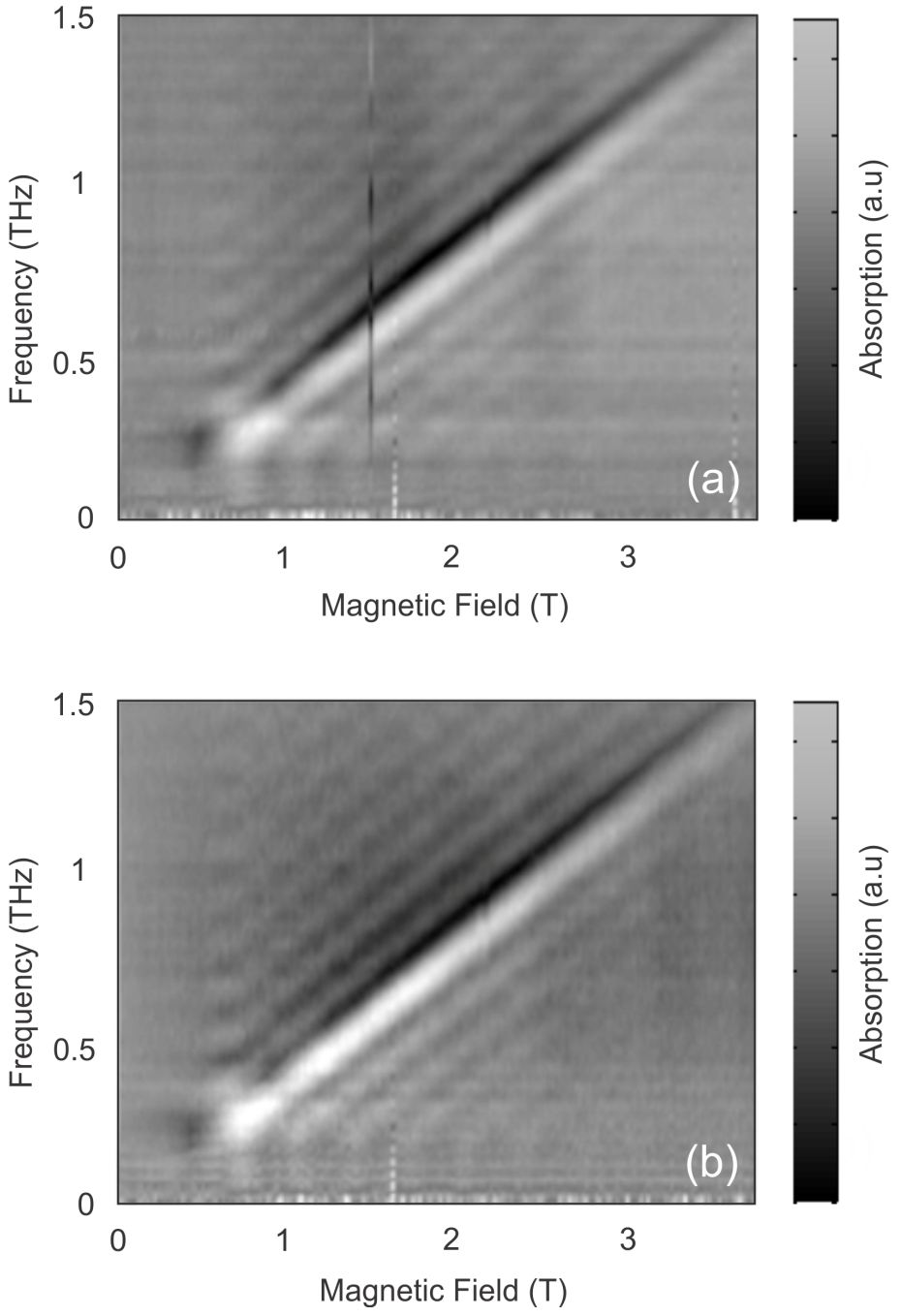

FIGURE 5.3: Experimental data for off-diagonal (Hall) part of conductivity under (a) dark and (b) light conditions. Again extra features parallel to the cyclotron resonance can be observed in both situations. As the carrier concentration of 2DEG sample is changed these features become prominent. The apparent change in the width of cyclotron resonance at low magnetic fields can be attributed to the signal to noise ratio of the system deteriorating at the lower limit of the system bandwidth. Also the presence of vertical bands in both figures can be attributed to sudden changes in the noise floor of the system.

5.4.1 Simulations for magnetoplasmon resonance

In order to determine whether the extra features in the experimental data are magnetoplasmons, simulations were performed for a range of sample sizes and 2DEG carrier concentrations (Figure 5.4). A plasmon mode in a 2DEG can be thought of as a coherent oscillation of the electrons constrained by the boundaries of the 2DEG sample. The coupling of the two-dimensional plasmon and the cyclotron resonance forms the magnetoplasmon resonance. When a magnetic field is applied perpendicular to the surface of a 2DEG, the cyclotron resonance and plasmon in 2DES couple yielding a magnetoplasmon mode. Mathematically it can be represented by the following equation;

$$\omega = \sqrt{\omega_p^2 \ + \ \omega_c^2} \tag{5.1}$$

where ω_c is the cyclotron resonance frequency; given by $\omega_c = eB/m^*$, e is the electron charge, B is the magnetic field perpendicular to the surface of the 2DEG and m^* is the electron effective mass. The symbol ω_p is the two-dimensional plasmon frequency; given by $\omega_p = \sqrt{e^2 n_s q/2\epsilon_0 \epsilon m^*}$, where n_s is the carrier concentration of 2DEG, $\epsilon_0\epsilon$ is the dielectric constant of the substrate used and $q = \pi/w$ is the wave vector of the two-dimensional plasmon (w is the width of the 2DEG sample).

Figure 5.4 shows simulated plasmon modes along with cyclotron resonance for a range of sample sizes. As the sample size is reduced, the spacing between individual magneto plasmon modes increases. In wider samples the plasmons are not very sharp, and different modes have different strengths leading to a situation where weaker modes can be masked by the stronger ones. The simulated data did not have any agreement with the experimental results, so it was concluded that the observed features were not magneto plasmons. Figure 5.5 shows simulated and experimental data considering multiple cyclotron resonances in the sample at the same time assuming that the electron are getting scattered to multiple Landau levels i.e. from n to n+1, n+2, n+3 etc. Again, as far as the extra features are concerned, the experimental results do not agree with the simulated data. So based on this set of simulations, the phenomenon of multiple cyclotron resonances was ruled out as well.

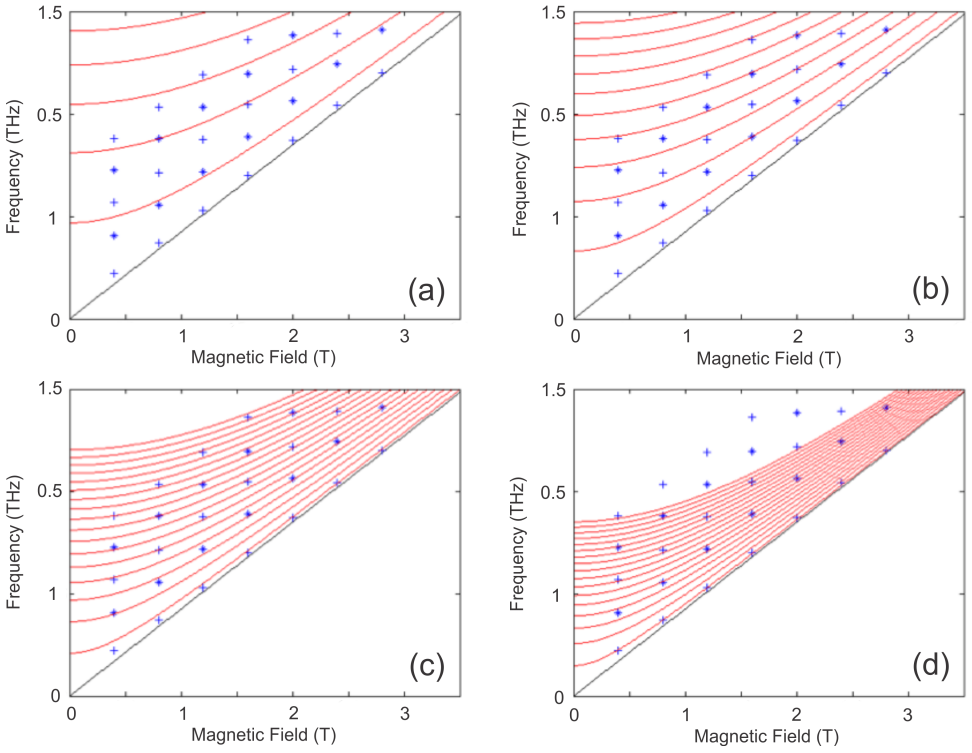

FIGURE 5.4: Simulations for magneto plasmons in a 2DEG for different widths of the sample used. Figures (a) to (d) show the simulated magneto plasmon modes and cyclotron resonance along with the experimental data for sample sizes of 10, 20, 50 and 100 μm. It can be observed clearly that the spacing between modes decreases as the sample width is increased. For the sample size used in measurements (i.e. 9 mm), the magneto plasmon modes merged completely into the cyclotron resonance.

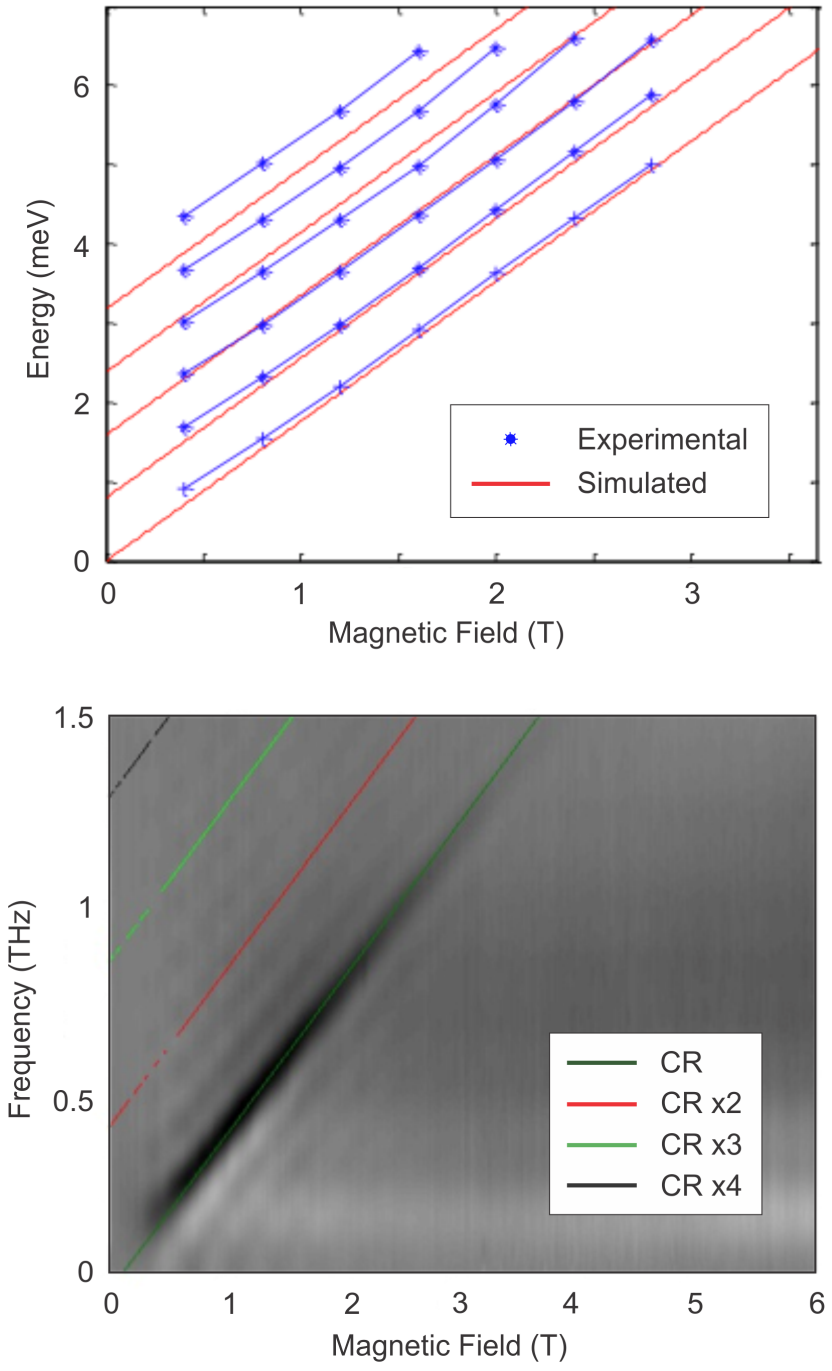

FIGURE 5.5: Simulated data along with experimental results in order to check the presence of multiple cyclotron resonances in the 2DEG. Figure (a) shows simulated data (red lines) with equal energy gap among all modes. The experimental data does not carry a good agreement as the spacing among all modes is not uniform. Figure (b) shows experimental data with overlaid multiple cyclotron resonances. Once again, the experimental data does not agree well with the theory, as there are extra lines in the experimental data in between any two cyclotron resonance features.

5.4.2 Simulations to find out the origin of extra oscillations

In the time domain the difference of signals at finite and zero magnetic fields leads to decaying periodic oscillatory pulse, so a THz TDS system evaluating a 2DEG at cyrogenic temperatures under strong magnetic fields can be considered as a damped oscillator. Matlab was used to evaluate the effect of the length of time domain THz pulses and its relationship to the extra oscillatory features observed in the experimental data. A range of different lengths for the time domain pulse were used in the simulations (following the main peak), in which the periodic cyclotron oscillations in the time domain were extrapolated (using curve fitting) to fit any desired time window. It has been observed during simulations that the truncation of a periodic time signal leads to oscillatory features in the frequency spectrum (either side of the main peak) when a Fourier transform is taken (Figure 5.6). Since this is also a possible cause of the small oscillations surrounding the cyclotron resonance peak in this work, further simulations were done to check how the oscillations depend on truncation of the time-domain signal (Figures 5.8). The results showed that the position and amplitude of the small oscillations depend directly on the length of the time domain signal. The oscillatory features became more pronounced as the size of the time domain pulse was reduced.

Simulations were also performed to study the effect of magnetic field on these oscillations (Figures 5.7). The period of cyclotron oscillations in the time domain pulse reduces as magnetic field is increased i.e. cyclotron resonance moves to higher frequencies. This effect was replicated by just changing the frequency of the simulated oscillatory time signal. Simulated results showed that spacing between extra features in the frequency domain data did not change as the magnetic field was changed. Hence it was concluded that the small oscillations were a direct consequence of truncating the time-domain signal to avoid incorporating reflection peaks (Figures 5.6, 5.7).

The same technique was applied to analyse the experimental data in order to confirm the predicted behaviour of the new features. Figures 5.8 and 5.9 show that spacing between small oscillations does not change as the magnetic field is changed. Also the amplitude and position of the oscillations change when the time domain trace is truncated at different lengths of time, hence a direct confirmation of what was predicted by simulations.

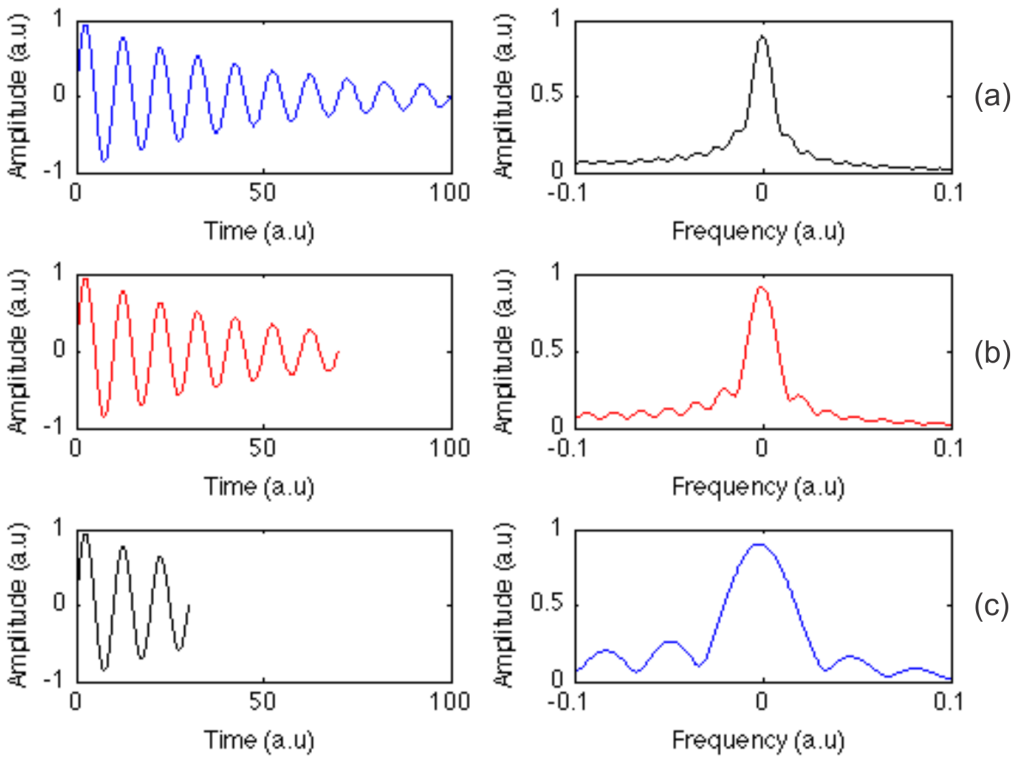

FIGURE 5.6: Simulated data to demonstrate the effect of window size of the time domain pulse. (a, b and c) The damped oscillations displayed in the figures on the left represent the time-domain signal at a finite magnetic field minus the zero-field reference waveform. Any truncation of the time domain signal results in oscillatory features in the Fourier transformed data (figures on the right). As the window size is reduced in time domain, the spacing between the small oscillations increases, accompanied by a change in amplitude and position.

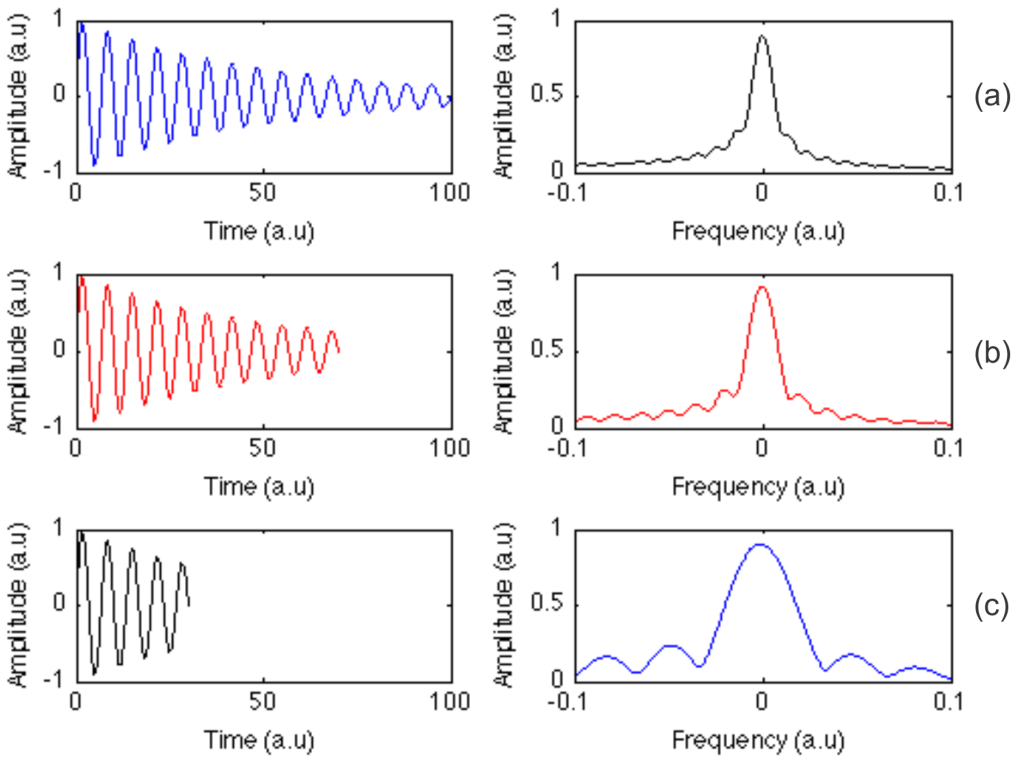

FIGURE 5.7: Simulated data to demonstrate the effect of change in magnetic field for the same window length as that in figure 5.6. Since cyclotron resonance shifts to higher frequency as the magnetic field is increased, the frequency of the simulated cyclotron oscillations was increased twofold, in order to replicate the effect of magnetic field on the extra oscillations in the data. It was observed by comparing the data in figures 5.6 and 5.7 that the position of extra oscillations does not change as the magnetic field is changed.

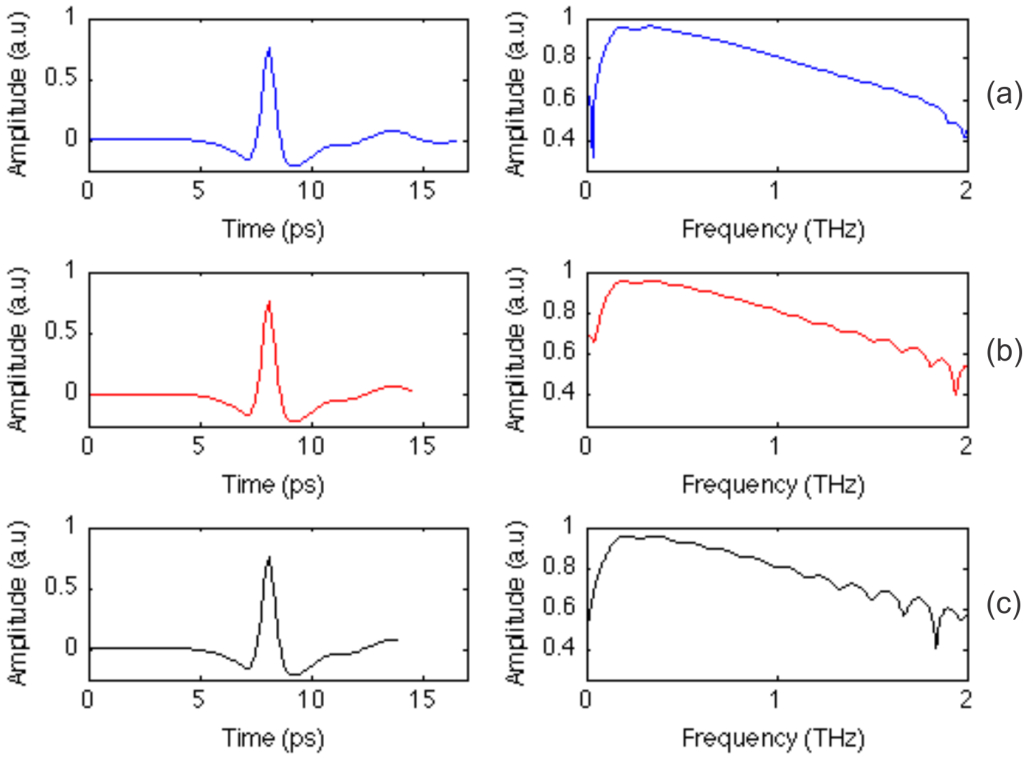

FIGURE 5.8: Effect of the window size of the time domain pulse (experimental data). (a, b and c) Figures show the time domain pulse at 1.32 T being truncated at different points in time. As predicted by simulations, extra oscillations appear in the Fourier transformed data shown on the right. A change in the window size leads to a change in the width and amplitude of the small oscillations in the Fourier transformed data.

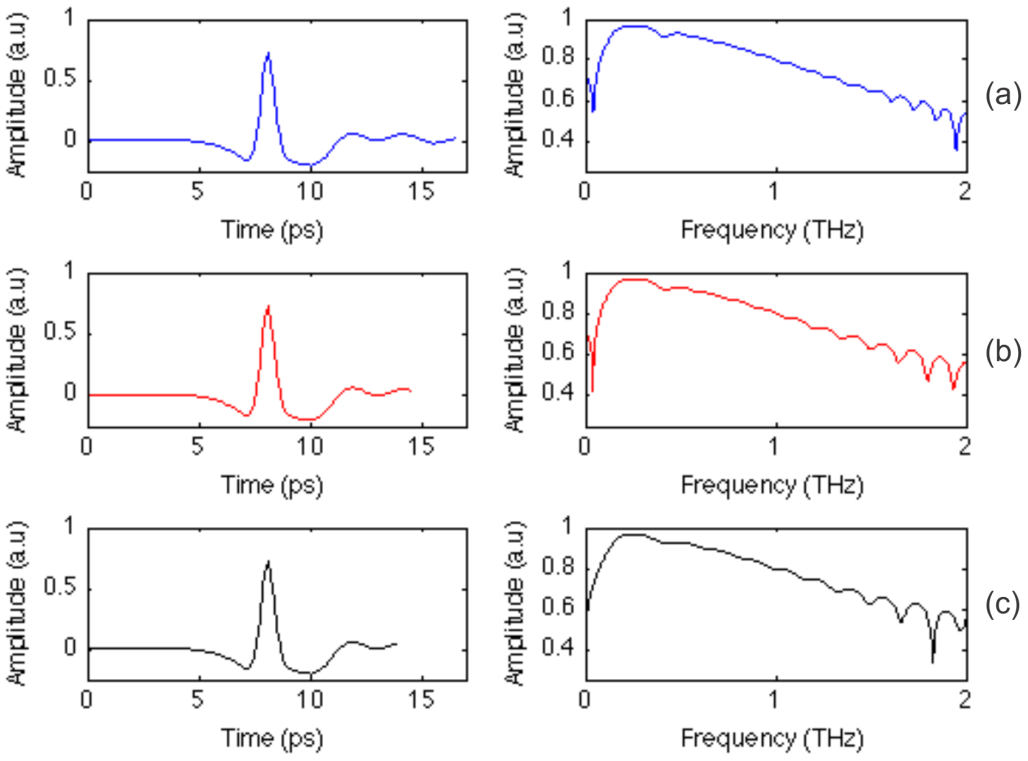

FIGURE 5.9: Effect of the window size of the time domain pulse (experimental data) as the magnetic field is changed. (a, b and c) Figures show the time domain pulse at 2T being truncated at different points in time. As predicted by simulations, it can be observed by comparing figures 5.8 and 5.9 that the position of extra oscillations does not change as the magnetic field is changed.

5.4.3 Modified data analysis technique

Since simulations done in Matlab showed that the extra oscillations in THz TDS transmission data were a system artefact, a different data analysis technique was devised to remove extra oscillations (Figure 5.10). As mentioned earlier that in the time domain the difference of signals at finite and zero magnetic fields leads to decaying periodic oscillatory pulse, so in this new technique, decaying sinusoids were fitted to the time domain data and appending the simulated data to it increased the window size of the time domain pulse. Taking a time domain pulse at a finite magnetic field and subtracting the zero-field reference waveform results in a decaying sinusoid, waveform representing cyclotron resonance in the time domain. It is this decaying sinusoid that was extrapolated using curve fitting. Instead of employing the zero padding technique to enhance the frequency resolution of the system, the window size of the time domain pulse was extended by curve fitting technique. The Fourier transformed data from the extended time domain pulse either had no extra oscillations or supressed ones depending on the length of extended time domain pulse as predicted by simulations in Matlab (Figure 5.6 – 5.9). The real part of longitudinal conductivity was evaluated using the Fourier transformed data, in order to demonstrate that the new data analysis technique helped to remove the extra oscillations. Simulated data for the real part of longitudinal conductivity, based on the Drude model, was also fitted to the experimental data (Figure 5.11) and there is a good agreement between the experimental and simulated conductivities. All the simulations and fitting were done using Matlab.

Despite the fact that the new technique helped to remove extra oscillations from the experimental data, there are few inherent limitations associated with this particular data analysis technique. Firstly this technique cannot be used to evaluate the complex part of conductivity (Appendix A). It involves a process that starts with taking the difference between the time domain pulses at a finite and zero magnetic fields. But this cannot be the case in order to evaluate the complex part. One will have to first fit the data to the decaying sinusoid and extend the time domain window size followed by converting the decaying sinusoid into a normal time domain THz TDS pulse. All this involves too much fitting and interpolation that it ends up in a situation where most of the data is no longer real. Secondly, it is a very monotonous process, as one has to verify the fitting to the time domain data at all magnetic fields manually as any minor fluctuation in temperature inside the sample chamber will lead to a sudden change in the system noise floor

that will consequently result into a measureable change in the transmission data (Figure 5.3).

Figures 5.12 to 5.15 show the experimental data for the real part of longitudinal and Hall conductivities both under dark and light conditions, along with Drude model fits. Application of the new data analysis technique helped to suppress the extra oscillations. The extra oscillations can be completely removed, although the original experimental data then forms only a small fraction of the total signal undergoing the Fourier transform. In figures 5.14 and 5.15, almost ten times as much fitting and extrapolation has been applied in comparison to data shown in figures 5.12 and 5.13. This means that the time domain pulse length of the data shown in figures 5.14 and 5.15 is ten times that of shown in figures 5.12 and 5.13. The difference is obvious in the latter case, where very small features can also be observed in the experimental data. It is also noticeable that the effective system bandwidth has improved (Figures 5.14 and 5.15). This particular fitting techniques results into a much lower system noise floor in the Fourier transformed data hence a net increase into the effective system bandwidth.

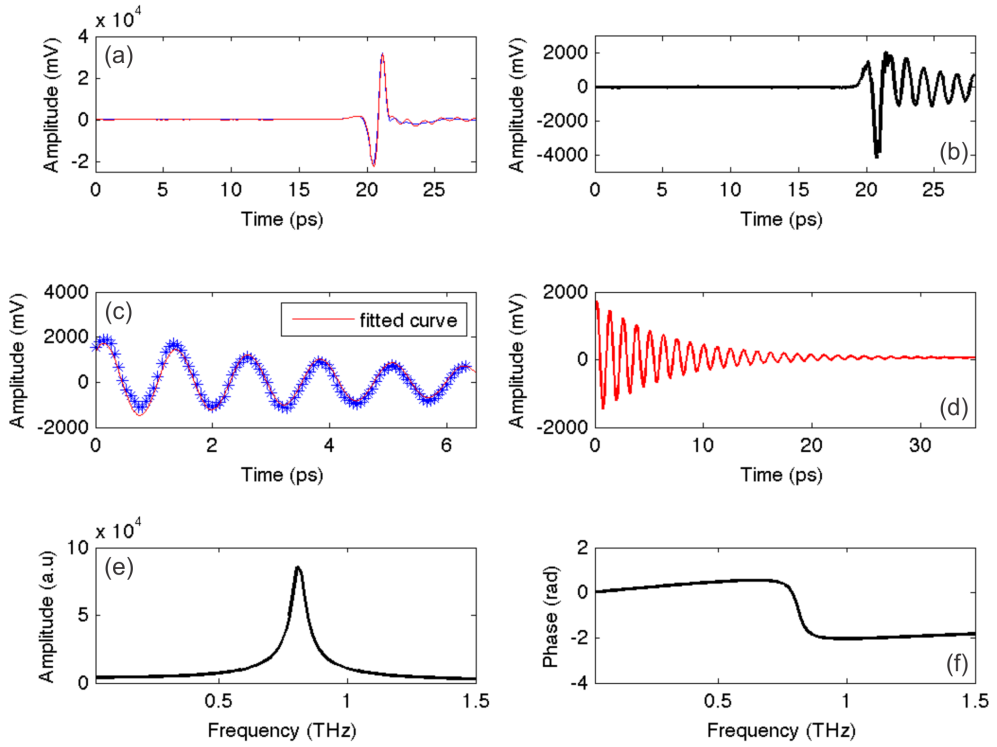

FIGURE 5.10: Modified data analysis technique for removing the extra oscillations from the Fourier transformed data. (a) Time domain traces at zero and finite magnetic field i.e. B=2T, (b) difference of the time domain pulses, (c) experimental data fitted to a decaying sinusoid, (d) simulated data appended to the experimental data in order to increase time window length and (e and f) Fourier transformed data after fitting.

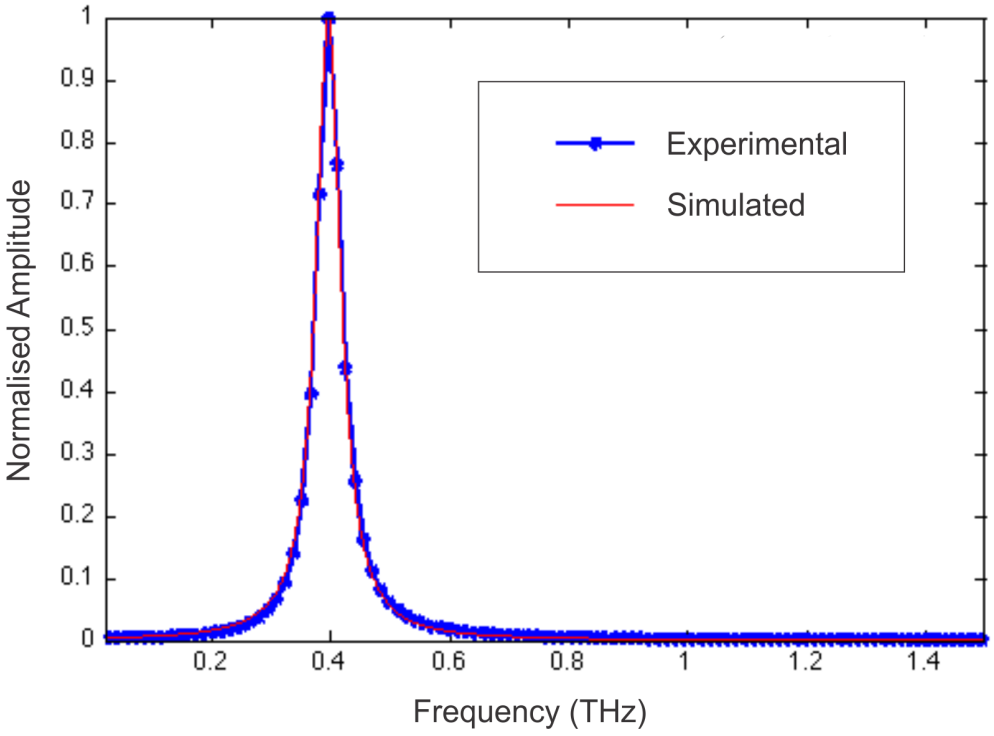

FIGURE 5.11: Real part of longitudinal conductivity along with simulated one based on Drude model using Matlab, to demonstrate the new data analysis technique. The experimental data carries a good agreement with that predicted by theory.

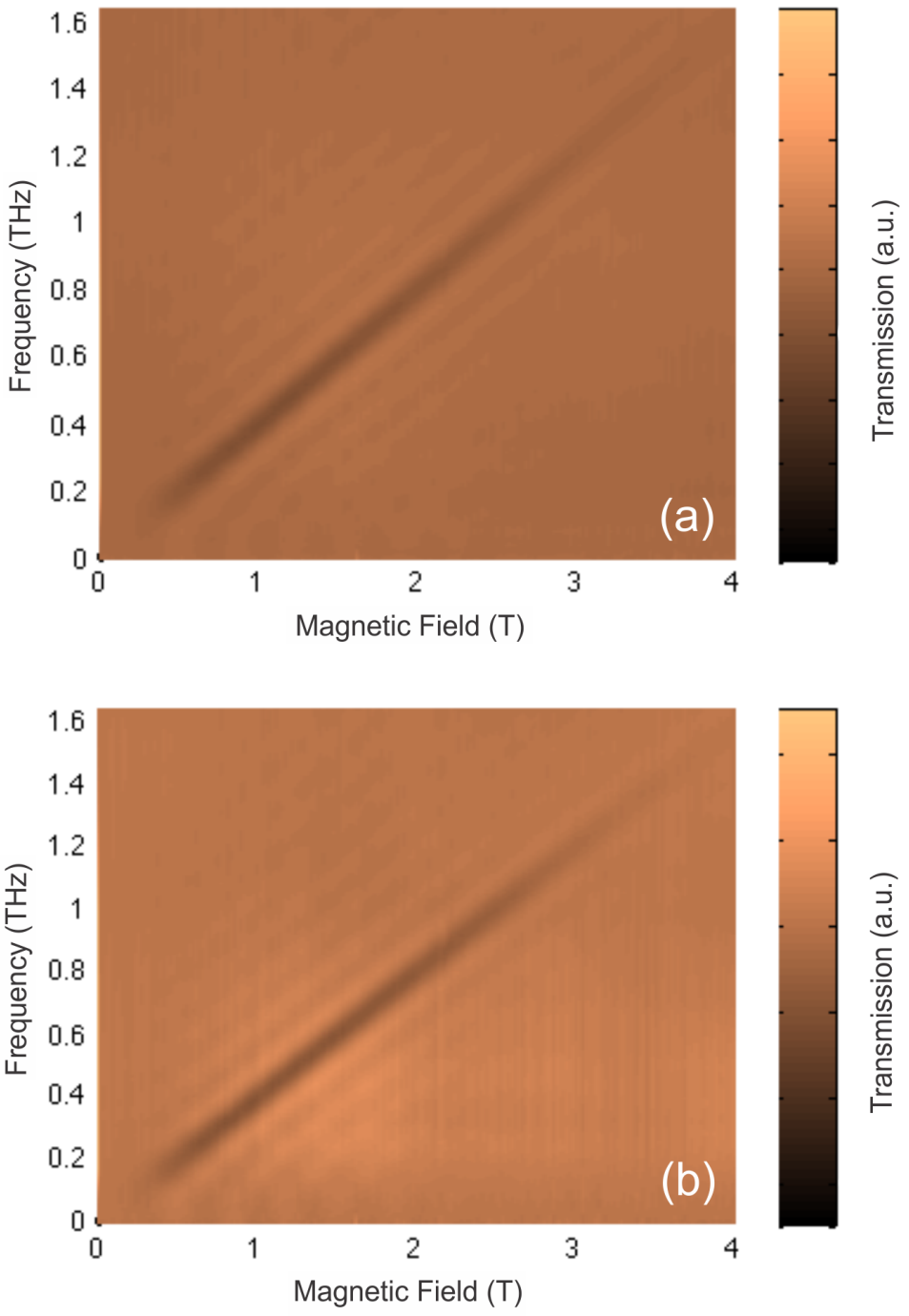

FIGURE 5.12: Experimental data for longitudinal part of conductivity both under (a) dark and (b) light conditions. Application of new data analysis technique almost removed features parallel to the cyclotron resonance for both dark and light conditions. The apparent change in the width of cyclotron resonance at high magnetic fields can be attributed to the signal to noise ratio of the system deteriorating at the upper limit of the system bandwidth.

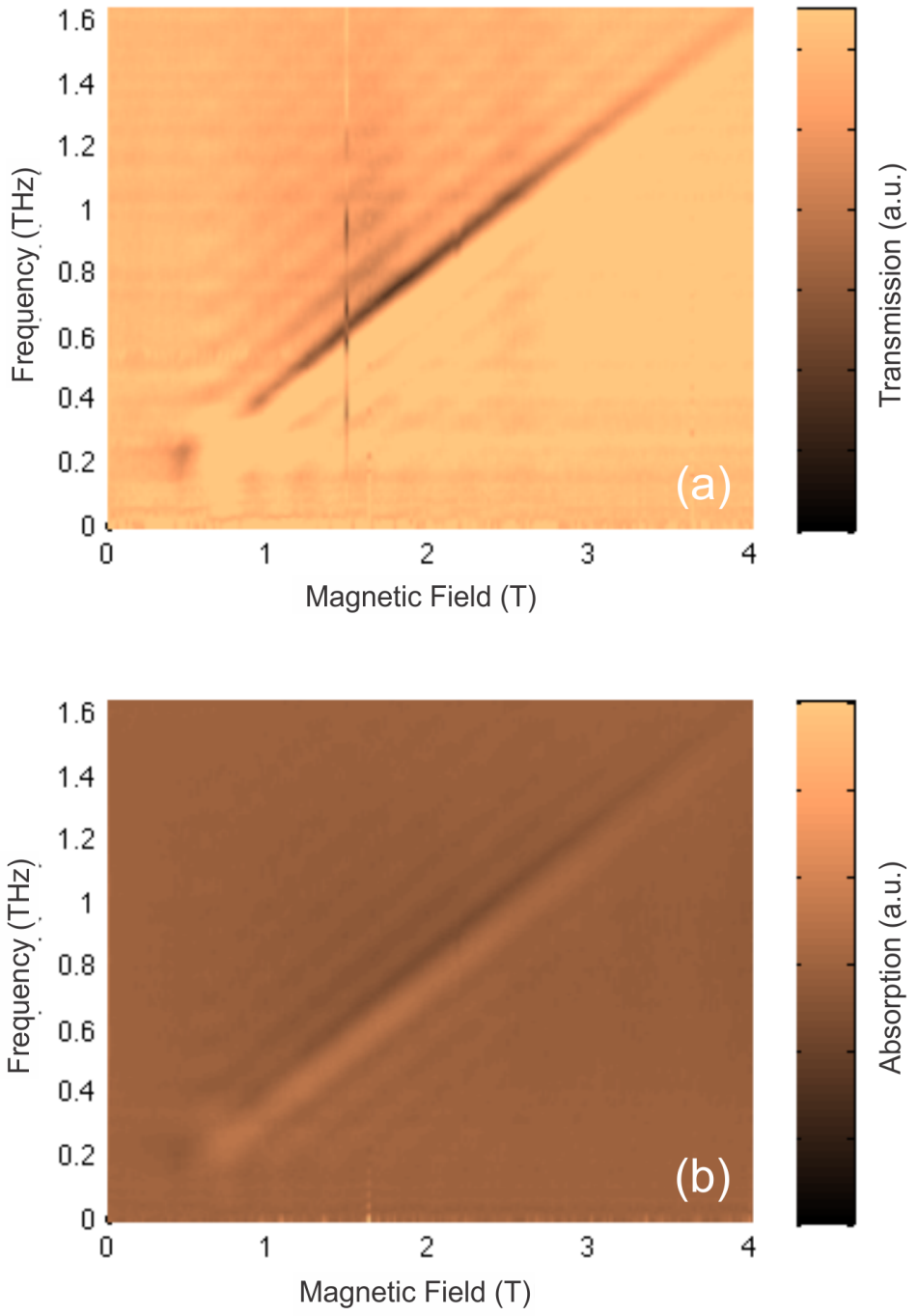

FIGURE 5.13: Experimental data for off-diagonal (Hall) part of conductivity both under (a) dark and (b) light conditions. Application of the new data analysis technique helped to supress features parallel to the cyclotron resonance for both dark and light conditions. The apparent change in the width of cyclotron resonance at low magnetic fields can be attributed to the signal to noise ratio of the system deteriorating at the lower limit of the system bandwidth.

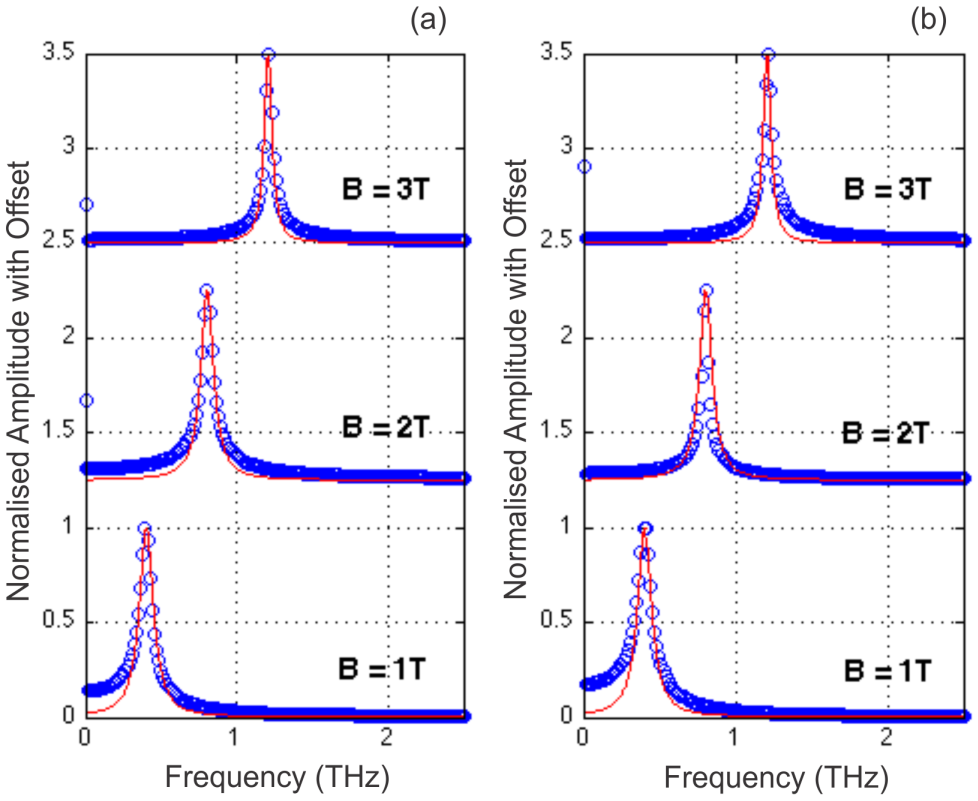

FIGURE 5.14: Real part of longitudinal conductivity of a 2DEG, both in (a) dark and (b) light conditions, for different values of magnetic field applied perpendicular to the surface of the 2DEG sample. Experimental results (blue circles) carry a very good agreement with simulated data (red line) based on the Drude model. The new data analysis technique resulted in no extra oscillations in the frequency domain data, with only cyclotron resonance being observable. The effective system bandwidth increased up to 2.2 THz because of the new fitting procedure.

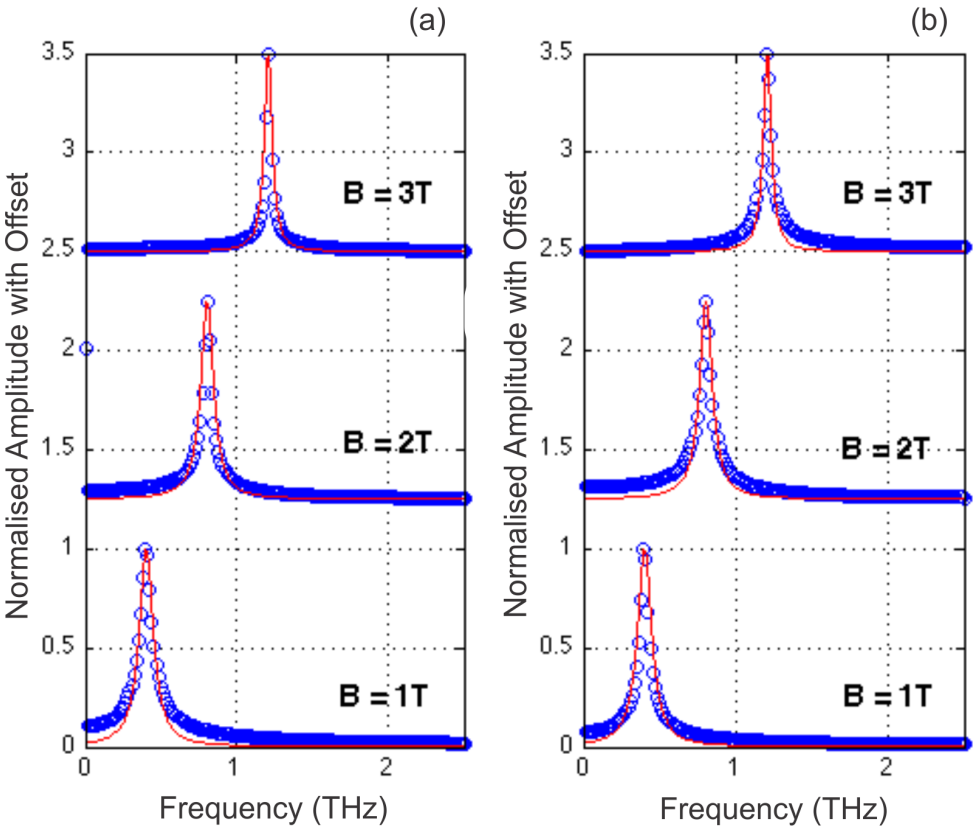

FIGURE 5.15: Real part of Hall conductivity of a 2DEG, both in (a) dark and (b) light conditions, for different values of magnetic field applied perpendicular to the surface of the 2DEG sample. Experimental results (blue circles) carry a very good agreement with simulated data (red line) based on the Drude model. The new data analysis technique resulted in no extra oscillations in the experimental data. Once again only cyclotron resonance can be observed in the plotted data.

5.5 Summary

Free-space transmission measurements of 2DEGs in GaAs/AlGaAs heterostructures, using a THz TDS system, have been demonstrated successfully. The real part of diagonal and off-diagonal conductivity of the 2DEG samples was evaluated. Extra features surrounding the cyclotron resonance were observed in the frequency domain for the transmission data. Simulations were performed to investigate the origin of these features. Also experiments were repeated for a range of magnetic fields in order to understand the behaviour of the newly observed features. Simulated data ruled out the possibilities of these features being magneto plasmon modes or multiple harmonics of the cyclotron resonance. It was determined, using further simulations, that these features were a direct consequence of the truncation of the time domain pulse. A new data analysis technique was devised in order to suppress these oscillations in the transmission data. Simulations of conductivity based on Drude model equations were carried out for the range of frequencies used in these experiments. The experimental results show good agreement with the simulated results for frequencies and magnetic fields up to 1.5 THz and 3.75T respectively. The effective system bandwidth also increased up to 2.2 THz because of the new fitting procedure. This technique can be employed to enhance the bandwidth of time domain THz systems where extra scattering introduced by optics and sample under test limits systems effective bandwidth.

Chapter 6

Edge-magneto-plasmons in two-dimensional electron gases

6.1 Introduction

In a two dimensional electron gas (2DEG), edge magneto plasmons (EMPs) can be defined as the collective excitations of electrons propagating along the edges of the 2DEG. EMPs can be considered as the dynamical equivalent of the Hall effect as they are driven by the Hall conductivity of the 2DEG. The direction of EMPs along the edges of the 2DEG is determined by the magnetic field and EMP wave vector. The velocity of EMP is proportional to the Hall conductivity of the 2DEG and can be evaluated by the Hall motion of electrons.

EMPs can be explained with a simplified model as shown in figure 6.1. Consider a finite sized 2DEG with a magnetic field perpendicular to the surface. In equilibrium, the net negative charge of electrons is balanced by the net positive charge of background in the system. If a charge density fluctuation i.e. a dipole is invoked, owing to the presence of an external electromagnetic wave hitting the 2DEG, by shifting the sheet of electrons relative to the positive background, it will manifest itself in the form of two oppositely charged strips (Figure 6.1(A)). Under the influence of the y-directed resultant electric field, electrons get accelerated and start moving inside the 2DEG.

The presence of a strong magnetic field leads to a much larger Hall current than the diagonal current. This results into a situation where electrons end up moving

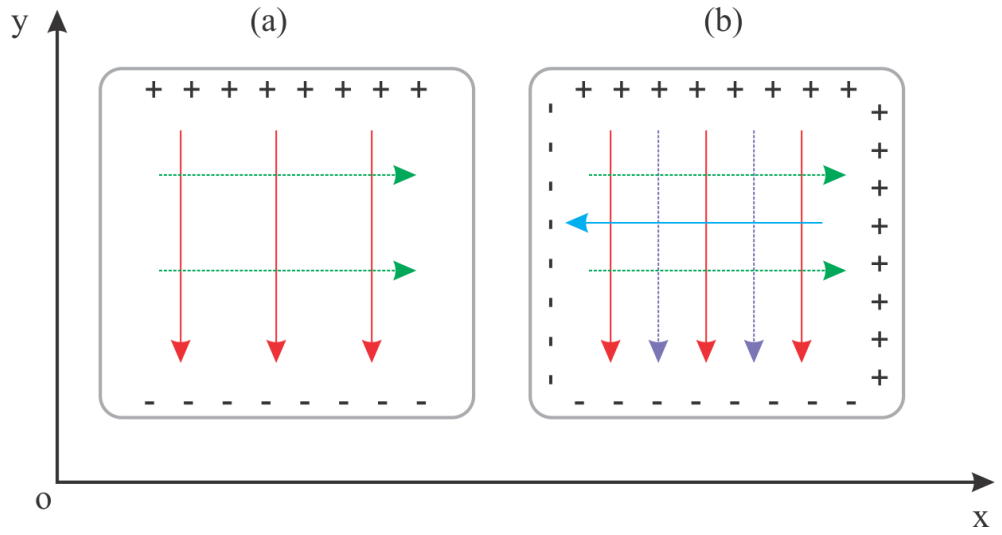

FIGURE 6.1: A simple schematic, representing a finite size 2DEG sample, to illustrate the EMPs in a strong magnetic field B at the initial (a) and subsequent (b) moments of time. Here electric charge is represented by + and –, electric field by solid arrows and electric current by dashed arrows. The magnetic field B is perpendicular to the surface of 2DEG.

in a direction perpendicular to the induced y-directed electric field. Consequently electrons move to the sides of 2DEG and accumulate there, which leads to the appearance of two extra oppositely charged strips (Figure 6.1(B)). So a secondary x-directed electric field is created, accompanied by a Hall current. The whole process leads to a situation where the oppositely charged strips along all edges of 2DEG keep on changing polarity and it is this oscillating process that is the essence of EMPs in a 2DEG [85].

6.2 Experimental apparatus

A free-space microwave system was designed (Figure 6.2), in which a single-frequency continuous-wave microwave signal was generated by up-converting a lower frequency RF signal from an oscillator source. The W-band microwave transmission module had an in-built multiplier that provided an output frequency six times that of the input. Electrical chopping was used to modulate the output signal for lock-in detection at 1.1 kHz. The microwave signal was transmitted into free space employing a corrugated horn antenna connected to the transmission module. An off-axis 2 parabolic mirror collected microwave-radiation from the source.

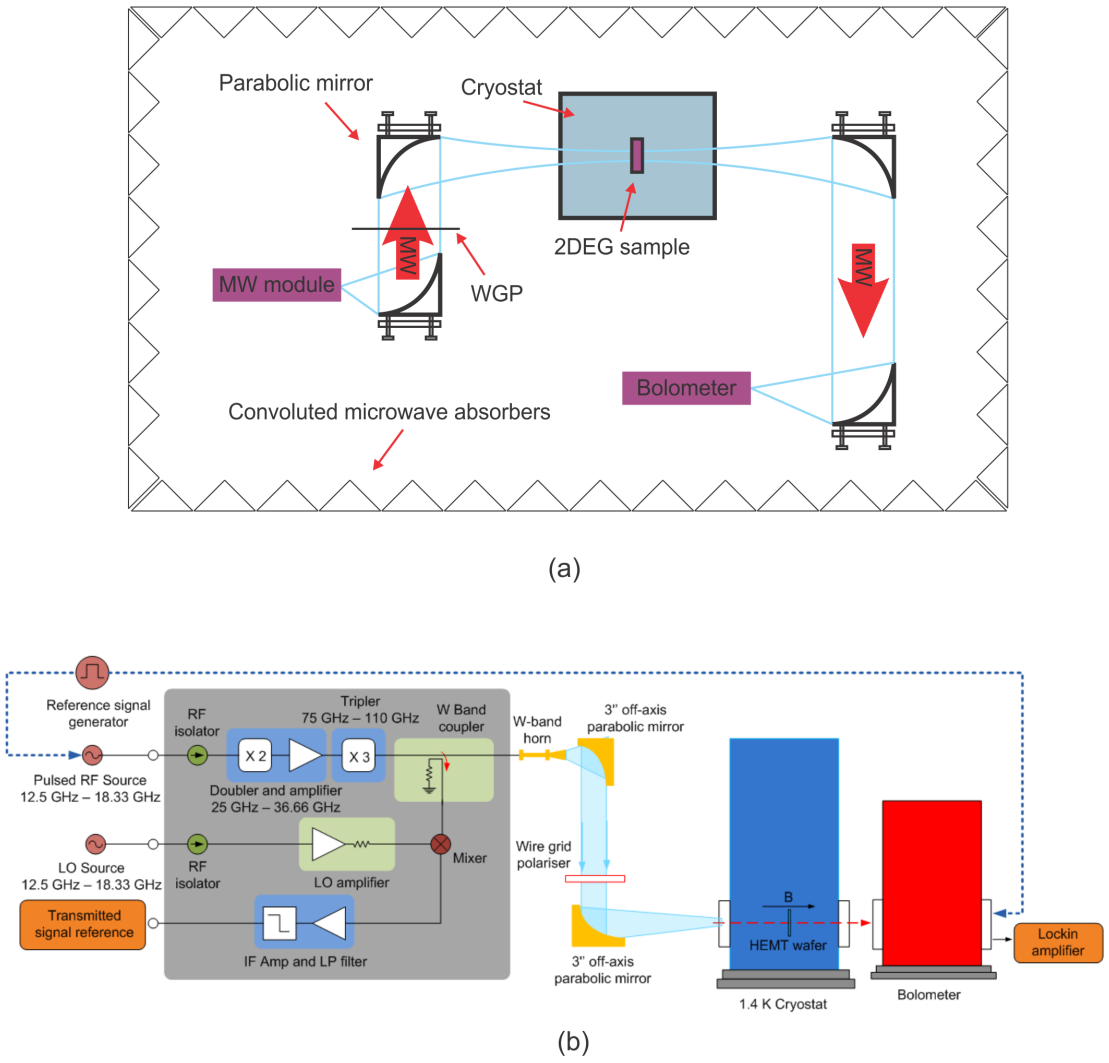

FIGURE 6.2: Experimental setup of free-space continuous wave single frequency W-band microwave system with (a) the actual optical arrangement for the free-space system and (b) simplified schematic of free-space system showing the multiplication-chain in detail. The microwave signal was transmitted by the W-band transceiver into free space using a corrugated horn antenna. A helium-cooled bolometer was employed to detect the signal. Ohmic contacts on the 2DEG sample were used to monitor any change in carrier concentration. Hall probes were used to record the DC Hall conductivity along with microwave induced voltage using a double modulation technique. Also shown are the WGP and convoluted absorbers that ensure a linearly polarised radiation directed towards the sample inside the cryostat and no spurious reflections in the free-space system.

A wire-grid polariser was placed in the path of the collimated beam, to ensure a linearly polarised electric field propagating towards the 2DEG sample inside the cryostat (held at the base temperature of 1.4 K). The collimated beam was then focused on to the 2DEG sample. A superconducting magnet provided a magnetic field perpendicular to the 2DEG sample surface in the range of 0 to 1T for these experiments. Convoluted microwave absorbers were used to avoid any reflections from the metallic shields placed at the edges of the optical bench.

After transmission through the 2DEG sample, a 2 inch parabolic mirror was used to collect microwave radiation. For detection purposes, the collimated beam was focused on to the centre of a helium-cooled bolometer, and the bolometer signal was measured using a lock-in amplifier. Four ohmic contacts on the square 2DEG sample provided the capability to monitor any change in carrier concentration along with the measurement of DC QHE and microwave induced photo-voltage.

6.3 Measurement technique

A 2DEG sample was used to study both the magneto-conductivity and microwave induced photo-voltage. The diagonal component of conductivity was measured by focusing the free-space microwave signal to the centre of bolometer after interaction with the 2DEG sample. It also provided a way to monitor any possible change in the longitudinal conductivity of the 2DEG owing to the presence of microwaves. A DC bias was applied across the ohmic contacts of the square sample at 33 Hz and the corresponding Hall voltage was monitored. The same Hall probes were used to record the microwave induced voltage using the double modulation technique, which involved feeding the signal from the signal monitor of first lock-in amplifier to a second one with a lock-in frequency of 1.1 kHz.

Measurements were taken over a magnetic field range of 0 to 1 T, both with and without microwave radiation incident on the 2DEG sample. Transmission data (using the bolometer) was also recorded for a range of scenarios i.e. with/without a DC bias across the 2DEG and with/without the Hall probes connected to the 2DEG sample to phase out any perturbation caused by either DC bias or Hall probes. Microwave-induced voltage was also monitored without any DC bias across the 2DEG sample.

6.4 Results and analysis

The experimental data shows the presence of microwave induced oscillatory features i.e. photo-induced voltage for a range of microwave frequencies (Figures 6.3, 6.4 and 6.6). The oscillatory features disappeared, when the microwaves were removed (Figure 6.3). The experimental data can be split into three individual sections i.e. 0 to 0.3T, 0.3 to 0.75T and 0.75 to 1T respectively (Figure 6.4). In the first section cyclotron resonance is the only dominant feature. In the second section microwave-induced oscillations are observed while in the last section SdH oscillations start to appear. With the microwave source off, both the cyclotron resonance and photo-voltage disappear as expected (Figure 6.3).

The observed oscillatory features can be attributed to interference of edge magneto-plasmons, given they satisfy the following two conditions; (a) the oscillations are periodic in B and (b) the oscillation period varies inversely with frequency. The experimental data for the microwave induced voltage (Figures 6.4 and 6.6) shows that the oscillations are periodic in B (Figure 6.5) and the oscillation period varies inversely with frequency (Figure 6.7). The microwave induced oscillations in the experimental data seem to satisfy the conditions for their being EMPs, so they may be attributed to the manifestion of EMPs in a 2DEG sample.

Since SdH oscillations start to appear beyond 0.75T so magnetic field range of 0 to 0.75T can be considered appropriate for the photo-induced oscillatory features (Figure 6.4). Beyond 0.75T EMPs are mixed with SdH oscillations (Figure 6.6). These features have been observed here for the first time in this frequency range and with this sample size (0.9x0.9 cm). It is pertinent to mention that spacing among plasmon modes has an inverse relationship with the dimensions of 2DEG sample. The highest previously reported frequency for EMPs in a 2DEG is 53 GHz, using a sample size of tens of micrometres. It has been reported that these oscillations have the same origin as that for the microwave induced extra oscillations in longitudinal resistivity at lower magnetic fields [86]. In contrast, these experiments did not reveal any extra oscillations in the DC longitudinal resistivity, which suggests that the photo voltage oscillations may have a different origin.

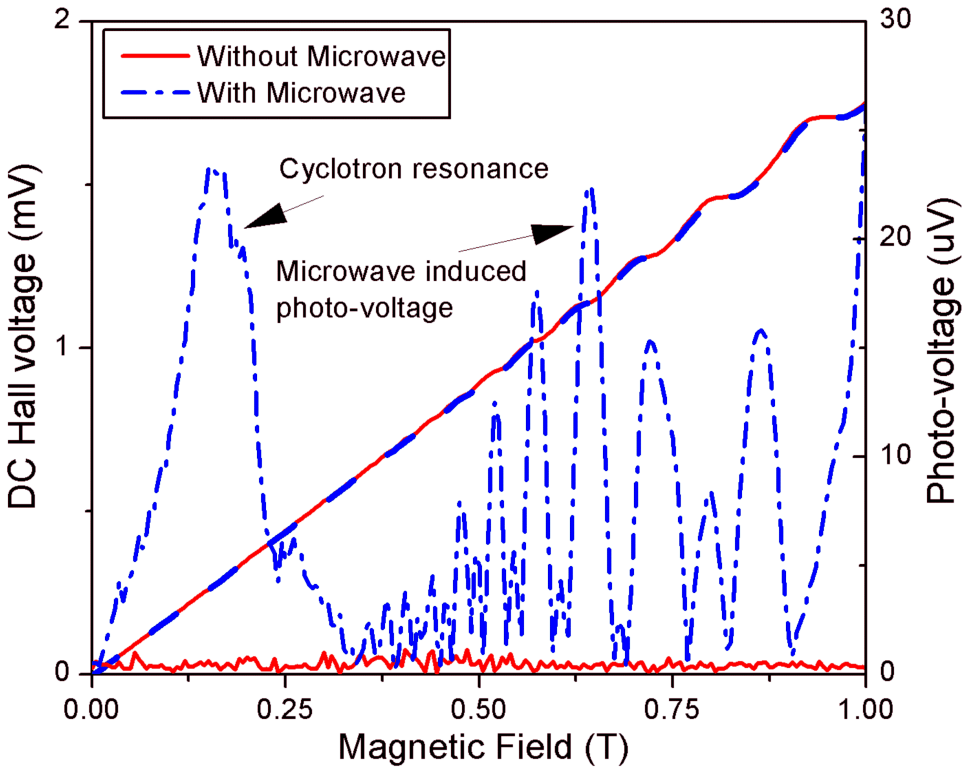

FIGURE 6.3: Measurement of DC Hall effect using the four ohmic contacts on the 2DEG square sample. The figure shows the presence of microwave induced photo voltage along with cyclotron resonance (blue line). Current through the 2DEG sample was modulated at 33 Hz for lock-in detection, while microwave radiation was modulated at 1.1 kHz. Double lock-in detection was employed to record the photo-induced voltage. Also shown is the data (using same x and y scales) with no microwave radiation incident on the 2DEG sample (red line).

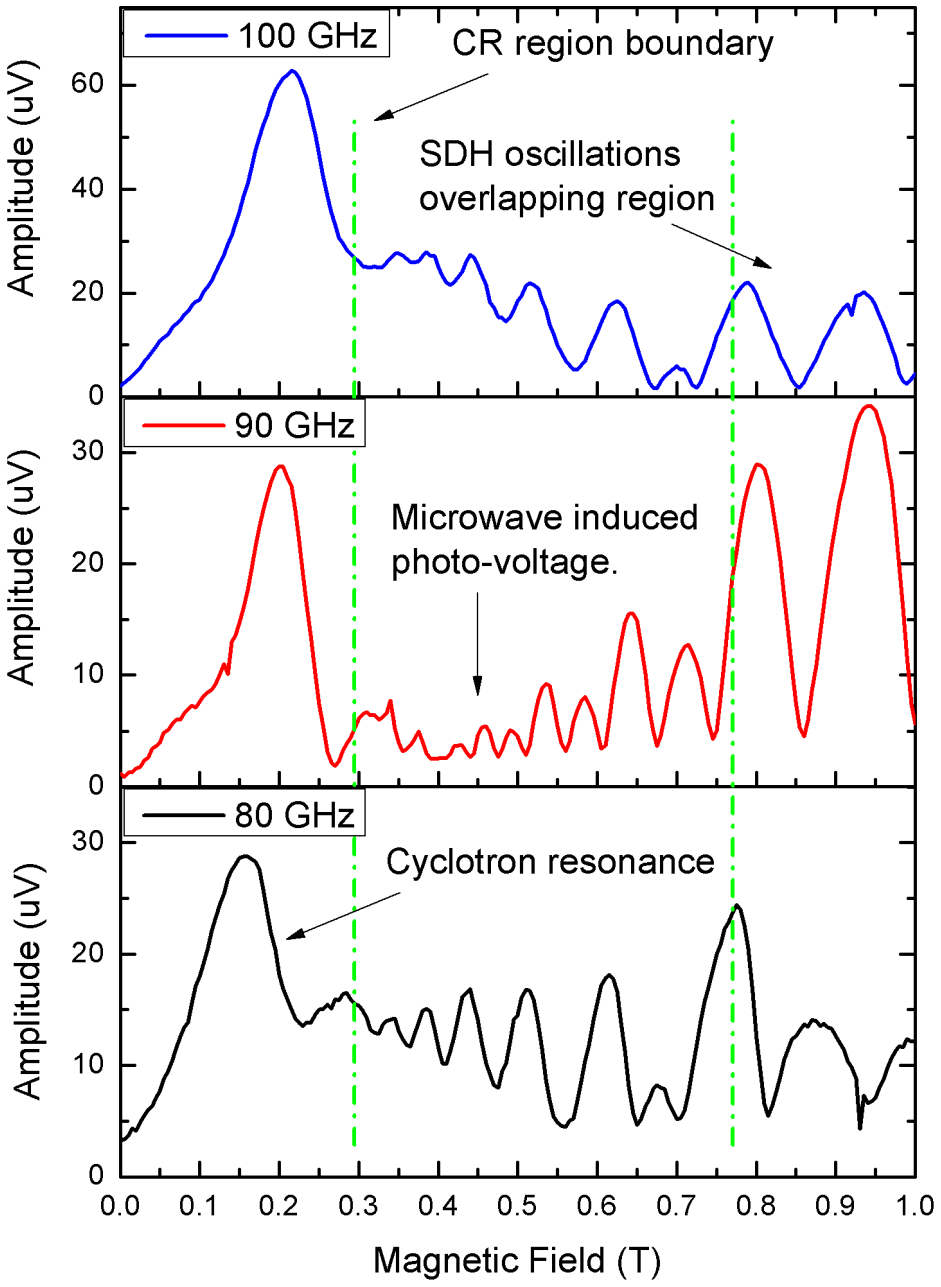

FIGURE 6.4: Measurement of microwave induced photo voltage using the double modulation technique. The data can be split into three individual sections showing cyclotron resonance (0 – 0.3T), microwave induced oscillations (0.3 – 0.75T) and SdH oscillations (0.75 – 1T). SdH oscillations are periodic in 1/B while the microwave induced oscillations are periodic in B.

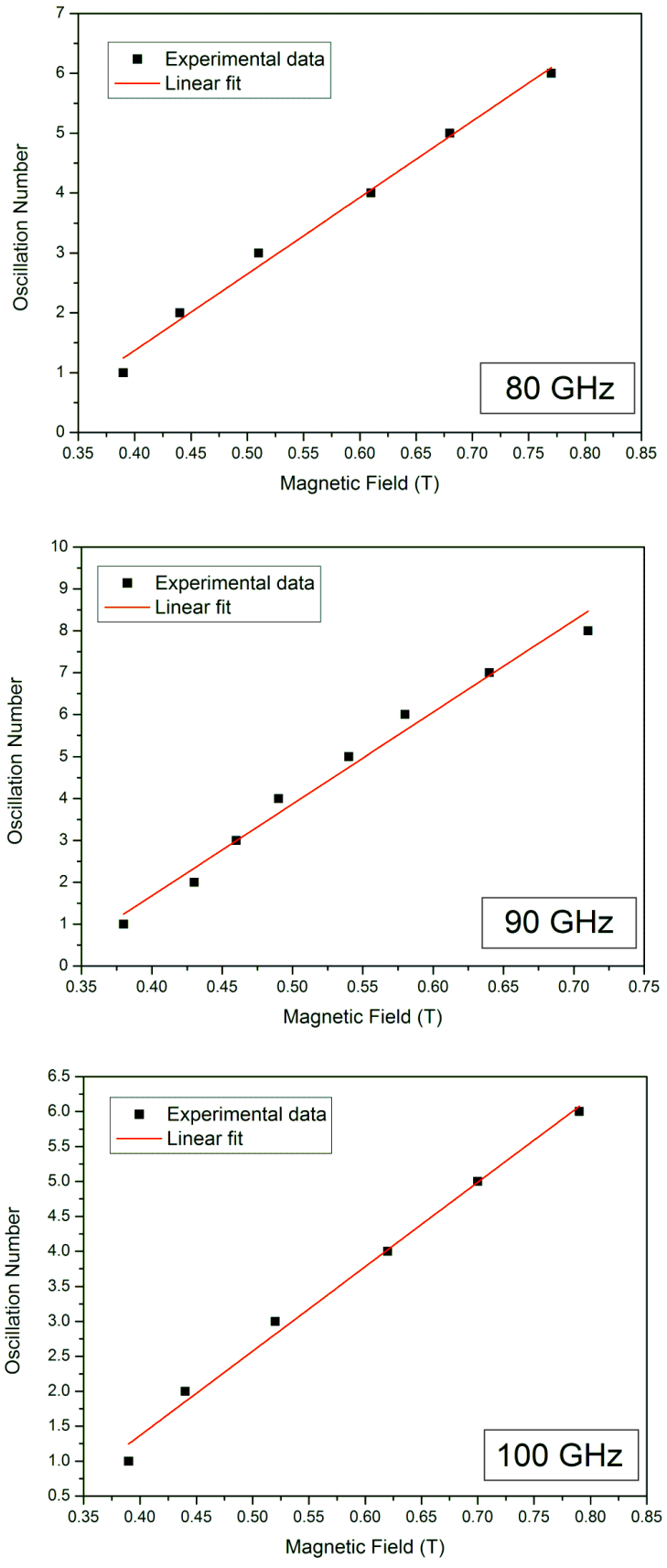

FIGURE 6.5: Individual microwave induced photo voltage oscillations plotted against B at 80, 90 and 100 GHz, showing that they are periodic in B.

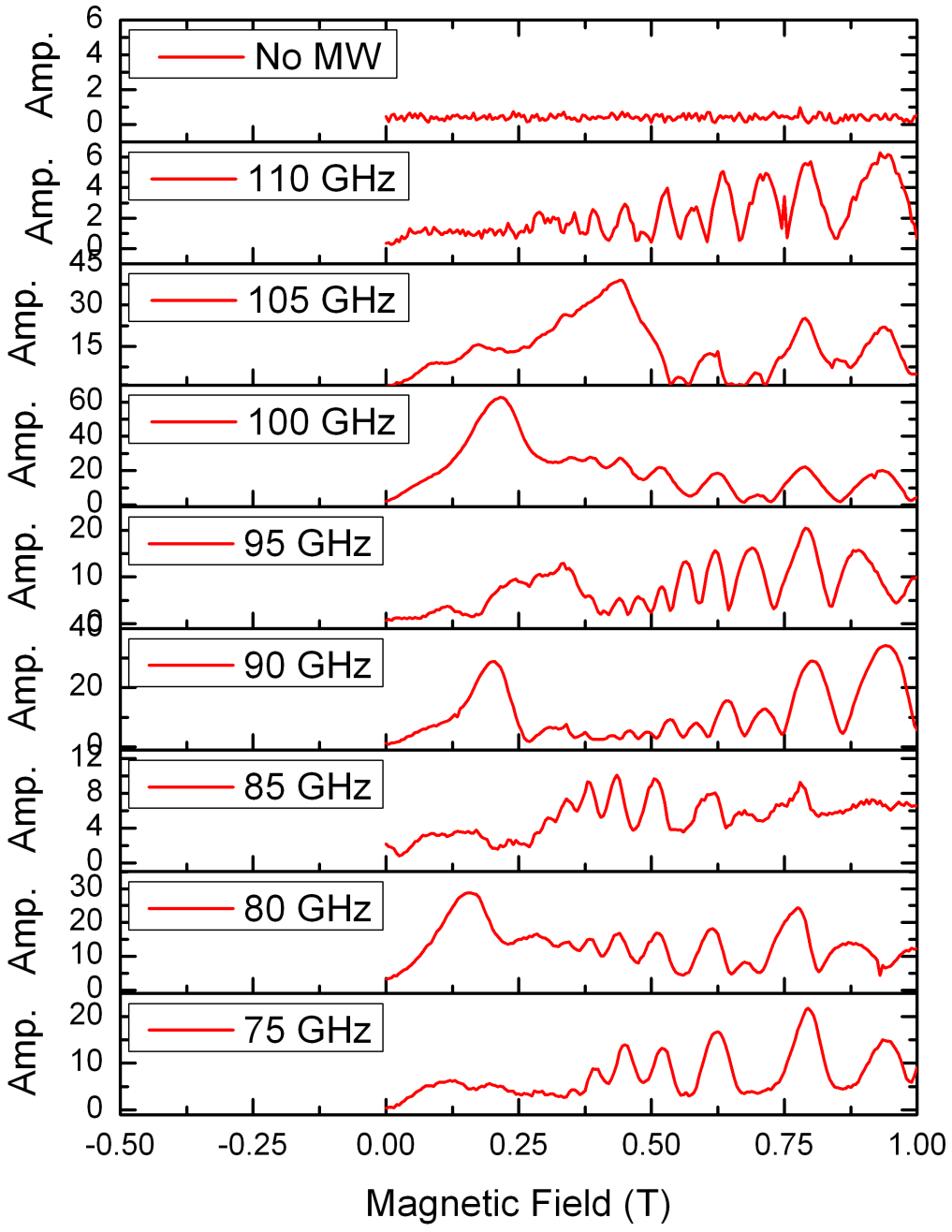

FIGURE 6.6: Measurement of microwave induced photo voltage at different frequencies namely 75, 80, 85, 90, 95, 100, 105 and 110 GHz. Double modulation technique was used to record this data. DC bias was applied at 33 Hz through the 2DEG sample while microwave radiation was electronically chopped at 1.1 kHz. The trace on the very top shows the recorded data when microwave source was turned off.

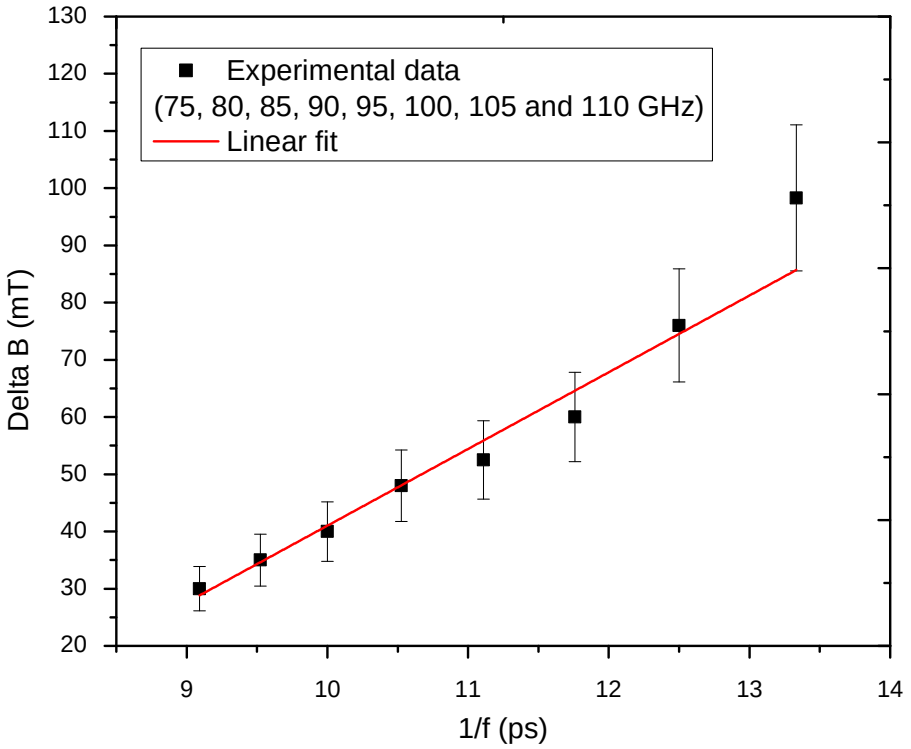

FIGURE 6.7: Plot of the period of microwave induced photo voltage vs. reciprocal of frequency, which should be a straight line for edge-magneto plasmons [86]. Delta B plotted here is the average of delta B for all oscillations up to 0.75T for any given frequency.

6.5 Summary

A free space microwave system, operating in the frequency range of 75 to 110 GHz, has been demonstrated successfully with a capability of recording both the longitudinal conductivity of the 2DEG and the microwave induced photo voltage simultaneously. Oscillatory features, which can be attributed to interference of EMPs, have been observed for a range of microwave frequencies. A detailed investigation about the origin of these features and their ability to couple into the conductivity of 2DEG is required. Repeating the measurements using different microwave powers, a range of sample temperatures and 2DEG samples with different width and carrier concentration is required to confirm this.

Chapter 7

Conclusion and future work

7.1 Conclusion

Formation of a 2DEG in GaAs/AlGaAs heterostructures presents a gateway to study the dynamic behaviour of electrons confined in two-dimensional space. GaAs/AlGaAs heterostructures provide an advantage over other types of 2DEG systems, as electrons are physically separated from the scattering centres. A number of experimental techniques have been used to study the dynamic behaviour of electrons confined in two-dimensional space. Frequency and time domain polarisation sensitive systems operating at microwave and THz frequencies have been demonstrated and the results have been reported to Applied Physics Letters [89] and EP2DS-19/MSS-15 [94].

Free-space THz polarisation sensitive systems

Polarisation sensitive systems enable the measurement of both orthogonal components of the electric field in a propagating wave. Two polarisation sensitive systems have been designed with the aim of studying both parts of 2DEG conductivity, simultaneously, at THz frequencies. The performance of the first system, with two ZnTe crystals, has been demonstrated by measuring the birefringence of $LiNbO_3$ at room temperature. The performance of the second system, with a three terminal detector, with two photo-conductive gaps, has been evaluated by recording its extinction ratio for an incoming linearly polarised THz beam.

Time domain magneto-spectroscopy of two dimensional electron systems

A free-space THz-TDS system has been designed in order to study the dynamic response of a 2DEG at THz frequencies. A super-conducting magnet is also incorporated into the free space system with a magnetic field perpendicular to the surface of the 2DEG sample. The THz system had a useful bandwidth up to 1.5 THz and a magnetic field range of 0 to 6T. Both longitudinal and off-diagonal parts of 2DEG conductivity have been measured experimentally. The experimental data agrees well with theory based on the Drude model. A comparison of data from the TDS system with that from continuous wave systems shows a certain discrepancy in the TDS data. The cyclotron resonance feature is asymmetric in both continuous wave systems, unlike in the TDS system where it is symmetric. This can be attributed to the data analysis technique used in the TDS system, which was compromised owing to the presence of a reflection peak in close proximity to the main pulse peak in the time domain data. Simulations were done to rule out the possibility of extra oscillatory features in the experimental data being a manifestation of magneto plasmon modes or multiple cyclotron resonances in the 2DEG sample. Simulations were also done to show that the small window size of the time domain pulse resulted into the extra features in transmission data and they were removed using the modified data analysis technique based on further simulations.

Measurement of magneto conductivity of 2DEG using continuous wave systems

Two continuous wave free space systems have been used to study the dynamic response of the 2DEGs. A W-band free-space microwave system has been used to study the conductivity of 2DEG in the frequency range of 75 to 110 GHz. The experimental results show good agreement with the Drude model. Also a free-space THz system based on QCLs, operating around 2.6 and 3.1 THz, has been used to study the conductivity of the 2DEG. Again the experimental data is in good agreement with the Drude model.

Edge-magnetoplasmons in 2DEG using continuous wave microwave system

Preliminary experimental results suggest the presence of microwave induced edge-magneto plasmons measured using a free space W-band microwave system. The presence of edge-magneto plasmons was confirmed through showing that the oscillations were periodic in B and that their period was inversely proportional to the frequency of the microwave radiation. This plasmon behaviour has been measured at these frequencies and sample size used for the first time.

7.2 Recommendations for Future Work

In future, a number of techniques can be used to further study the presence of the QHE at microwave and THz frequencies along with the presence of induced edge magneto plasmons at such high frequencies.

Polarisation sensitive systems

Preliminary experimental results suggest that edge magneto plasmons can be coupled into the magneto conductivity response of the 2DEG. So such polarisation sensitive systems can be designed both at microwave and THz frequencies that can detect both components of electric field polarisation simultaneously (Figs. 7.1 and 7.2). A free space microwave polarisation sensitive system in shown in figure 7.1. Here one component of electric polarisation is detected using bolometer while the other component is detected using the microwave module that down-converts the free space microwave radiation to a much lower frequency, (few kilohertz), before detection by the lock-in amplifier. Figure 7.2 shows a free space THz polarisation sensitive system. Here one component of electric field is detected by the bolometer while the other component is detected by the QCL itself using the self mixing scheme. An optical chopper is used for lock-in detection in such a system.

Edge magneto plasmons in two dimensional electron systems

The presence of edge magneto plasmons in the 2DEG can be recorded using the ohmic contacts on the 2DEG sample. Both free space systems shown in figures 7.1 and 7.2 may be used to study the edge magneto plasmons at microwave and THz frequencies. Also large Hall bars and small square samples may be used to study the presence of edge magneto plasmons along with their coupling into the cyclotron resonance using free space TDS and continuous wave systems. A systematic study of edge-magneto plasmons, induced by free space microwave and THz radiation, is required by varying different parameters such as 2DEG sample temperature, power of microwave/THz radiation and sample size.

Study of quantum Hall effect using continuous wave systems

Initial results obtained using free space continuous wave microwave and THz systems suggest that the QHE does not exist at such high frequencies, unlike what is reported in the literature. Both free space systems (Figs. 7.1 and 7.2) may be used to investigate the presence of the QHE at such high frequencies in a systematic manner.

Systematic study of cyclotron resonance in two dimensional electron systems

It has been observed experimentally using free space continuous wave systems that cyclotron resonance is asymmetric in shape, but this has not been observed using the free space THz TDS system. So a detailed investigation is required to study the asymmetric behaviour of cyclotron resonance using 2DEG samples with different carrier densities and mobilities along with different temperatures.

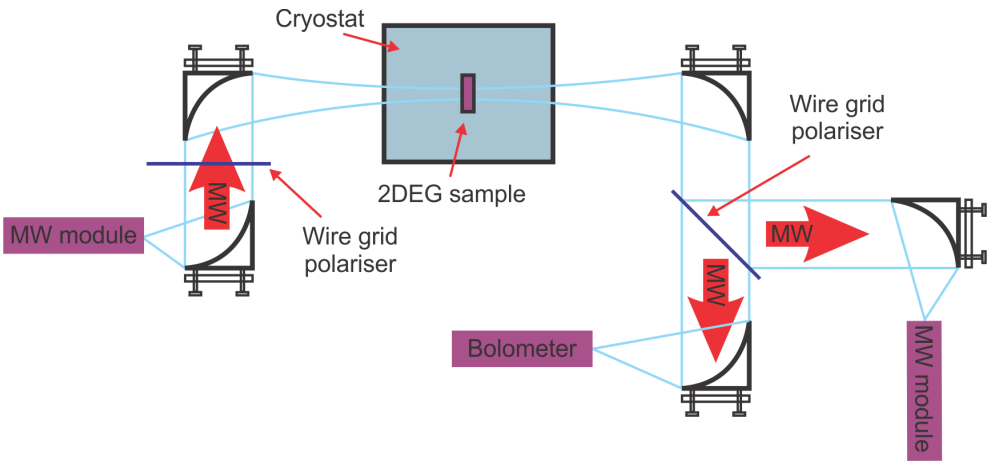

FIGURE 7.1: A free-space microwave polarisation sensitive system to detect both components of electric field polarisation simultaneously. A continuous microwave source is electrically modulated before connecting it to the microwave transceiver module that up converts the microwave signal by six times. Modulated microwave radiation is launched into free space from MW transceiver module employing a W-band horn antenna. A wire-grid polariser splits the radiation into two orthogonal components, after interaction with the 2DEG sample, which is subsequently detected using microwave module and bolometer respectively. Lock-in amplifiers are used to detect the modulated signals from bolometer and microwave module. A low noise amplifier is used in between microwave module and lock-in amplifier which provides 40dBm amplification. Ohmic contacts on the 2DEG sample can be used to monitor any change in carrier density along with the presence of edge-magneto plasmons using double modulation technique. Also shown is the wire-grid polariser to ensure linearly polarised radation directed towards the sample inside the cryostat.

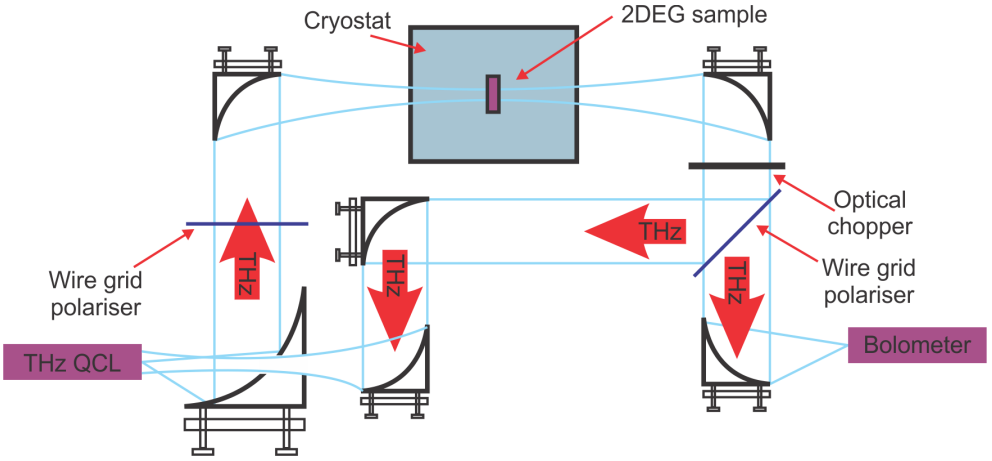

FIGURE 7.2: A free-space THz polarisation sensitive system to detect both components of THz electric field simultaneously. THz QCL is operated in continuous wave mode. THz radiation from QCL is split into x and y components, after interaction with 2DEG sample, which is detected using bolometer and QCL itself using self mixing technique. An optical chopper is used for lock-in detection. Ohmic contacts on the 2DEG sample can be used to monitor any change in carrier density along with the presence of edge-magneto plasmons using double modulation technique. A de-focused THz beam is used at the centre of the cryostat in order to ensure that it covers all four ohmic contacts as well. Also shown is the wire-grid polariser to ensure linearly polarised radation directed towards the sample inside the cryostat.

Appendix A

Magneto-conductivity tensor of 2DEG in GaAs/AlGaAs

A THz wave propagates through the two-layer sample (Figure 3.9) and induces a current in the conducting layer. It is assumed that the volume force acting on the current is the Lorentz force;

$$F(t) = \rho\,(\ \underline{E}(t)\ +\ \underline{v}(t) \times \underline{B}\ ) \tag{A.1}$$

ρ = Charge density

and also that the current has a linear dependence on this force;

$$\underline{J}(t) = A\rho\,(\ \underline{E}(t)\ +\ \underline{v}(t) \times \underline{B}\ ) \tag{A.2}$$

A = Constant

The general relation between $\underline{J}$ and $\underline{E}$ is established as follows:

From equation 3.2;

$$\underline{J}(t) = A\,(\ \rho\underline{E}(t)\ +\ \underline{J}(t) \times \underline{B}\ )$$

Writing $\underline{J}(t)$ and $\underline{E}(t)$ as Fourier integrals;

$$\underline{J}(t) = \int_{-\infty}^{\infty} \underline{J}_{\omega}\ e^{-j(\omega t - \phi)}\ d\omega$$

$$\underline{J}(t) = \int_{-\infty}^{\infty} \underline{E}_{\omega}\ e^{-j\omega t}\ d\omega$$

the above equation can be re-written as;

$$\underline{J}_{\omega}\ e^{-j(\omega t\ -\ \phi)} = A\left[\ \rho\underline{E}_{\omega}\ e^{-j\omega t}\ \times\ \underline{J}_{\omega}\ e^{-j(\omega t\ -\ \phi)} \times B\ \right] \tag{A.3}$$

The x, y and z components of $\underline{J}$, $\underline{E}$ and $\underline{B}$ are, respectively (Figure 1);

$$\underline{J}_{\omega} = \begin{pmatrix} J_{\omega x}\ e^{-j(\omega t\ -\ \phi_x)} \\ J_{\omega y}\ e^{-j(\omega t\ -\ \phi_y)} \\ 0 \end{pmatrix}\ ,\quad \underline{E}_{\omega} = \begin{pmatrix} E_{\omega x}\ e^{-j\omega t} \\ E_{\omega y}\ e^{-j\omega t} \\ 0 \end{pmatrix}\ ,\quad \underline{B} = \begin{pmatrix} 0 \\ 0 \\ B_z \end{pmatrix}$$

Substituting into equation 3.3, dropping the subscript ω, and cancelling the $e^{-j\omega t}$ terms;

$$J_x\ e^{j\phi_x} = A\left[\ \rho E_x\ +\ J_y\ e^{j\phi_y}\ B_z\ \right] \tag{A.4}$$

$$J_y\ e^{j\phi_y} = A\left[\ \rho E_y\ -\ J_x\ e^{j\phi_x}\ B_z\ \right] \tag{A.5}$$

From equation 3.4;

$$J_y\ e^{j\phi_y} = \frac{1}{AB_z}\left[\ J_x\ e^{j\phi_x}\ -\ \gamma\rho E_x\ \right]$$

Substituting into 3.5;

$$\frac{1}{AB_z}\left[\ J_x\ e^{j\phi_x}\ -\ A\rho E_x\ \right] = A\left[\ \rho E_y\ -\ J_x\ e^{j\phi_x}B_z\ \right]$$

$$J_x\ e^{j\phi_x}\left[\ 1\ +\ A^2B_z^2\ \right] = A\rho E_x\ +\ A^2\rho B_z E_y$$

$$J_x = \frac{A\rho\ e^{-j\phi_x}}{(1\ +\ A^2B_z^2)}\ E_x\ +\ \frac{A^2\rho B_z\ e^{-j\phi_x}}{(1\ +\ A^2B_z^2)}\ E_y$$

$$J_x = \left(\ \sigma_{xx}^{'}\ +\ j\sigma_{xx}^{''}\ \right)E_x\ +\ \left(\ \sigma_{xy}^{'}\ +\ j\sigma_{xy}^{''}\ \right)E_y \tag{A.6}$$

Substituting into 3.4;

$$J_y = \frac{-A^2\rho B_z\ e^{-j\phi_y}}{(1\ +\ A^2B_z^2)}\ E_x\ +\ \frac{A\rho\ e^{-j\phi_y}}{(1\ +\ A^2B_z^2)}\ E_y$$

$$J_y = \left(\ \sigma_{yx}^{'}\ +\ j\sigma_{yx}^{''}\ \right)E_x\ +\ \left(\ \sigma_{yy}^{'}\ +\ j\sigma_{yy}^{''}\ \right)E_y \tag{A.7}$$

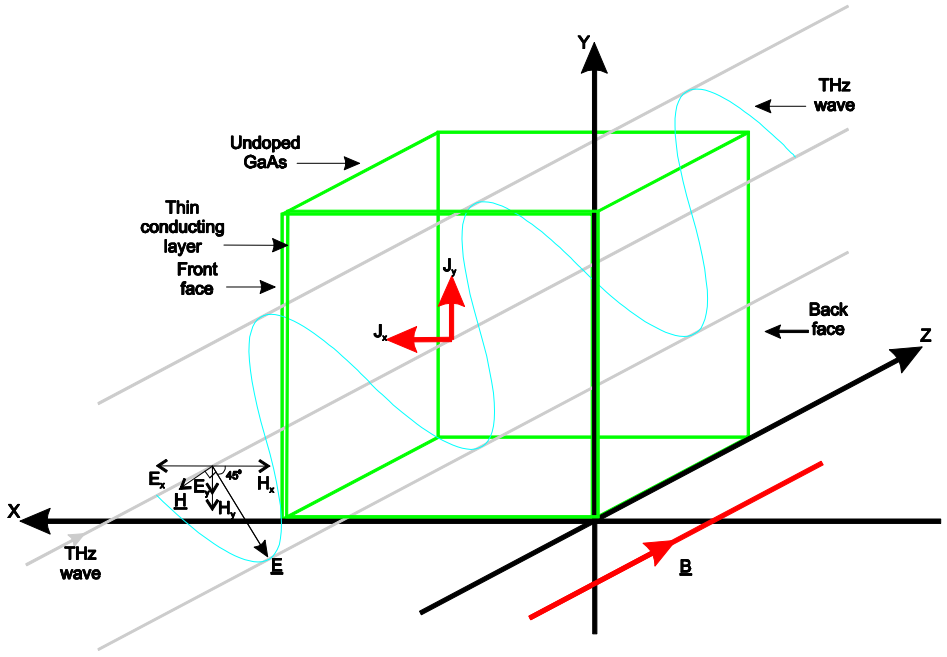

FIGURE A.1: Semiconductor sample containing 2DEG with THz signal propagating through it.

For an isotropic sample, the phase lag ϕ of $\underline{J}$ is the same for both x and y directions, i.e. $\phi_x = \phi_y$, therefore;

$$\sigma_{xx}^{'} + j\sigma_{xx}^{''} = \sigma_{yy}^{'} + j\sigma_{yy}^{''}$$

$$\sigma_{xy}^{'} + j\sigma_{xy}^{''} = -\left(\sigma_{yx}^{'} + j\sigma_{yx}^{''}\right)$$

The general relation between $\underline{J}$ and $\underline{E}$ may therefore be written as;

$$\begin{pmatrix} J_x \\ J_y \end{pmatrix} = \begin{pmatrix} \sigma_{xx}^{'} + j\sigma_{xx}^{''} & \sigma_{xy}^{'} + j\sigma_{xy}^{''} \\ -\sigma_{xy}^{'} - j\sigma_{xy}^{''} & \sigma_{xx}^{'} + j\sigma_{xx}^{''} \end{pmatrix} \begin{pmatrix} E_x \\ E_y \end{pmatrix}$$

The quantities σ_{xx} etc may be found from the measured THz signals by relating the transmitted fields to the current distribution (J_x, J_y) in the conducting layer. The relations are established by considering the boundary conditions for the fields at the front and back faces of the sample.

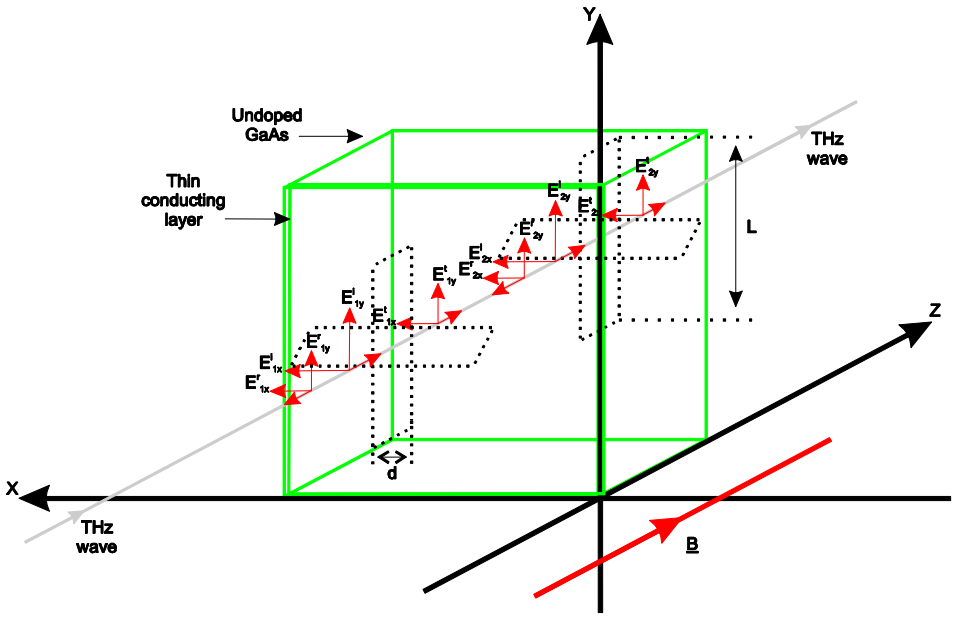

FIGURE A.2: THz electric field represented in terms of incident (i), reflected (r) and transmitted (t) components.

A.0.1 Boundary Conditions at the Front Face:

The THz electric field is resolved into incident (i), reflected (r) and transmitted (t) components (Figure 3.10).

Integrating the Maxwell equation;

$$\oint \underline{E} \cdot d\underline{l} = \frac{-\partial}{\partial t} \oint \underline{H} \cdot d\underline{S}$$

($\mu = 1$)

Around the loop in the x-z plane in Figure 3.10;

$$E^i_{1x}(t)L \; + \; E^r_{1x}(t)L \; - \; E^t_{1x}(t)L = \frac{-\partial}{\partial t} \left[\; H_x(t)Ld \; \right]$$

Letting d $\rightarrow$ 0, the R.H.S also $\rightarrow$ 0;

$$E^i_{1x}(t) \; + \; E^r_{1x}(t) \; - \; E^t_{1x}(t) = 0$$

Using the Fourier integral representation;

$$\int_{-\infty}^{\infty} E^i_{1x}(\omega)\, e^{-j\omega t}\, d\omega + \int_{-\infty}^{\infty} E^r_{1x}(\omega)\, e^{-j(\omega t \, - \, \phi^r_x)}\, d\omega - \int_{-\infty}^{\infty} E^t_{1x}(\omega)\, e^{-j(\omega t \, - \, \phi^t_x)}\, d\omega = 0$$

Where ϕ_x^r and ϕ_x^t are the phase shifts in E_x due to reflection and transmission, respectively.

In the frequency domain;

$$E_{1x}^i \; + \; E_{1x}^r \; e^{j\phi_x^r} \; - \; E_{1x}^t \; e^{j\phi_x^t} = 0 \tag{A.8}$$

A similar relation is also obtained for E_y using the loop in the y-z plane;

$$E_{1y}^i \; + \; E_{1y}^r \; e^{j\phi_y^r} \; - \; E_{1y}^t \; e^{j\phi_y^t} = 0 \tag{A.9}$$

The magnetic field is similarly resolved into components by integrating a second Maxwell equation;

$$\oint \underline{H} \cdot d\underline{l} = \oint \underline{J} \cdot d\underline{S}$$

For the loop in the y-z plane (Figure 3.10);

$$H_{1y}^i(t)L \; - \; H_{1y}^r(t)L \; - \; H_{1y}^t(t)L = J_x(t)Ld$$

The loop width (d) is again allowed to approach zero, and the current density (J_x) to approach infinity, in such a way that the product $J_x d$ = constant.

$$H_{1y}^i(t) \; - \; H_{1y}^r(t) \; - \; H_{1y}^t(t) = J_x(t)$$

Again using the Fourier representation, and equation 3.6, the following expression is obtained in the frequency domain;

$$H_{1y}^i \; - \; H_{1y}^r \; e^{j\phi_y^r} \; - \; H_{1y}^t \; e^{j\phi_y^t} = \sigma_{xx} \left[\; E_{1x}^i \; + \; E_{1x}^r \; e^{j\phi_x^r} \; \right] \; + \; \sigma_{xy} \left[\; E_{1y}^i \; + \; E_{1y}^r \; e^{j\phi_y} \; \right] \tag{A.10}$$

Equation 3.10 can be re-written entirely in terms of $\underline{E}$ which allows σ_{xx}, σ_{yy} to be related to measurable transmission or reflection coefficients for $\underline{E}$. This is done by first using the Maxwell equation;

$$\underline{\nabla} \; \times \; \underline{E} = \frac{-\partial \underline{H}}{\partial t}$$

Writing $\underline{E}$ and $\underline{H}$ as Fourier integrals, the Fourier coefficients are related by;

$$\begin{vmatrix} \underline{i} & \underline{j} & \underline{k} \\ \frac{\partial}{\partial x} & \frac{\partial}{\partial y} & \frac{\partial}{\partial z} \\ E_x & E_y & 0 \end{vmatrix} = -j\omega \begin{pmatrix} H_x \\ H_y \\ H_z \end{pmatrix}$$

$$\frac{-\partial E_y}{\partial z} = -j\omega H_x \quad ; \quad \frac{\partial E_x}{\partial z} = -j\omega H_y \tag{A.11}$$

The derivatives are evaluated by considering the form of the coefficient E_x and E_y, which can be deduced from the wave equation for the THz fields;

$$\nabla^2 \underline{E} \; + \; \frac{n^2}{c^2} \frac{\partial^2 \underline{E}}{\partial t^2} = 0$$

In the frequency domain;

$$\nabla^2 \underline{E}_\omega \; - \; \frac{n^2 \omega^2}{c^2} \underline{E}_\omega = 0$$

$$\frac{\partial^2 \underline{E}_\omega}{\partial z^2} = \frac{n^2 \omega^2}{c^2} \underline{E}_\omega$$

$$\underline{E}_\omega = \underline{E}_0 \; e^{\pm jknz}$$

Only the positive solution (jknz) is physically meaningful, since it describes a travelling wave, i.e.

$$\underline{E}(t) = \int_{-\infty}^{\infty} \underline{E}_\omega \; e^{-j\omega t} d\omega = \int_{-\infty}^{\infty} \underline{E}_0 \; e^{j(kz \; - \; \omega t)} d\omega$$

Equations 3.11 therefore become;

$$nkE_y = \omega H_x \quad , \quad nkE_x = -\omega H_y \tag{A.12}$$

Substituting 3.12 into 3.10;

$$\frac{-k}{\omega} E^i_{1x} + \frac{k}{\omega} E^r_{1x} \, e^{j\phi^r_x} + \frac{nk}{\omega} E^t_{1x} \, e^{j\phi^t_x} = \sigma_{xx} \left[\; E^i_{1x} \; + \; E^r_{1x} \, e^{j\phi^r_x} \; \right] + \sigma_{xy} \left[\; E^i_{1y} \; + \; E^r_{1y} \, e^{j\phi^r_y} \; \right]$$

Using equations 3.8 and 3.9 to eliminate the reflection terms;

$$\frac{-k}{\omega} E^i_{1x} \; + \; \frac{k}{\omega} \left[\; E^t_{1x} \, e^{j\phi^t_x} \; - \; E^i_{1x} \; \right] \; + \; \frac{nk}{\omega} E^t_{1x} \, e^{j\phi^t_x} = \sigma_{xx} E^t_{1x} \, e^{j\phi^t_x} \; + \; \sigma_{xy} E^t_{1y} \, e^{j\phi^t_y}$$

$$E^t_{1x}\ e^{j\phi^t_x}\left[\ 1\ +\ n\ -\ \frac{\omega}{k}\sigma_{xx}\ -\ \frac{\omega}{k}\sigma_{xy}\frac{E^t_{1y}}{E^t_{1x}}\ e^{j(\phi^t_y\ -\ \phi^t_x)}\ \right]=2E^i_{1x} \tag{A.13}$$

Using the following substitutions;

$$\frac{\omega}{k}=\frac{H_x}{E_y}=Z_0\quad ;\quad \frac{E^t_{1y}}{E^t_{1x}}\ e^{j(\phi^t_y\ -\ \phi^t_x)}=K$$

Equation 3.13 becomes;

$$\frac{E^t_{1x}}{E^i_{1x}}\ e^{j\phi^t_x}=\frac{2}{1\ +\ n\ -\ Z_0\ \sigma_{xx}\ -\ Z_0\ \sigma_{xy}} \tag{A.14}$$

A similar equation can be derived for the y-component of $\underline{E}$, by considering the loop in the x-z plane in Figure 3.12;

Integrating $\underline{H}$ around the loop as shown;

$$H^i_{1x}(t)L\ -\ H^r_{1x}(t)L\ -\ H^t_{1x}(t)L=-J_y(t)Ld$$

Letting d $\rightarrow$ 0;

$$H^i_{1x}(t)\ -\ H^r_{1x}(t)\ -\ H^t_{1x}(t)=-J_y(t)$$

Transforming to the frequency domain, and using 3.7;

$$H^i_{1x}\ -\ H^r_{1x}\ e^{j\phi^r_x}\ -\ H^t_{1x}\ e^{j\phi^t_x}=\sigma_{yx}\left[\ E^i_{1x}\ +\ E^r_{1x}\ e^{j\phi^r_x}\ \right]\ +\ \sigma_{yy}\left[\ E^i_{1y}\ +\ E^r_{1y}\ e^{j\phi^r_y}\ \right]$$

Using equation 3.12;

$$\frac{k}{\omega}E^i_{1y}-\frac{k}{\omega}E^r_{1y}\ e^{j\phi^r_y}-\frac{nk}{\omega}E^t_{1y}\ e^{j\phi^t_y}=\sigma_{yx}\left[\ E^i_{1x}\ +\ E^r_{1x}\ e^{j\phi^r_x}\ \right]+\sigma_{yy}\left[\ E^i_{1y}\ +\ E^i_{1y}\ +\ E^r_{1y}\ e^{j\phi^r_y}\ \right]$$

Eliminating reflection terms through 3.8 and 3.9;

$$\frac{k}{\omega}E^i_{1y}\ -\ \frac{k}{\omega}\left[\ E^t_{1y}\ e^{j\phi^t_y}\ -\ E^i_{1y}\ \right]\ -\ \frac{nk}{\omega}E^t_{1y}\ e^{j\phi^t_{1y}}=\sigma_{yx}E^t_{1x}\ e^{j\phi^t_x}\ +\ \sigma_{yy}E^t_{1y}\ e^{j\phi^t_y}$$

$$E^t_{1y}\ e^{j\phi^t_y}\left[\ 1\ +\ n\ +\ \frac{\omega}{k}\sigma_{yy}\ +\ \frac{\omega}{k}\sigma_{yx}\frac{E^t_{1x}}{E^t_{1y}}\ e^{-j(\phi^t_x\ -\ \phi^t_y)}\ \right]=2E^i_{1y}$$

$$\frac{E^t_{1y}}{E^i_{1y}}\ e^{j\phi^t_y}=\frac{2}{1\ +\ n\ +\ Z_0\ \sigma_{yy}\ +\ Z_0\ \sigma_{yx}K^{-1}}=\frac{2}{1\ +\ n\ +\ Z_0\ \sigma_{xx}\ -\ Z_0\ \sigma_{xy}K^{-1}} \tag{A.15}$$

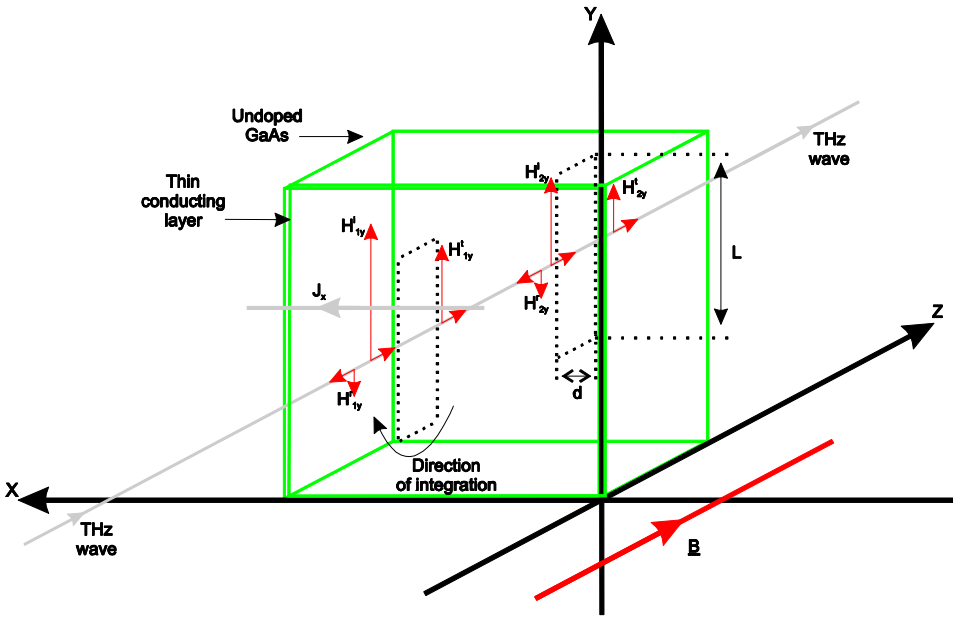

FIGURE A.3: Evaluation of x-component of current density in 2DEG using Maxwell equation around the loop in y-z direction.

A.0.2 Boundary Conditions at the Back Face:

The conditions for the THz electric field at the back face are identical in form to equations 3.8 and 3.9 (Figure 3.9);

$$E^i_{2x} \; + \; E^r_{2x} \; e^{j\delta^r_x} \; - \; E^t_{2x} \; e^{j\delta^t_x} = 0 \tag{A.16}$$

$$E^i_{2y} \; + \; E^r_{2y} \; e^{j\delta^r_y} \; - \; E^t_{2y} \; e^{j\delta^t_y} = 0 \tag{A.17}$$

where δ represents the relative phase shift for each field component.

As there is no surface current at the back face, the analysis for $\underline{H}$ does not involve terms in σ_{xx}, σ_{xy}, but is otherwise similar to the analysis for the front face. Therefore, equation 3.13 may be re-written for the back face as;

$$E^t_{2x} \; e^{j\delta^t_x}(1 \; + \; n) = 2nE^i_{2x}$$

$$\frac{E^t_{2x}}{E^i_{2x}} \; e^{j\delta^t_x} = \frac{2n}{1 \; + \; n} \tag{A.18}$$

Similarly for the y-component;

$$\frac{E^t_{2y}}{E^i_{2y}} \; e^{j\delta^t_y} = \frac{2n}{1 \; + \; n} \tag{A.19}$$

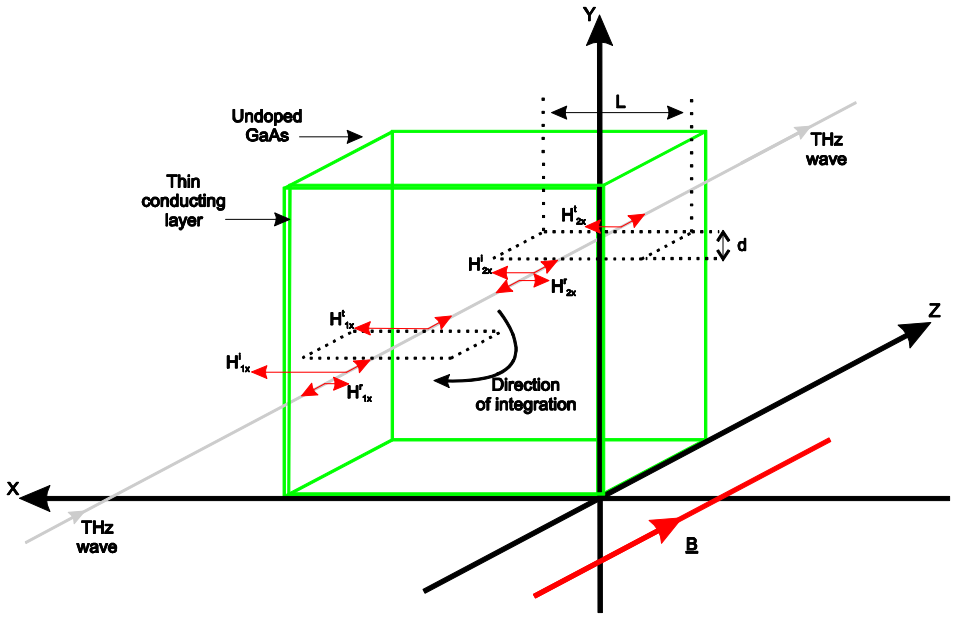

FIGURE A.4: Evaluation of y-component of current density in 2DEG using Maxwell equation around the loop in x-z direction.

A.0.3 Transmission Coefficients:

Equations 3.14, 3.15, 3.18 and 3.19 may be used to define a complex transmission coefficient for the whole sample, for both x and y components of the THz electric field. This quantity (including the phase) is measurable, and allows $\sigma_{xx}^{'}$, $\sigma_{xx}^{''}$, $\sigma_{xy}^{'}$ and $\sigma_{xy}^{''}$ to be calculated, owing to the relations derived in equations 3.14 and 3.15.

It is desired to find;

$$T_x = \frac{E_{2x}^t}{E_{1x}^i}\ e^{j(\delta_x^t\ +\ \phi_x^t\ +\ \beta)}$$

and

$$T_y = \frac{E_{2y}^t}{E_{1y}^i}\ e^{j(\delta_y^t\ +\ \phi_y^t\ +\ \beta)}$$

where β is the additional phase shift on passing through the sample.

Since

$$\frac{E_{2x}^t}{E_{1x}^i} = \frac{E_{2x}^t}{E_{2x}^i} \cdot \frac{E_{1x}^t}{E_{1x}^i} \cdot \frac{E_{2x}^i}{E_{1x}^t}$$

then

$$T_x = \frac{E_{2x}^t}{E_{2x}^i}\ e^{j\delta_x^t} \cdot \frac{E_{1x}^t}{E_{1x}^i}\ e^{j\phi_x^t} \cdot \frac{E_{2x}^i}{E_{1x}^t}\ e^{j\beta}$$

The unknown term $\frac{E^i_{2x}}{E^t_{1x}}$ may be evaluated by considering the Fourier integral formulation;

$$\underline{E}(z,t) = \int_{-\infty}^{\infty} \underline{E}_0 \; e^{jknz} \cdot e^{-j\omega t} \; d\omega$$

Writing n = N + jk,

$$\underline{E}(z,t) = \int_{-\infty}^{\infty} \underline{E}_0 \; e^{-kKz} \; e^{-j(\omega t \; - \; Nkz)} \; d\omega$$

$$\underline{E}(z,t) = \int_{-\infty}^{\infty} \underline{E}_w \; e^{-j(\omega t \; - \; Nkz)} \; d\omega$$

The ratio $\frac{E^i_{2x}}{E^t_{1x}}$ i.e. the ratio of $\underline{E_\omega}$ after and before passing through the sample, is then just $e^{-kK\Delta z}$, where Δz is the sample thickness.

Using equations 3.14, 3.15, 3.18 and 3.19;

$$T_x = \frac{2n}{(1 \; + \; n)} \cdot \frac{2}{(1 \; + \; n \; - \; Z_0 \; \sigma_{xx} \; - \; Z_0 \; \sigma_{xy} K)} \; e^{-kK\Delta z} \; e^{j\beta} \tag{A.20}$$

$$T_y = \frac{2n}{(1 \; + \; n)} \cdot \frac{2}{(1 \; + \; n \; + \; Z_0 \; \sigma_{xx} \; - \; Z_0 \; \sigma_{xy} K^{-1})} \; e^{-kK\Delta z} \; e^{j\beta} \tag{A.21}$$

The terms $e^{j\beta}$ can be eliminated by comparing T_x and T_y to transmission coefficients for a GaAs substrate without a conducting layer. Under these conditions, equation 3.14 can be re-written as;

$$\frac{\epsilon^t_{1x}}{E^i_{1x}} \; e^{j\varphi^t_x} = \frac{2}{1 \; + \; n} \tag{A.22}$$

And equation 3.15 can be re-written as;

$$\frac{\epsilon^t_{1y}}{E^i_{1y}} \; e^{j\varphi^t_y} = \frac{2}{1 \; + \; n} \tag{A.23}$$

where φ^t_x and φ^t_y are phase shifts in the x and y components on transmission through the front face of the sample, and ϵ^t_{1x} and ϵ^t_{1y} are corresponding amplitudes.

Using equations 3.22, 3.23, 3.18 and 3.19, new transmission coefficients can be defined for the sample without the conducting layer;

$$\Gamma_x = \frac{\epsilon^t_{2x}}{E^i_{1x}} \; e^{(j\delta^t_x \; + \; \varphi^t_x \; + \; \beta)} = \frac{4n}{(1 \; + \; n)^2} \; e^{-kK\Delta z} \; e^{j\beta} \tag{A.24}$$

$$\Gamma_y = \frac{\epsilon^t_{2y}}{E^i_{1y}}\ e^{(j\delta^t_y\ +\ \varphi^t_y\ +\ \beta)} = \frac{4n}{(1\ +\ n)^2}\ e^{-kK\Delta z}\ e^{j\beta} \tag{A.25}$$

Then using equation 3.20;

$$\frac{T_x}{\Gamma_x} = \frac{E^t_{2x}}{\epsilon^t_{2x}}\ e^{j[(\ \delta^t_x\ +\ \phi^t_x\ +\ \beta\ )\ -\ (\ \delta^t_x\ +\ \varphi^t_x\ +\ \beta\ )]} = \frac{1\ +\ n}{1\ +\ n\ -\ Z_0\ \sigma_{xx}\ -\ Z_0\ \sigma_{xy}K}$$

Defining total phase shifts with and without the conducting layer as;

$$\theta^c_x = \delta^t_x\ +\ \phi^t_x\ +\ \beta$$

$$\theta_x = \delta^t_x\ +\ \varphi^t_x\ +\ \beta$$

then

$$\frac{E^t_{2x}}{\epsilon^t_{2x}}\ e^{j(\theta^c_x\ -\ \theta_x)} = \frac{1\ +\ n}{1\ +\ n\ -\ Z_0\ \sigma_{xx}\ -\ Z_0\ \sigma_{xy}K}$$

$$\frac{E^t_{2x}}{\epsilon^t_{2x}}\ cos(\theta^c_x\ -\ \theta_x) = Re\left[\ \frac{1\ +\ n}{1\ +\ n\ -\ Z_0\ \sigma_{xx}\ -\ Z_0\ \sigma_{xy}K}\ \right] \tag{A.26}$$

$$\frac{E^t_{2x}}{\epsilon^t_{2x}}\ sin(\theta^c_x\ -\ \theta_x) = Im\left[\ \frac{1\ +\ n}{1\ +\ n\ -\ Z_0\ \sigma_{xx}\ -\ Z_0\ \sigma_{xy}K}\ \right] \tag{A.27}$$

Also, using equation 3.21;

$$\frac{T_y}{\Gamma_y} = \frac{E^t_{2y}}{\epsilon^t_{2y}}\ e^{j[(\ \delta^t_y\ +\ \phi^t_y\ +\ \beta\ )\ -\ (\ \delta^t_y\ +\ \varphi^t_y\ +\ \beta\ )]} = \frac{1\ +\ n}{1\ +\ n\ +\ Z_0\sigma_{xx}\ -\ Z_0\sigma_{xy}K^{-1}}$$

With

$$\theta^c_y = \delta^t_y\ +\ \phi^t_y\ +\ \beta$$

$$\theta_y = \delta^t_y\ +\ \varphi^t_y\ +\ \beta$$

$$\frac{E^t_{2y}}{\epsilon^t_{2y}}\ cos(\theta^c_y\ -\ \theta_y) = Re\left[\ \frac{1\ +\ n}{1\ +\ n\ +\ Z_0\ \sigma_{xx}\ -\ Z_0\ \sigma_{xy}K^{-1}}\ \right] \tag{A.28}$$

$$\frac{E^t_{2y}}{\epsilon^t_{2y}}\ sin(\theta^c_y\ -\ \theta_y) = Im\left[\ \frac{1\ +\ n}{1\ +\ n\ +\ Z_0\ \sigma_{xx}\ -\ Z_0\ \sigma_{xy}K^{-1}}\ \right] \tag{A.29}$$

Equations 3.26 $\rightarrow$ 3.29 provide the link between $\sigma^{'}_{xx}$, $\sigma^{''}_{xx}$, $\sigma^{'}_{xy}$, $\sigma^{''}_{xy}$ and the measured amplitude and phase of the THz signals.

The factor K may be deduced from the amplitude and phase measured after transmission through the sample with the conducting layer, as the ratio between x and

y components should be preserved during propagation through the undoped GaAs;

$$K = \frac{E_{1y}^t}{E_{1x}^t}\, e^{j(\phi_y^t\, -\, \phi_x^t)} = \frac{E_{2y}^t}{E_{2x}^t}\, e^{j(\theta_y^c\, -\, \theta_x^c)}$$

Appendix B

HEMT wafers used

Following HEMT wafers have been characterised using QHE. Same wafers were used to study electron dynamics at GHz/THz frequencies under strong magnetic fields and at cryogenic temperatures.

- L355
- L356
- L357
- L409
- L410
- L412
- L413
- L424
- L425
- L69
- L340
- L445
- L498

All the wafers were grown using the in house molecule beam epitaxy fabrication facility. Also all the grown wafers were processed for experimental measurements using the in in house clean-room facility.

Bibliography

[1] K. V. Klitzing et al. *PRL*, 45(6), 1980.

[2] A. B. Fowler et al. *Electronic properties of two dimensional systems, Chapter 2*, IBM Thomas J Watson Research Centre, New York 10598.

[3] C.H.W. Barnes. *Quantum Electronics in Semiconductors, Chapter 4*, Cavendish Laboratory, University of Cambridge.

[4] Daniel C. Tusi. *Reviews of Modern Physics*, 71(4), 1999.

[5] Klaus V. Klitzing. *Physica B*, 204(111-116), 1995.

[6] J Schurr et al. *Metrologia*, 44(15-23), 2007.

[7] M. Pepper et al. *J. Phys. C*, 16, L113, 1983.

[8] L. Engel et al. *PRL*, 71, 2638, 1993.

[9] F. Kuchar et al. *PRB*, 33, 2965, 1986.

[10] E. Abrahams et al. *PRL*, 42, 673, 1979.

[11] R. Joynt et al. *Journal of Physics*, C 18, L331, 1985.

[12] Y. Ikebe et al. *PRL*, 104, 256802, 2010.

[13] E. D. Palik et al. *Rep. Prog. Phys.*, 33, 1193, 1970.

[14] J. G. Mavroides et al. *Optical Properties of Solids, F. Abeles, ed.*, pp. 351-528, 1972.

[15] B. D. McCombe and R. J. Wagner. *Advances in Electronics and Electron Physics, L. Marton, ed.*, 37, pp 1-78, 1975.

[16] A. Petrou and B. D. McCombe. *Landau Level Spectroscopy, G. Landwehr and E. I. Rashba, eds.*, pp 679-775, 1991.

[17] R. J. Nicholas. *Handbook on Semiconductors, Volume 2 Optical Properties*, pp 385-461, 1994.

[18] J. Kono. *Methods in Materials Research*, Wiley, 2001.

[19] M. Seck et al. *Physica B*, 211 470-473, 1995.

[20] S. A. Crooker. *Revw. Sci. Instrum.*, 73, 3258, 2002.

[21] W. J. Walecki et al. *APL*, 63(13), 1993.

[22] N. A. Kabir et al. *APL*, 89, 2006.

[23] Alan B. Fowler et al. *IBM Thomas J Watson Research Center*, New York, 10598.

[24] D. Some and A. V. Nurmikko. *APL*, 65(26), 1994.

[25] Xianfeng Wang et al. *Optics Letters*, 32(13), 2007.

[26] Y. Ikebe et al. *PRL*, 104, 256802, 2010.

[27] X. Wang et al. *Opt. Exp.*, 18(12), 2010.

[28] J. Richter et al. *PRB*, 39(9), 1989.

[29] C. T. Liu et al. *PRB*, 40(3), 1989.

[30] D. M. Mittleman et al. *APL*, 71(1), 1997.

[31] Y. Ikebe et al. *PRL*, 104, 256802, 2010.

[32] J. N. Heyman et al. *APL*, 88, 162104, 2006.

[33] E. Castro-Camus et al. *APL*, 86, 254102, 2005.

[34] E. Castro-Camus et al. *Optics Express*, 15, 11, 2007.

[35] Nick C. J. van der Valk. *Optics Letters*, 30, 20, 2005.

[36] J. Faist et al. *Quantum Cascade Laser, Science (USA)*, 264, 1994.

[37] Kohler et al. *Nature*, pp. 156-159, 2002.

[38] M. Hajenius et al. *Optics Letters*, 33(4), 2008.

[39] Kazarinov et al. *Sov. Phys. Semiconductor*, pp. 707-709, 1971.

[40] G. Scalari et al. *APL*, 2006.

[41] B. S. Williams et al. *Optics Express*, 2005.

[42] S. Barbieri et al. *APL*, 13, 2004.

[43] Benjamin S. Williams. *Nature Photonics*, 1: 517-525, 2007.

[44] Giacomo Scalari et al. *APL*, 82(19), 2003.

[45] Michael Rochat et al. *APL*, 79(26), 2001.

[46] Jerome Faist et al. *APL*, 78(2), 2001.

[47] Toshiaki Suhara. *Semiconductor Laser Fundamentals*, Chapter 4, 1998.

[48] S. Kohen et al. *Applied Physics*, 2005.

[49] A. J. L. Adam et al. *APL*, 88, 2006.

[50] Martin van Exter et al. *J. Opt. Soc. Am. B*, 7(10), 1990.

[51] C. Dahl et al. *Spectroscopy of Solids*, 7-50, 1998.

[52] Charles A. Schmutteenmaer. *Chem. Rev.*, 104 (1759-1779), 2004.

[53] W. Fan et al. *Applied Spectroscopy*, 61(6), 2007.

[54] D. H. Auston et al. *APL*, 45(3), 1984.

[55] Masahiko Tani et al. *Japanese Journal of Applied Physics*, 36(9), 1997.

[56] J. T. Darrow et al. *Optics Letters*, 15(6), 1990.

[57] T-A. Liu et al. *APL*, 83, 1322, 2003.

[58] T-A. Liu et al. *Optics Express*, 12, 2954, 2004.

[59] Y. Cai et al et al. *APL*, 73(4), 1998.

[60] Shunsuke Kono et al. *APL*, 79(7), 2001.

[61] Y. C. Shen et al. *APL*, 85(2), 2004.

[62] Q. Wu and X. C. Zhang. *APL*, 67(24), 1995.

[63] Sang-Gyu Park et al. *APL*, 73(22), 1998.

[64] A. Bonvalet et al. *APL*, 67(20), 1995.

[65] R. A. Kaindl et al. *APL*, 75(8), 1999.

[66] O. Mitrofanov et al. *APL*, 77(4), 2000.

[67] D. B. MAst et al. *PRL*, 54, 1706-1709, 1985.

[68] D. C. Glattli et al. *PRL*, 54, 1710-1713, 1985.

[69] V. B. Sandomirskii et al. *Electrochimica Acta*, 34, 3-17, 1989.

[70] V. A. Volkov and S. A. Mikhailov. *Modern Problems in Condensed Matter Sciences*, 27.2, Chapter 15, pp. 855-907, 1991.

[71] V. A. Volkov et al. *JETP Letters*, 42, pp. 556-560, 1985.

[72] V. A. Volkov et al. *JETP Letters*, 44, pp. 655-659, 1986.

[73] V. A. Volkov et al. *Sov. Phys. JETP*, 67, 1639-1653, 1988.

[74] R. C. Ashoori et al. *PRB*, 45, 3894-3897, 1992.

[75] N. B. Zhitenev et al. *PRB*, 49, pp. 7809-7812, 1994.

[76] I. M. Grodnensky et al. *PRB*, 44, pp. 1946-1949, 1991.

[77] I. Grodnensky et al. *Helvetica Physica Acta*, 65, 359-360, 1992.

[78] T. Demel et al. *PRL*, 66, 2657-2660, 1991.

[79] S. J. Allen et al. *PRB*, 28, 4875-4877, 1983.

[80] C. Dahl et al. *Solid State Communication*, 80, 673-676, 1991.

[81] C. R. Proetto et al. *PRB*, 46, 16174-16177, 1992.

[82] X. Xia and J. J. Quinn. *PRB*, 50, 11187-11189, 1994.

[83] Y. P. Monarkha. *Fizika nizkikh temperature*, 21, 589-593, 1995.

[84] A. E. Kuchma and V. A.Sverdlov. *PRB*, 54, 16333-16336, 1996.

[85] S. A. Mikhailov. *Horizons in World Physics*, Volume 236, Chapter1.

[86] I. V. Kukushkin et al. *PRL*, 92, 23, 2004.

[87] Van der Pauw. *Philips Technical Review*, 20, pp. 220-224, 1958.

[88] M. B. Byrne. *PhD Thesis, School of Electronic and Electrical Engineering, University of Leeds*, December 2008.

[89] M. B. Byrne et al. *APL*, 98, 151104, 2011.

[90] Y.-M. Sun et al. *Chin. Phys. Lett.*, 24, 414, 2007.

[91] P. D. Ye et al. *APL*, 79, 14, 2001.

[92] A. A. Bykov et al. *APL*, 97, 82107, 2010.

[93] M. G. Vavilov et al. *PRB*, 70, 161306, 2004.

[94] M. U. Shaukat et al. *EP2DS-19/MSS-15*, Florida, USA, 2011.